The Significance of Surface Topography in the Synthesis and Application of (Super-)Liquid-Repellent Surfaces

Dissertation

zur Erlangung des Grades

„Doktor der Naturwissenschaften“

im Promotionsfach Chemie

am Fachbereich Chemie, Pharmazie und Geowissenschaften

der Johannes Gutenberg-Universität Mainz

Katharina Irene Hegner

geboren in Frankfurt am Main

Mainz, August 2022

Die vorliegende Arbeit wurde in der Zeit von August 2019 bis August 2022 am Max-Planck-Institut für Polymerforschung in Mainz unter Anleitung von [redacted] angefertigt.

Dekanin: Prof. Dr. Tanja Schirmeister

1. Berichterstatterin: [redacted]

2. Berichterstatter: [redacted]

Tag der mündlichen Prüfung: 02.11.2022

I hereby declare that I wrote the dissertation submitted without any unauthorized external assistance and used only sources acknowledged in the work. All textual passages which are appropriated verbatim or paraphrased from published and unpublished texts as well as all information obtained from oral sources are duly indicated and listed in accordance with bibliographical rules. In carrying out this research, I complied with the rules of standard scientific practice as formulated in the statutes of Johannes Gutenberg University Mainz to insure standard scientific practice.

_____

Mainz, August 2022

Table of Content

Abstract

In recent decades, the characteristic wetting properties of liquid-repellent and super-liquid-repellent surfaces have attracted a lot of attention in industry and academia. Both classes of functional materials are characterized by low lateral drop adhesion; drops roll off when the surfaces are tilted by just a few degrees. However, despite substantial research in this field, their successful implementation is challenged by difficulties in fabrication, chemical compatibility, and longevity. In this thesis, both fundamental and applied aspects are investigated to improve the basic understanding of these surfaces and bring forward their prospective applications.

While nowadays the design of superhydrophobic surfaces has been mastered to a commercial level, the large-scale fabrication of intricate overhang structures required to repel low surface tension liquids still poses significant challenges. Here, liquid flame spray is established as a simple one-step method for the fabrication of controlled particle-based surface structures. A variety of parameters can be tuned to simultaneously control the nanoscale, that is, the nanoparticle diameter and their aggregation into micrometer-sized features. In the *first part* of this thesis, these particle-based structures are optimized toward single bubble bursting and bulk defoaming. By optimizing the dual-scale surface topography, bubble rupturing can be tuned to a minimum rupturing time of only 2 ms. The porous surfaces are mechanically and chemically stable within the scope of the experiments. Finally, the concept of passive single bubble bursting is applied to greatly increase the collection efficiency in a froth flotation setup.

Super-liquid-repellent surfaces conventionally rely on the functionalization with fluoroalkyl substances to minimize the surface energy. This group of chemicals has been shown to be a potential environmental and health hazard, thereby limiting the applicability of fluorinated coatings. In the *second part* of this thesis, a novel fluorine-free, super-liquid-repellent surface is designed by combining particle-based structures and a liquid-like coating of covalently bonded polydimethylsiloxane chains. Without the use of fluorine, the underlying surface topography is even more crucial; so far, only silicon-based intricate doubly re-entrant structures prepared by a multi-step etching process have successfully repelled liquids with surface tensions lower than 48 mN m^{-1}. Here, drops of water-ethanol solutions with surface tensions as low as 31 mN m^{-1} can easily roll and bounce off, upon optimization of the underlying particle-based structures.

The *third part* explores the wettability of liquid-like polydimethylsiloxane surfaces with respect to solid-liquid interactions, estimated via the Hansen solubility parameter and a swelling ratio. On structured surfaces, wetting-induced swelling of the polymer chains by suitable solvents may result in the Wenzel

state, regardless of comparatively high surface tensions. On smooth surfaces, the associated change in interfacial energy fosters enhanced liquid-like behavior. Solvent-dependent interactions are an important factor to consider in the design and characterization of (super-)liquid-repellent surfaces.

Another approach to circumvent the need for fluorine is the use of slippery, lubricant-infused, porous surfaces. These surfaces are promising candidates for application in anti-icing due to delayed frost formation and low ice adhesion. However, depletion of lubricant from the solid scaffold by capillary forces exerted from growing frost dendrites typically limits their application. In the *fourth part* of this thesis, it is shown that lubricant depletion can be minimized by optimization of the underlying surface topography: tuning the interstitial spacing of the particle-based scaffold allows balancing or even exceeding the capillary forces exerted by the frost dendrites. This general design concept toward optimization of the underlying solid structure is termed capillary balancing.

In the *fifth part*, the effect of surface structure on the adhesion of bacteria is explored. Rather than the surface wettability, here the exact spacing and morphology of the structures are crucial. Single-configuration silicone nanofilaments have been found to effectively reduce bacterial adhesion in the superhydrophobic as well as the wetted state. The fibrous structures on the length scale just below the size of individual bacteria offer a greatly reduced number of anchoring sites. Here, the concept of using surface topography to passively reduce bacterial adhesion is explored using particle-based coatings prepared by liquid flame spray.

Zusammenfassung

In den letzten Jahrzehnten haben die charakteristischen Benetzungseigenschaften von (super-)flüssigkeitsabweisenden Oberflächen viel Aufmerksamkeit in Industrie und Wissenschaft erregt. Die Oberflächen zeichnen sich durch eine geringe laterale Adhäsion aus; Tropfen rollen ab, wenn die Oberflächen um nur wenige Grad geneigt werden. Trotz umfangreicher Forschung auf diesem Gebiet ist ihr kommerzieller Einsatz bisher durch Schwierigkeiten in der Herstellung, die chemische Kompatibilität und die mechanische Stabilität begrenzt. In der vorliegenden Dissertation werden sowohl fundamentale als auch angewandte Aspekte untersucht, um das grundlegende Verständnis dieser Oberflächen zu verbessern und ihre möglichen Anwendungen voranzubringen.

Die großtechnische Herstellung von Überhangstrukturen, wie sie für die Abweisung von Flüssigkeiten mit niedrigen Oberflächenspannungen benötigt werden, stellt eine große Herausforderung dar. Hierzu wurde im Rahmen dieser Arbeit eine einstufige Methode zur Synthese partikelbasierter Oberflächen mit kontrollierbaren Strukturen entwickelt: Bei der Flammensprühpyrolyse können eine Vielzahl von Parametern variiert und so der Durchmesser der Nanopartikel und die Aggregation in Strukturen auf der Mikrometerskala unabhängig voneinander kontrolliert werden. Im *ersten Teil* dieser Dissertation werden diese partikelbasierten Strukturen im Hinblick auf das Zerplatzen einzelner Blasen und die Entschäumung optimiert. Durch die Optimierung der Oberflächentopografie auf der Nano- und Mikrometerskala kann das Zerplatzen einzelner Blasen auf eine minimale Zeit von nur 2 ms reduziert werden. Die porösens Oberflächen zeigen im Verlauf der Experimente exzellente mechanische und chemische Stabilität. Schließlich wird das Konzept des passiven Zerplatzens von Blasen angewandt, um die Abscheideleistung einer Schaumflotationsanlage erheblich zu steigern.

Die außerordentlichen Benetzungseigenschaften von superflüssigkeitsabweisenden Oberflächen beruhen in der Regel auf einer Minimierung der Oberflächenenergie durch die Funktionalisierung mit Fluoralkylsubstanzen. Diese Gruppe von Chemikalien hat sich als potenzielles Umwelt- und Gesundheitsrisiko erwiesen, was die Anwendbarkeit von fluorierten Oberflächenmodifikationen einschränkt. Im *zweiten Teil* wird eine fluorfreie, superflüssigkeitsabweisende Oberfläche durch die Kombination von partikelbasierten Strukturen und einer Beschichtung aus kovalent gebundenem, linearem Polydimethylsiloxan entwickelt. Da auf Fluor verzichtet wird, spielt die Oberflächentopografie eine noch entscheidendere Rolle. Bisher war nur eine Oberflächenmodifikation mit doppelt einspringenden Überhangstrukturen, hergestellt durch ein mehrstufiges Ätzverfahren, in der Lage, Flüssigkeiten mit einer Oberflächenspannung von weniger als 48 $mN\,m^{-1}$ abzustoßen. Durch die

Optimierung der Strukturen, hergestellt mittels Flammensprühpyrolyse, können hier Tropfen einer Wasser-Ethanol-Lösung mit einer Oberflächenspannung von nur 31 mN m^{-1} problemlos abrollen und abprallen.

Der *dritte Teil* beschäftigt sich ausführlicher mit der Benetzbarkeit von Polydimethylsiloxan-funktionalisierten Oberflächen. Das flüssigkeitsähnliche Verhalten, hervorgerufen durch die hohe Mobilität der kovalent gebundenen Ketten, ist je nach Wechselwirkung mit der jeweiligen Probenflüssigkeit unterschiedlich stark ausgeprägt. Die Wechselwirkungen können mit Hilfe des Hansen-Löslichkeitsparameters und eines Quellverhältnisses abgeschätzt werden. Die Auswirkungen unterscheiden sich fundamental, je nach Oberflächentopografie. Auf strukturierten Oberflächen kann ein durch starke Wechselwirkungen hervorgerufenes Quellen der Polydimethylsiloxan-Ketten den Cassie-Wenzel-Übergang herbeiführen, unabhängig von vergleichsweise hohen Oberflächenspannungen. Auf glatten Oberflächen hingegen führt die durch das Quellen erhöhte Mobilität der Polydimethylsiloxan-Ketten zu verstärkten flüssigkeitsähnlichen Oberflächeneigenschaften. Lösungsmittelabhängige Wechselwirkungen sind demnach ein entscheidender Faktor, der bei der Entwicklung und Charakterisierung von (super-)flüssigkeitsabweisenden Oberflächen zu berücksichtigen ist.

Eine weitere Strategie, um den Einsatz von Fluor zu vermeiden, ist die Anwendung von porösen Oberflächenstrukturen, die mit einem Schmiermittel, zum Beispiel Silikonöl, imprägniert werden. Diese Oberflächenmodifikationen sind vielversprechende Kandidaten für den Schutz von Flugzeugen oder Windkraftanlagen vor Vereisung, da sie die Nukleation von Frost hinauszögern und die Adhäsion von Eis sehr gering ist. Ihr kommerzieller, langfristiger Einsatz wird jedoch häufig durch den Verlust des Schmiermittels und somit der flüssigkeitsabweisenden Eigenschaften verhindert. Wachsende Frostkristalle üben starke Kapillarkräfte auf das Schmiermittel aus, wodurch es aus der Oberflächenstruktur in die Kristalle gezogen wird. Im *vierten Teil* werden die Kapillarkräfte ausbalanciert und somit der Schwund des Schmiermittels verhindert, indem die Zwischenräume der partikelbasierten Oberflächenstrukturen optimiert werden.

Im *fünften Teil* wird der Einfluss der Oberflächenstruktur auf die Adhäsion von Bakterien untersucht. Es wurde bereits gezeigt, dass beispielsweise Silikon-Nanofilamente die Adhäsion von Bakterien sowohl im superhydrophoben als auch im benetzten Zustand wirksam reduzieren. Die faserigen Strukturen auf einer Längenskala knapp unterhalb der Größe einzelner Bakterien bieten eine stark reduzierte Anzahl von Anhaftungsstellen. Hier wird das Konzept zur passiven Verringerung von bakterieller Adhäsion auf partikelbasierten Oberflächen, hergestellt mittels Flammensprühpyrolyse, untersucht.

1 Introduction

1.1 Motivation and Outline

In recent years, liquid-repellent and super-liquid-repellent surfaces have attracted a lot of attention in academic and industrial research. Drops of water and/or low surface tension liquids easily roll off when surfaces are tilted by just a few degrees. This unique interaction with liquids warrants their potential application in the fields of self-cleaning or antifouling coatings, drag reduction, or the reduction of ice nucleation and adhesion. However, these surfaces rely on specific surface topographies that can be notoriously difficult to fabricate, challenging their successful application in real life. In the following thesis, these issues are addressed by combining fundamental and applied aspects.

The wettability of super-liquid-repellent surfaces is based on two principles: low surface energy, typically achieved by functionalization with a fluorinated hydrocarbon, and surface topography to reduce the solid-liquid interface. A major challenge to the widespread use of super-liquid-repellent coatings is the lack of structural control in conventional large-scale coating methods, such as spray or dip coating. However, the topography on the nano- and micrometer scale and geometrically re-entrant structures are essential to achieve superior performance against low surface tension liquids. Here, liquid flame spray (LFS), also known as flame spray pyrolysis, is proving a valuable technique enabling the production of coatings where nano- and micrometer scale topography can be tuned simultaneously (Chapters 2, 3, 4, and 6). A range of process parameters can be adjusted to provide characteristic microscale features composed of nanoparticles with variable particle diameters. In Chapter 2, this method enables the optimization of fluoroalkyl-functionalized coatings toward ultrafast single bubble bursting and bulk defoaming (Figure 1.1a). Variation of only two process parameters allows the production of a large range of surface topographies. The results show that super-liquid-repellency alone does not guarantee superior functionality: here, the dual-scale surface topography is crucial for the application in bubble bursting.
In Chapter 3, super-liquid-repellency without the use of fluoroalkyl substances is explored. Due to this class of chemicals' potentially harmful effects on the environment and human health, alternatives are urgently needed. Instead, the structures are functionalized with a thin coating of covalently bonded, liquid-like polydimethylsiloxane (PDMS) as an environmentally friendly, non-toxic, and biocompatible alternative (Figure 1.1b). As the surface cannot rely on a fluoroalkyl-functionalization, the underlying surface structure and re-entrant geometries are even more crucial to achieve super-liquid-repellency toward low surface tension liquids. Different coating methods are explored to produce a range of

nanoparticle-based surfaces: single-configuration candle soot and spray coating, and tunable liquid flame spray.

The wettability of covalently bonded PDMS is investigated in more detail in Chapter 4. Due to the low glass transition temperature, the polymer chains are a melt at room temperature and exhibit high chain mobility. When in contact with suitable probe liquids, swelling of the chains results in enhanced liquid-like properties. While the effect has been previously observed on smooth surfaces, the effect of wetting-induced adaptation on the wettability of structured surfaces has yet to be explored.

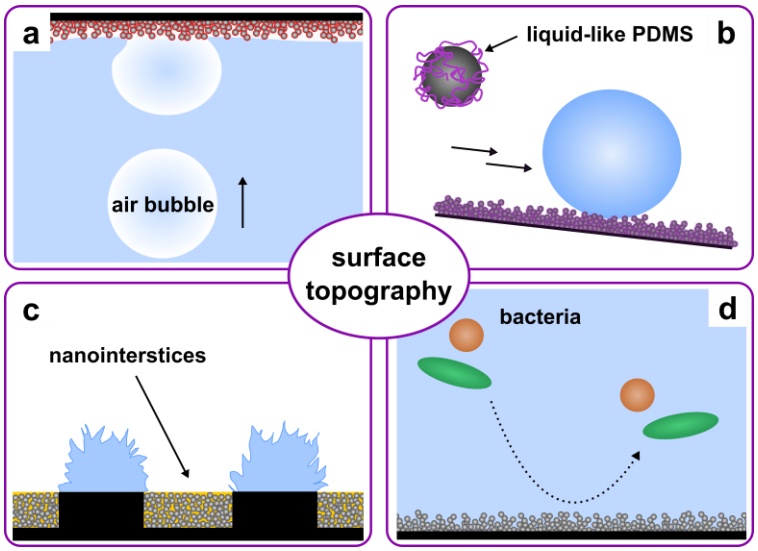

Figure 1.1. Surface topography is a crucial factor for various applications and the exploration of fundamental questions. a) A dual-scale topography allows the ultrafast rupturing of contacting air bubbles. b) Optimized particle structures allow the repellency of low surface tension liquids without the need for a fluoro-functionalization. c) For SLIPS, tuning of the interstitial spacing allows lubricant retention under harsh conditions. d) Even in the wetted state, a sub-micrometer roughness may inhibit the adhesion of bacteria because of reduced anchoring area.

Slippery, lubricant-infused, porous surfaces (SLIPS) rely on a different mechanism: here, the air between the surface structures is replaced by a second immiscible liquid which forms a defect-free, chemically homogeneous surface. The application of SLIPS in anti-icing and other fields is limited due to the depletion of the lubricant from the solid scaffold. In Chapter 5, frost-induced depletion of lubricant is controlled via optimization of the underlying solid structure (Figure 1.1c). By tuning the interstitial spacing, the capillary forces exerted by growing frost dendrites are balanced, thereby stabilizing the lubricant in the scaffold.

In Chapter 6, the effect of surface topography on the adhesion of bacteria is explored. It has been shown that fibrous silicone nanofilaments on a length scale just below the size of bacteria offer a greatly reduced

anchoring area and thereby reduce bacterial adhesion even in the wetted state. Here, the validity of this design principle is examined on particle-based coatings prepared by liquid flame spray (Figure 1.1d).

This thesis gives a brief introduction on how to describe and characterize the wetting properties of a surface (Chapters 1.2 and 1.3). Furthermore, an overview of relevant natural and artificial surfaces and of recent advances in the fabrication of surfaces with liquid-repellent and super-liquid-repellent wetting properties is given (Chapter 1.4). Thereafter, a number of potential real-life applications are discussed, specifically anti-biofouling and anti-icing (Chapter 1.5). Chapters 2 to 5 consist of original contributions to fundamental questions and the fabrication and application of super-liquid-repellent and liquid-repellent surfaces. Each chapter contains an Introduction, Results and Discussion, a Conclusion, Methods, and relevant Supporting Information. For publications (Chapters 2 and 5), the Supporting Information in its entirety is available online with the publisher. At the end of each chapter, the authors' contributions are summarized. Finally, Chapter 7 summarizes the findings and gives a brief outlook.

1.2 How to Describe Wetting

Predicting and controlling the wettability of surfaces[1–4] is essential for many areas of basic science as well as industry and our daily life. Wetting and de-wetting need to be controlled for applications in printing, painting, microfluidics, or in the distribution of pesticides and herbicides. The wettability determines the adhesion of drops[5,6] to lenses and mirrors and the aggregation of ice[7–9] on airplanes and wind turbines.

To quantitatively describe surface wettability, one usually considers a single drop placed on the surface. Independent of the volume, the wettability of the solid depends on the balance of interfacial tensions, that is the solid-air γ_{SA}, the solid-liquid γ_{SL}, and the liquid-air γ_{LA} interfacial surface tension. The interfacial tension γ can be interpreted as the work required to increase the interface dA between two adjacent phases as a measure of work per area or force per length (mN m^{-1}):

$$\gamma = \frac{\mathrm{d}W}{\mathrm{d}A}. \tag{1}$$

Within the bulk of a phase, cohesive interactions such as van-der-Waals forces, hydrogen bonding, or electrostatic interactions lead to a strong attraction. At the phase boundary, molecules are partially surrounded by molecules from the other phase and thus, have fewer attractive bonding partners. Therefore, the smallest possible interface is formed. In order to increase the interfacial area, molecules

from the bulk need to the transported to the interface and intermolecular bonds need to be broken. Hence, increasing the interfacial area requires work, the interfacial tension.[10]

A liquid tends to spread onto a solid provided that the solid-air interfacial tension is larger than the sum of solid-liquid and liquid-air interfacial tensions, $\gamma_{SA} > \gamma_{SL} + \gamma_{LA}$.[10,11] Thus, the sign of the so-called spreading parameter S determines the behavior of a drop placed on a solid:

$$S = \gamma_{SA} - \gamma_{SL} - \gamma_{LA} . \tag{2}$$

For S > 0, the drop spreads completely, whereas for S < 0, partial wetting occurs.

1.2.1 Ideal Wetting

The shape of a drop placed on an ideal, smooth surface is dictated by the balance of the interfacial forces acting at the three-phase contact line (Figure 1.2a). In thermodynamic equilibrium, the relation between interfacial tensions and the contact angle is described by what is commonly known as the Young's equation:

$$\cos\theta = \frac{\gamma_{SA} - \gamma_{SL}}{\gamma_{LA}}, \tag{3}$$

where θ is the contact angle at the three-phase contact line.[11] This equation applies to flat and chemically homogeneous surfaces where the contact angle is univocally limited by the chemical nature of the different phases. If a drop of water forms an angle smaller than 90°, the surface is defined as hydrophilic (Figure 1.2b). Surfaces are hydrophobic if contact angles larger than 90° are observed (Figure 1.2c).

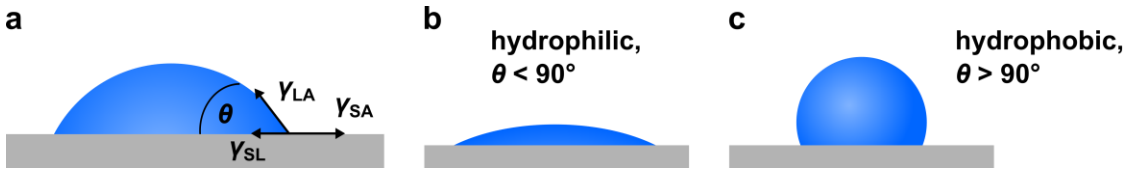

Figure 1.2. Partial wetting of a water drop on a flat surface. a) The contact angle θ at the three-phase contact line is determined by the balance of interfacial tensions. A water drop is deposited on b) a hydrophilic and c) a hydrophobic surface.

For low surface tension oils, surfaces are defined as oleophilic and oleophobic, analogously. If the behavior applies to water, oils, and organic liquids, surfaces are called amphiphilic and amphiphobic.[12] While complete wetting has been observed using low surface tension oils, angles higher than approximately 120° have not been achieved on smooth surfaces.

1.2.2 Wetting on Rough Surfaces

Most real surfaces feature some level of roughness which can cause significant deviations from the ideal Young's contact angle. On rough surfaces, drops either conform to the topographic features and form a continuous solid-liquid interface (Figure 1.3a) or they rest on a composite solid-air interface (Figure 1.3b). The two states are called the Wenzel and the Cassie-Baxter state, respectively.

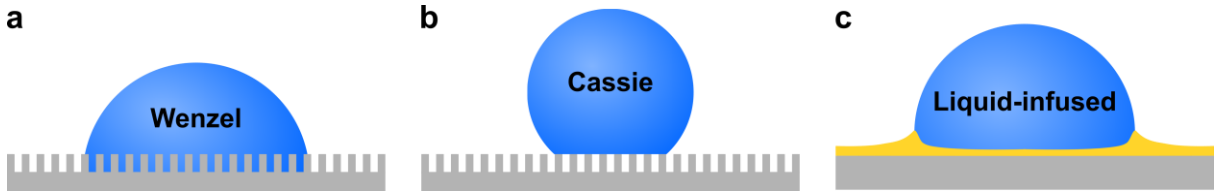

Figure 1.3. a) In the Wenzel state, drops conform to the surface topography and form a continuous solid-liquid interface. b) In the Cassie state, drops partially rest on air cushions trapped between the solid surface structures. c) Drop resting on a lubricant-infused surface.

In the Wenzel state[13], contact line progression of a spreading drop results in the replacement of the solid-air by a solid-liquid interface and an increase of the liquid-air interfacial area. The change in surface energy dE from the contact line displacement dx can thus be described as

$$\mathrm{d}E = r\,(\,\gamma_{SL} - \gamma_{SA}\,)\,\mathrm{d}x + \gamma_{LA}\,\mathrm{d}x\cos\theta^{*}\,, \tag{4}$$

where the geometric factor r represents the ratio of the actual over the apparent surface area. At equilibrium (dE = 0), this yields the Wenzel equation which relates the apparent contact angle on a rough surface θ^* to the contact angle on an ideal surface of the same chemical nature:

$$\cos\theta^{*} = r\,\cos\theta\,. \tag{5}$$

According to the Wenzel model, roughness amplifies the wetting properties of a surface in both directions, but it cannot invert the wettability. On hydrophobic surfaces, a roughness factor larger than 1 results in enhanced hydrophobicity ($\theta^* > \theta$). Vice versa, a hydrophilic surface becomes more hydrophilic ($\theta^* < \theta$). Some limitations to the model should be kept in mind: arbitrarily large values for the geometric factor r imply the possibility of complete wetting or drying. However, high contact angles larger than 150° are not observed in the Wenzel state. Furthermore, Kao researchers showed that below a critical contact angle θ_c, the apparent contact angle θ^* hardly depends on the value of θ.[14,15] If

hemiwicking, i.e. the formation of a pre-wetting layer, occurs, the surface wettability no longer follows the assumptions of the Wenzel regime.[4]

Roughness cannot only amplify the wetting properties but also introduce new features, such as super-liquid-repellency. On superhydrophobic surfaces, drops of water do not form a continuous wetting interface with the solid. Rather, they rest on a composite interface of solid protrusions and air cushions stabilized between the surface structures (Figure 1.3b). Displacement of the contact line by dx results in the creation of new solid-liquid and liquid-air interfaces:

$$dE = \phi_{SL} (\gamma_{SL} - \gamma_{SA}) dx + (1 - \phi_{SL}) \gamma_{LA} dx + \gamma_{LA} dx \cos \theta^* , \quad (6)$$

where ϕ_{SL} is the solid area fraction of the surface in contact with the drop. Here, a flat liquid-air interface is assumed. At equilibrium, this yields the Cassie-Baxter equation[16] for the apparent contact angle cos θ*:

$$\cos \theta^* = \phi_{SL} [\cos \theta + 1] - 1. \quad (7)$$

Superhydrophobic surfaces are defined as exhibiting water contact angles greater than 150° and low contact angle hysteresis of less than 10°. Superamphiphobicity expands this concept to include repellency toward low surface tension oils and organic liquids.[17–19]

Apart from superhydro- or superamphiphobic surfaces, low contact angle hysteresis can also be achieved by the replacement of air with a second, immiscible liquid, resulting in a slippery, lubricant-infused surface (Figure 1.3c).[20–23]

1.2.3 Three-Phase Contact Line

Both, the Wenzel and the Cassie equation imply that the area of contact between the solid and the liquid away from the contact line affects the contact angle. However, numerous studies have shown that the contact angle is controlled only by the narrow region at the three-phase contact line.[1,24,25]

The importance of the contact line structure for the contact angle and the contact angle hysteresis has been extensively discussed by McCarthy et al. A simple experiment is employed to emphasize the role of the contact line over the solid-liquid interface.[25] Various two-component surfaces based on either different surface chemistry or topographies were prepared (Figure 1.4). Advancing and receding contact angles were measured for different island (d) and water drop (D) diameters. The fractions f_1 and f_2 correspond to the area fractions inside and outside the island, for example, a hydrophilic island on a

hydrophobic surface (Figure 1.4a). The contact angles were calculated using the Cassie equation for a binary surface

$$\cos\theta^* = f_1 \cos\theta_1 + f_2 \cos\theta_2 . \quad (8)$$

Comparison of the calculated versus the observed contact angles shows that values predicted by the Cassie equation are not reliable.[25] As soon as the contact line does not contact the hydrophilic island (D > d), the island no longer influences the contact angles formed. The contact angles equal those observed on a homogeneously hydrophobic surface. The same effect could be observed for the other two configurations (Figure 1.4b,c) and in a similar experiment conducted by Extrand[24]. The results of these experiments indicate that the advancing and receding contact angles are governed by events occurring at the three-phase contact line.

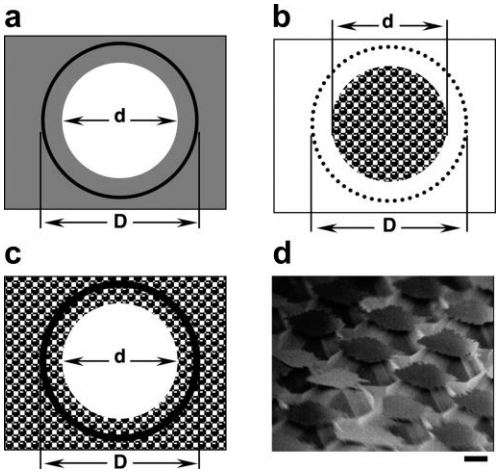

Figure 1.4. Schematic depiction of two-component surfaces employed by Gao et al. The samples consist of a) a hydrophilic island on a hydrophobic surface, b) a rough island on a smooth surface, and c) a smooth island on a rough surface. d) Scanning electron microscopy (SEM) image of the rough structures (scale bar is 10 µm). Reprinted with permission from ref.[25] Copyright 2007, American Chemical Society.

1.2.4 Contact Angle Hysteresis

On real surfaces, pinning of the contact line at topographic defects, chemical inhomogeneities, contaminations, or surface charges prevents drops from sliding freely. As a result, when a drop is moving on an inclined surface or when its volume is increased or decreased, it will exhibit a difference between the advancing (θ_{adv}) and receding (θ_{rec}) contact angle.[4,6,26] The difference between these two values is called the contact angle hysteresis, $\Delta\theta$:

$$\Delta\theta = \theta_{adv} - \theta_{rec}. \quad (9)$$

The contact line moves at a constant advancing and receding contact angle, characteristic of the surface chemistry and topography. A metastable static drop can form any contact angle between these two values. Therefore, these values are more valuable for the characterization of a surface than a static contact angle. It has long been observed that drops with a small contact angle hysteresis easily slide on a tilted surface. Vice versa, drops with a large contact angle hysteresis might not move at all when the surface is tilted.[27] Contact angle hysteresis is essential for our daily life by providing friction to drops and it can be measured using several methods (Chapter 1.3.1).[26]

Chemical heterogeneities and surface roughness have been identified as contributing to contact angle hysteresis early on (Figure 1.5a,b). At the border between patches of different surface chemistry or different solid surface energies, the contact line needs to overcome an energy barrier, resulting in sticking, stretching, and jumping events.[26,28] Therefore, the movement of the contact line on heterogeneous surfaces is typically slower than on homogeneous surfaces.[26] If the contact angle hysteresis differs in the individual regions, contact line movement on the heterogeneous composite surface becomes increasingly slower.[29]

If a drop advancing over a surface with rough features, conforms to the surface roughness, the microscopic slope of the contact angle θ_e can differ substantially from the apparent slope θ_r (Figure 1.5b). Pinning of the contact line at defects results in large contact angle hysteresis, characteristic of the Wenzel state.[4] Oftentimes, even macroscopically smooth surfaces exhibit microgrooves or patterns due to the fabrication method. The extent of contact angle hysteresis depends on the specific structure as well as the direction of motion.[26]

On flexible, soft surfaces, such as elastomers and hydrogels, the formation of a wetting ridge[30,31] can induce pinning and increase the contact angle hysteresis (Figure 1.5c). Furthermore, wetting-induced surface adaptation can lead to a difference in interfacial tension at the front and rear sides of a moving drop (Figure 1.5d). Surface adaptation may result from the reorientation of side groups and polymer segments, from diffusion and swelling, or the replacement of an adsorption layer.[32–35] These processes are time-dependent and associated with a change in solid-liquid interfacial energy. The effect of surface adaptation on wetting has only recently been modeled by Butt et al. who assume an exponential decrease in interfacial tension from the initial value γ_{SL}^{0} to the interfacial tension at equilibrium γ_{SL}^{∞}. The time scales depend on the system and can vary from nanoseconds (liquid ordering) to minutes or hours (polymer reorganization).[32] Furthermore, it has been shown that contact line movement can be affected by spontaneous charging of the surface.[36]

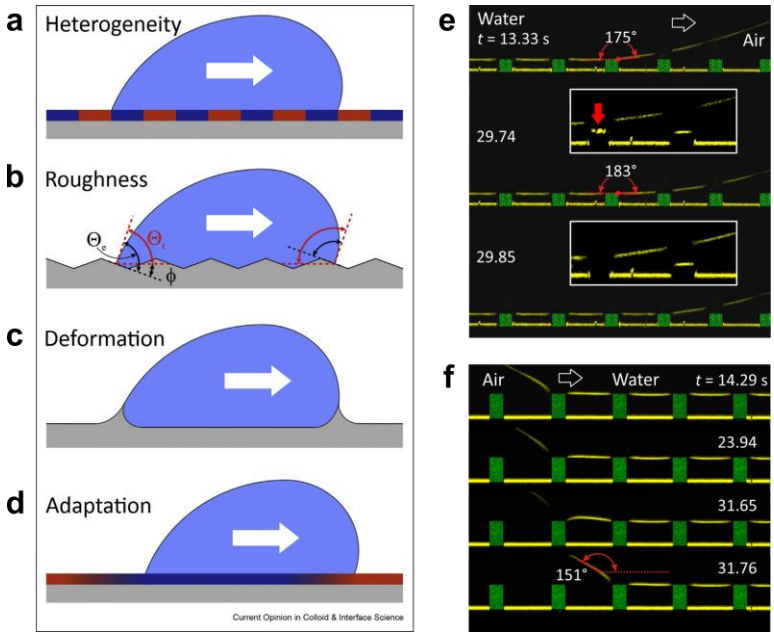

Figure 1.5. a-d) Effects leading to contact angle hysteresis include chemical heterogeneities, surface roughness, surface deformation, and surface adaptation. Reprinted with permission from ref.[26] Copyright 2018, American Chemical Society. e) Advancing and f) receding waterfront on a superhydrophobic micropillar array visualized using laser scanning confocal microscopy. Reprinted with permission from ref.[37] Copyright 2016, American Physical Society.

It should be noted that surface roughness and pinning of the contact line do not always result in reduced drop mobility. On super-liquid-repellent surfaces, drops quickly roll off when the surface is tilted by a few degrees even though the hysteresis is typically around 30°. Using laser scanning confocal microscopy (LSCM), water advancing on a hydrophobized micropillar array is imaged.[28,37] On the advancing side, the drop gradually bends down until it touches the top face of the next pillar, resulting in advancing contact angles of approximately 180° (Figure 1.5e). The receding side is pinned until a threshold force is overcome and the capillary bridge snaps back into the drop (Figure 1.5f). Nonetheless, drops roll off easily because of low lateral adhesion: the contact width w of the drop is low and the cosine at high contact angles does not change much anymore, rendering the precise value of θ_{adv} less critical (Chapter 1.3.3).[26] Here, pinning of the receding contact line can be greatly reduced by introducing a second length scale.[17]

Overall, contact angle hysteresis is caused by numerous phenomena at the micro-, nano-, and even atomic scale. On real surfaces, it is hardly avoidable. Characterization of the narrow region around the three-phase contact line poses a challenge, so far leaving the structure and dynamics largely unexplored.[26]

1.3 Wetting Characterization

1.3.1 Static Contact Angle

On a macroscopic scale, the apparent static contact angle is typically quantified via goniometry.[38] Here, *apparent* is defined as a length scale much larger than the surface roughness or chemical inhomogeneities.[26] For measurements of the apparent static contact angle a drop with a volume of typically less than 10 µL is carefully deposited on a surface. Directly after, a camera records the drop profile. The contours of the drop are detected, extrapolated to the three-phase contact line, and the contact angles are measured using the appropriate fitting method. The exact value of the apparent static contact angle can vary, depending on the measurement protocol. It takes a value between the advancing and the receding contact angle.

Several settings chosen by the user may influence the outcome of the measurements: 1) the choice of fitting method, 2) camera settings such as magnification, illumination intensity, and contrast, 3) dosing speed, volume, and distance, and 4) the time between drop deposition and measurement. Especially the choice of fitting method between the circular, the Young-Laplace, the tangent, and the ellipse fit can result in variations of up to 30°.[39] Both the circular and the Young-Laplace fit assume equal contact angles on both sides of the drop. Especially on rough surfaces, this is rarely the case due to pinning points at surface protrusions. Therefore, the tangent and the ellipse fit which allow different contact angles at the left and right sides of the three-phase contact line are more suitable.

Furthermore, a distinction between the Wenzel and the Cassie state is not always clear (Figure 1.6b). The macroscopic camera cannot discern between a drop that conforms to the topography of the underlying surface and a drop resting on a composite solid-air interface. The same challenge emerges on lubricant-infused surfaces: here, the three-phase contact line can be obscured by a wetting ridge formed by the lubricant. To answer this question, other techniques such as LSCM can be used (Figure 1.6c).[37]

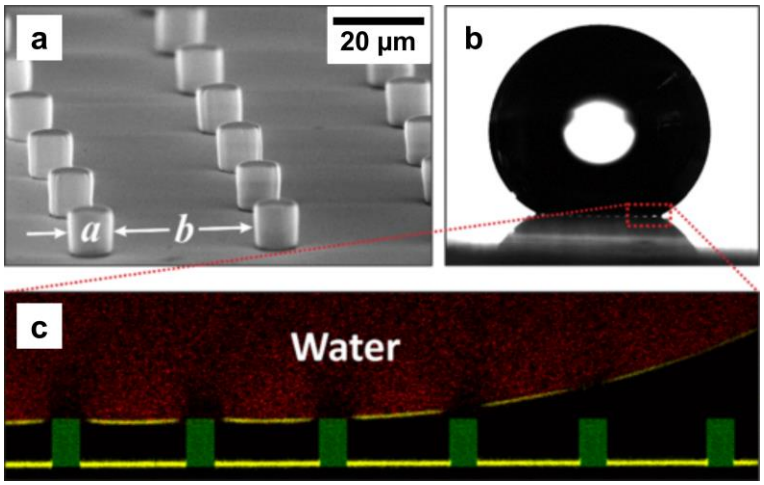

Figure 1.6. SEM image of a regular micropillar array prepared via photolithography. b) Image of a water drop resting on a hydrophobized micropillar array (drop height is 2 mm). The image is acquired using a contact angle goniometer. c) Image of the water drop acquired via LSCM. The fluorescent signal from the dyed water allows discrimination between the liquid and the air cushions between the pillars. Reprinted with permission from ref.[37] Copyright 2016, American Physical Society.

1.3.2 Dynamic Contact Angles

To properly characterize the wettability of a surface, measurement of the advancing and receding contact angles and/or the roll-off angles is required. The advancing and receding contact angles are characteristic quantities specific to a surface.[6,26,40] Generally, the values depend on the speed of the propagating contact line. Therefore, one can distinguish between the static or dynamic advancing and receding contact angles. The static advancing contact angle is recorded just before the contact line starts to advance. Vice versa, the dynamic advancing contact angle is the characteristic angle at which the contact line advances.[26] Typically, dynamic contact angles are used to characterize the wettability of a surface. There are several measurement techniques including the capillary rise[41,42] or Wilhelmy plate method[43,44]. Another common method involves adding and retrieving a controlled volume to a sessile drop at a low speed using a contact angle goniometer.[33] While inflating the drop, the contact line is initially pinned (Figure 1.7a). The contour of the drop changes causing the contact angle to increase. Once the advancing contact angle θ_{adv} is reached, the contact line moves while maintaining the dynamic advancing contact angle at the three-phase contact line (upper plateau in Figure 1.7c). Thereafter, the volume is retrieved again. The contact angle decreases until it reaches the receding contact angle θ_{rec} (Figure 1.7b and lower plateau in Figure 1.7c). Typically, a dosing speed of around 0.5 µL s^{-1} is used. It should be noted that if

the surface interacts with and adapts to the liquid, the contact time between surface and liquid can influence the results.

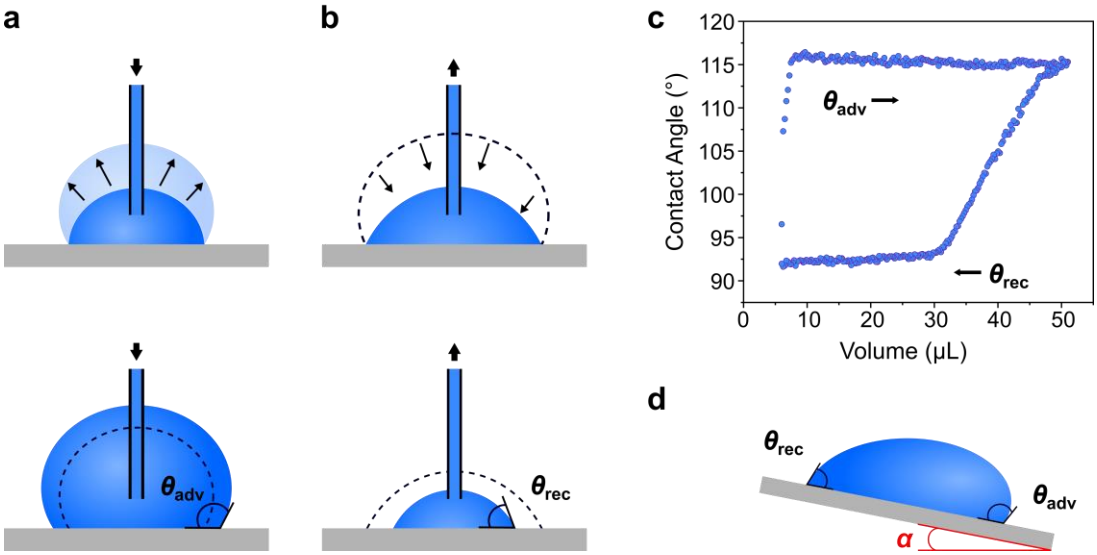

Figure 1.7. Measurement of the advancing θ_{adv} and the receding contact angle θ_{rec} by a,) inflating and b) deflating a sessile drop. c) Representative result of contact angle measurements showing the characteristic plateaus for θ_{adv} and θ_{rec} when the volume is increased and decreased, respectively. Measurement of the advancing θ_{adv} and the receding contact angle θ_{rec} via d) the tilted plate method.

Furthermore, the so-called tilted-plate method can be employed (Figure 1.7c).[34] Here, the substrate is gradually inclined, increasing the gravity acting on the drop until it begins to move. For the static advancing and receding contact angles, the image right before the onset of motion is analyzed. The technique also allows determining the dynamic contact angles during drop motion. However, it is not suitable for surfaces where i) the drop's adhesion to the surface is too high and drop motion cannot be induced by gravity or ii) super-liquid-repellent surfaces where drops quickly move out of the camera's field of view.

Instead, for super-liquid-repellent surfaces, the tilted plate setup may be used to measure the roll-off angle α. Again, a drop is deposited on the surface, and thereafter, the surface is slowly tilted. The drop rolls off at the angle α when the drop's lateral adhesion is overcome by the gravitational force F_g acting on the drop:

$$F_g = m\, g\, \sin\alpha\,, \tag{10}$$

where the roll-off angle is related to the drop volume via m, the drop mass.[45–47]

1.3.3 Lateral Adhesion Force Measurements

Lateral adhesion force measurements can offer complementary information on (super-)liquid-repellent surfaces: for the three main classes, namely superhydro- or superamphiphobic surfaces, liquid-like surfaces, and lubricant-infused surfaces, similar contact angle hysteresis might be observed. The characteristic force curves may differ substantially, though.[48]

The lateral adhesion force of drops sliding on a surface can be measured directly using a so-called drop adhesion force instrument (DAFI, Figure 1.8a).[5,6] Here, a drop is deposited on a surface and brought into contact with a flexible capillary. The surface is then moved at a constant velocity while the drop remains pinned to the capillary. The deflection of the capillary can be measured using a laser or a macroscopic optical camera. The drop adhesion force is determined from the deflection Δx of the capillary with a spring constant k_s:

$$F_{LA} = \Delta x \, k_s. \tag{11}$$

Depending on the setup, the drop shape and the advancing and receding contact angles may be measured simultaneously.

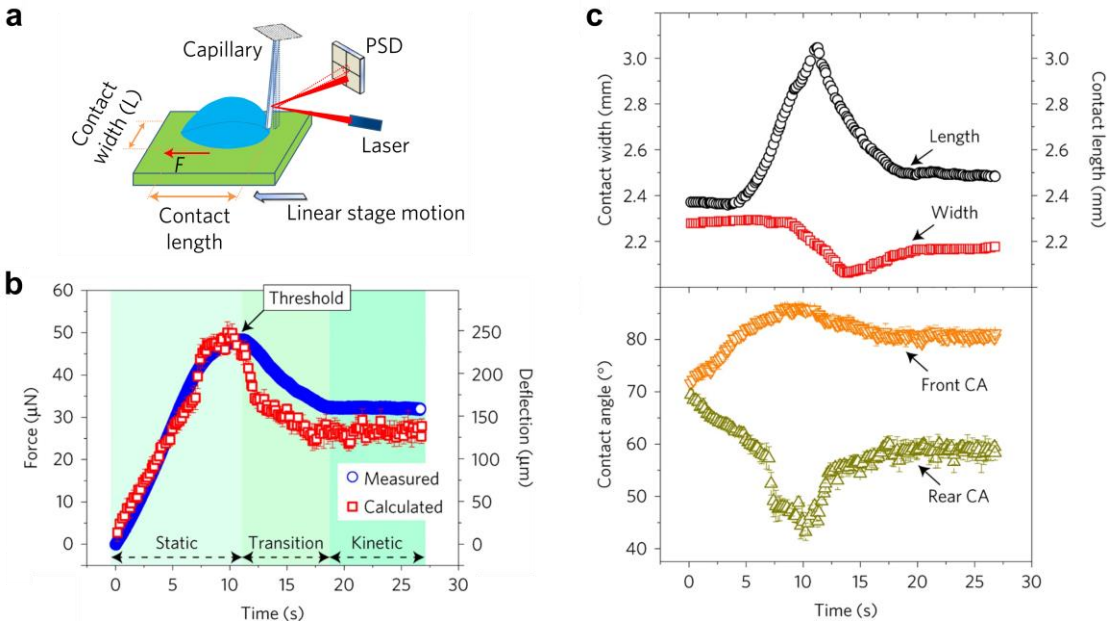

Figure 1.8. a) Schematic illustration of a drop adhesion force instrument (DAFI). b) Both the measured and the calculated lateral adhesion forces show three different regimes. c) Simultaneously recorded drop contact width and length and front and rear contact angles allow the calculation of the lateral adhesion forces. Reprinted with permission from ref.[6] Copyright 2016, American Physical Society.

Gao et al. observed an analogy to the friction between two solids: one can distinguish between the static, a transition, and the kinetic regime (Figure 1.8b).[6] For a drop to start sliding, a threshold force must be overcome. Thereafter, a constant, lower kinetic force is required to keep the drop in motion.

The different regimes are also apparent in the drop shape and the rear and front contact angles (Figure 1.8c). Within the first 5 s, the front and rear contact angles increased and decreased, respectively, while the contact line did not move. Afterward, the drop started to elongate. After approximately 10 s, the maximum difference between the front and rear contact angles was reached, and the threshold static adhesion force was overcome. In the transition regime, the shape of the drop circumference and the contact angles changed until finally, after 18 s, the kinetic regime was reached.

Theoretically, the lateral adhesion force F_{LA} can be described via the liquid's surface tension γ_{LA}, the advancing and receding contact angles, and the drop volume:

$$F_{LA} = w\,\gamma_{LA}\,k\,(\cos\theta_{rec} - \cos\theta_{adv}), \qquad (12)$$

where w is the contact width of the drop perpendicular to the direction of motion and the dimensionless factor k accounts for angular variations of the three-phase contact line.[46,47,49] Calculations of the lateral adhesion force according to Eq. 12 show good agreement with the experimental values and reflect the different regimes (Figure 1.8b).

Furthermore, a linear dependence of the friction forces with the contact width has been observed. Both the static and the kinetic adhesion forces increase with increasing velocities. Generally, the ratio between the two regimes and the adhesion forces depends on the type of substrate used.

1.4 Preparation of (Super-)Liquid-Repellent Surfaces

In recent decades, a great number of studies have discussed the fabrication of surfaces where drops exhibit low lateral adhesion. Generally, these surfaces can be classified as (1) superhydro(amphi)phobic, (2) slippery, lubricant-infused, porous, and (3) liquid-like surfaces (Figure 1.9).

Superhydro(amphi)phobicity can be introduced via low surface energy overhang structures that prevent wetting of the underlying substrate.[18] Alternatively, slippery liquid-repellent surfaces can be produced by replacing the air trapped in the porous surface structures with a compatible lubricant.[20,22] Furthermore, flexible polymer chains can be grafted to the substrate, resulting in a smooth, liquid-like coating.[50] The three different approaches are discussed in the next chapters on the basis of relevant surface modifications.

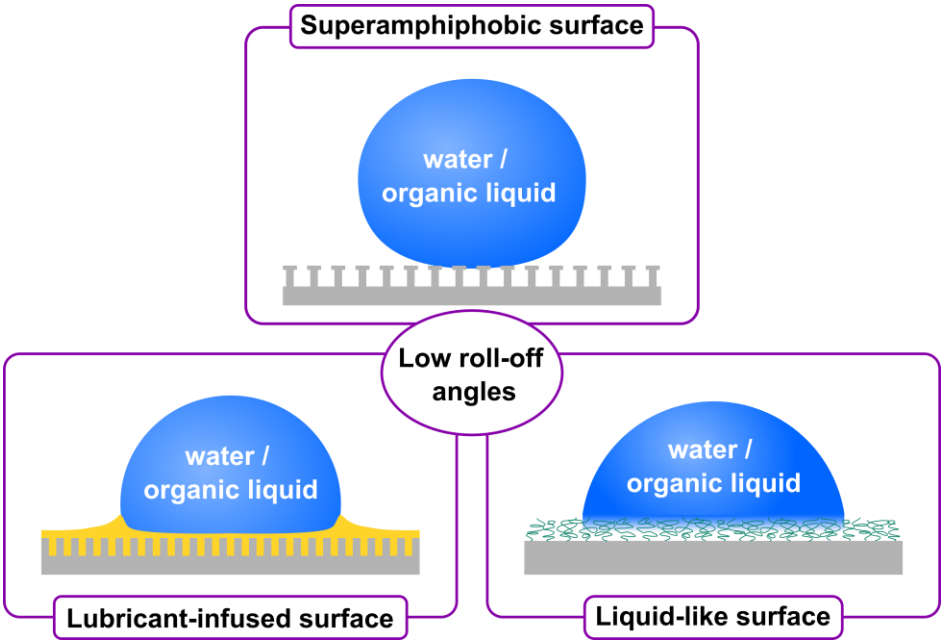

Figure 1.9. Different classes of surfaces where drops exhibit low lateral adhesion: superamphiphobic surfaces, slippery, lubricant-infused, porous surfaces, and liquid-like surfaces. All three types of surface modifications are characterized by low roll-off angles for water and low surface tension organic liquids.

1.4.1 Super-Liquid-Repellent Surfaces

The basic idea of (super-)liquid-repellency was described by Wenzel in the early 19th century and later on by Cassie and Baxter in the mid-20th century. Cassie and Baxter developed an equation to describe super-liquid-repellency on composite surfaces: here, the drop partially rests on air, thereby reducing the solid-liquid interface (Chapter 1.2.2).[16] Surfaces in the Cassie state are characterized by high apparent

contact angles larger than 150° and high drop mobility, i.e. low apparent contact angle hysteresis or roll-off angles of less than 10°. Super-liquid-repellency can be observed in nature, with the lotus leaf being one of the most famous examples (Figure 1.10a-c). Due to the wetting behavior observed on the lotus leaf, the self-cleaning property of super-liquid-repellent surfaces is oftentimes referred to as the lotus effect. In the late 1990s, modern visualization techniques allowed the structural elucidation of the intricate nano- and microstructures found on the lotus leaf.[51,52] At the same time, Tsujii et al.[14,15] published the first artificial superhydrophobic surfaces since the 1940s[53].

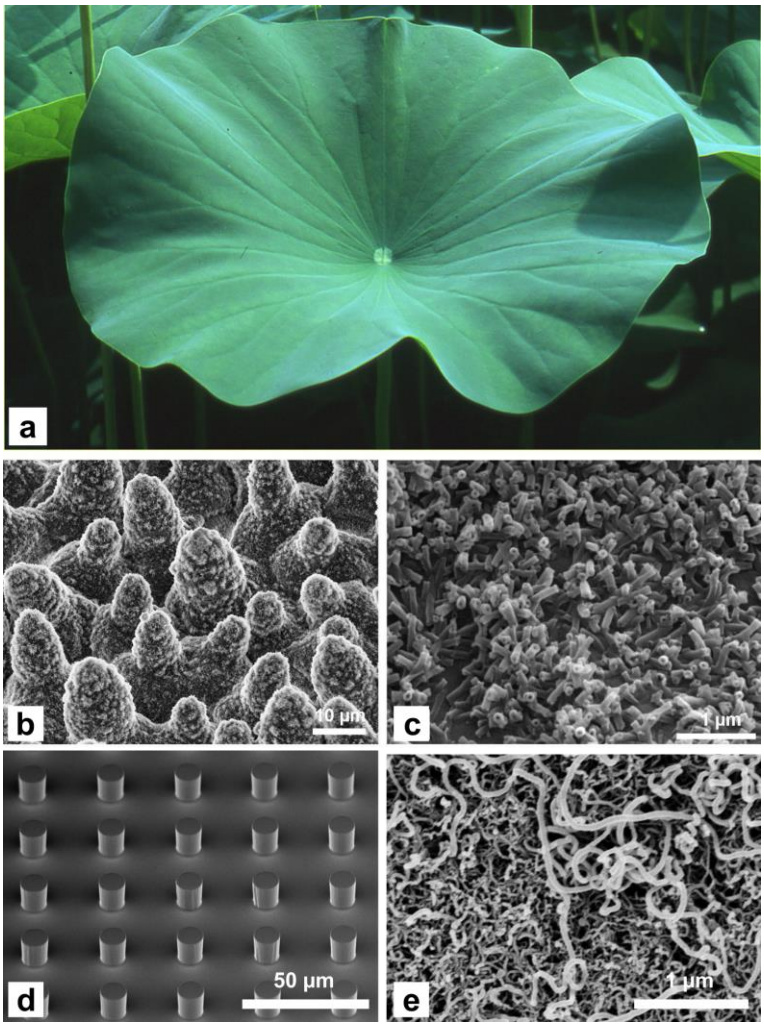

Figure 1.10. a) Optical and b,c) SEM images of a lotus leaf. Reprinted with permission from ref.[54] Copyright 2011, Beilstein Journal of Nanotechnology. Examples for artificial superhydrophobic surfaces: d) a fluorinated regular micropillar array and e) fibrous silicone nanofilaments.

Since then, a great number of superhydrophobic surfaces have been prepared either by top-down or bottom-up approaches and have either relied on the material's inherently low surface energy or on coating

the structures with a hydrophobic layer (Figure 1.10d,e). Various techniques have been used to produce surfaces with roughness on different length scales and from a plethora of materials including photolithography[37,55], spray- or dip-coating[56,57], and electrospinning[58].

Water has a comparatively high surface tension of 72.0 mN m^{-1} and thus, several materials are intrinsically hydrophobic. Nowadays, the fabrication of superhydrophobic surfaces is comparatively straightforward.

Achieving super-liquid-repellency toward low surface tension liquids has proven much more challenging. Oftentimes, a drop resting on the composite solid-air interface is in a metastable state. If the Wenzel state is energetically favorable, liquids that are suspended in the Cassie state may start penetrating the surface structures over time or due to external stimuli.[59] The Cassie-to-Wenzel transition can be caused by two different mechanisms. Either the curvature of the liquid interface touches the underlying substrate (sag impalement) or the liquid-air interface depins from the top sphere and moves down the structure (depinning impalement).[19,38] Capillary forces pull the liquid into the nano- and micropores, oftentimes resulting in superspreading.

To repel low surface tension liquids, it is insufficient to simply roughen a low surface energy material; no planar surface is inherently oleophobic. Instead, structural control on the nano- and micrometer scale is essential. Experiments combined with theoretical approaches have shown the critical parameters for designing stable, super-liquid-repellent surfaces: to increase the robustness of the metastable Cassie state, the distance between surface protrusions, and so-called overhang or re-entrant structures are essential.[19,60,61] Among others, Tuteja and colleagues investigated the critical role of re-entrant geometries and local curvature.[18,62,63] They compared the robustness of the metastable Cassie state for electrospun fibers and micro-hoodoos prepared by a two-step etching process.[18] As a result of the re-entrant geometries, both structures provide sites at which the Young's equation is locally satisfied for any value of $0° < \theta < 180°$ (Figure 1.11a,b). This allows the formation of a composite solid-air interface even for surfaces that do not exhibit intrinsic contact angles of $\theta > 90°$. The Cassie state is only locally stable though.

In the case of the electrospun fibers, the important geometric parameters are the distance D and the radius R of the fibers which can be summarized in a spacing parameter $D^* = (R + D) / R$. This parameter directly affects the solid fraction in contact with the liquid and thus, the apparent contact angle.

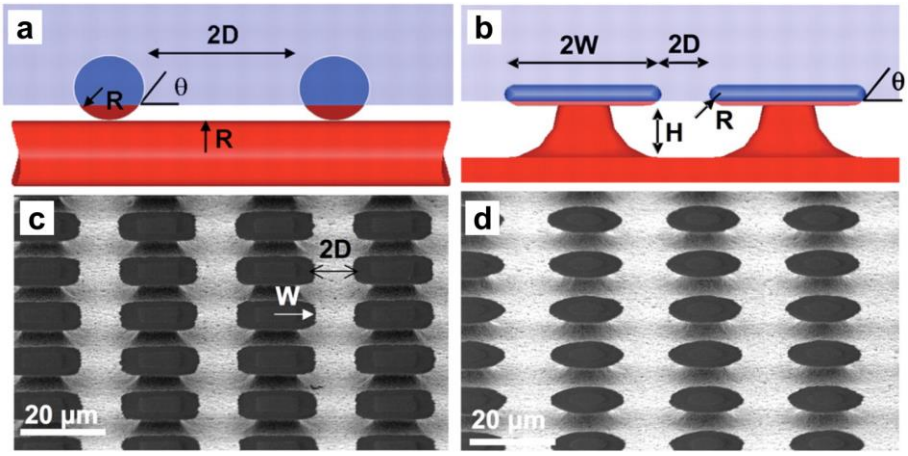

Figure 1.11. a, b) Schematic illustrations of fiber and micro-hoodoo surfaces with re-entrant structures showing the characteristic geometric parameters *R*, *D*, *W*, and *H*. c,d) SEM images showing micro-hodoos with c) square and d) round pillar tops. From ref.[18]. Reprinted with permission from AAAS.

The robustness parameter H^* measures the stability of the Cassie state against applied pressure with respect to the liquid's properties, the apparent contact angle θ, and the surface geometry:

$$H^* = \frac{2(1-\cos\theta)\, R\, l_{cap}}{D^2}. \tag{13}$$

The liquid's properties are represented by the capillary length $l_{cap} = (\gamma_{LA} / \rho g)^{1/2}$.

Varying the geometric parameters R and D has opposing effects on the spacing parameter D^* and the robustness parameter H^*: increasing the distance between fibers while decreasing the fiber radius results in a reduced solid-liquid interface and thus, a higher apparent contact angle. At the same time, the robustness factor is strongly reduced. Therefore, achieving a metastable Cassie state may not be possible on all topographies even if they exhibit re-entrant structures.

Similarly, the spacing parameter D^* for micro-hoodoo arrays is defined as $D^* = [(W + D) / W]^2$ where W is the radius of the pillar tops. Here, the robustness factor is related to the height of the micro-hoodoos H and the local curvature R of the re-entrant geometries:

$$H^* = \frac{2[(1-\cos\theta)\, R + H]\, l_{cap}}{D^2}. \tag{14}$$

The micro-hoodoo structures allow independent tuning of the spacing and the robustness parameters. Hence, the fabrication of surfaces with higher apparent contact angles and a more stable Cassie state is possible.

Since many superhydrophobic and superamphiphobic surfaces are composed of particles, Butt et al. investigated the design principles to achieve a stable Cassie state considering a model surface composed of spheres with a radius *R* (Figure 1.12a).[19] The spheres are partially sintered together, forming pillars that are organized in a regular, two-dimensional array.

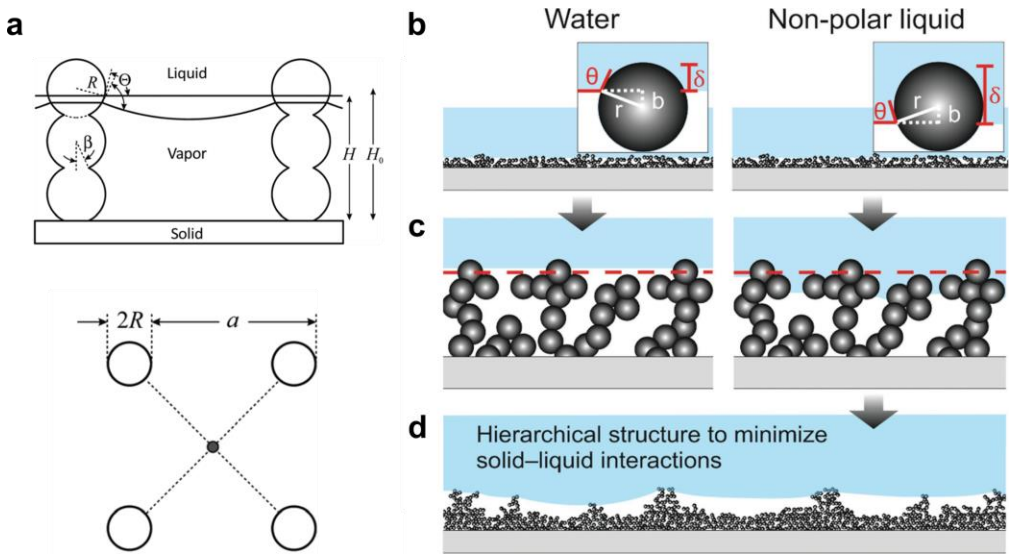

Figure 1.12. a) Schematic illustration of the model surface considered by Butt et al. from side and top view. The pillars are composed of partially sintered particles. Reprinted with permission from ref.[19] Copyright 2013, Royal Society of Chemistry. b-d) Schematic illustration of a particle-based hierarchical model surface wetted by water and a nonpolar liquid. Reprinted with permission from ref.[60] Copyright 2018, John Wiley and Sons.

Similar to the robustness factor *H** proposed by Tuteja, Butt et al. related the maximum pressure difference a liquid in the Cassie state is able to support, to geometric parameters. The critical parameters are the particle radius *R* and A_0, the total area per pillar. For a square lattice unit cell, A_0 is equal to a^2 where *a* is the distance between pillars.

The depinning impalement pressure *P* is given by:

$$P = \frac{2\,\pi\,\gamma\,R}{A_0}\,\sin^2\frac{\theta_{\mathrm{adv}}^{\mathrm{micro}}}{2}. \qquad (15)$$

Here, $\theta_{\mathrm{adv}}^{\mathrm{micro}}$ denotes the microscopic advancing contact angle of a liquid on the particles.

Both Tuteja and Butt show that the radius of and the distance between the surface structures requires careful tuning in order to achieve a stable Cassie state. Generally, the surface should consist of sparsely spaced, highly re-entrant structures.

Figure 1.12b depicts the wetting of a particle-based hierarchical surface by water and a low surface tension non-polar liquid. Local fulfillment of Young's contact angle results in a larger solid-liquid

interface for non-polar liquids. The aggregation of particles into spaced-out, hierarchical structures is essential to reduce the wetted contact area.[60]

Numerous artificial superhydrophobic and superamphiphobic surfaces are composed of spherical structures. Fabrication methods include spray-, dip-, or spin-coating, the deposition of soot from a parafilm flame, or liquid flame spray. A few prominent examples are presented below.

One of the early reported superamphiphobic surfaces is based on a fractal-like, highly porous particle template deposited from the soot of a parafilm flame (Figure 1.13).[61] The carbon nanoparticles with diameters of approximately 40 nm assemble into agglomerates, loosely connected by van der Waals forces. To enhance the mechanical stability, a thin silica shell is added via chemical vapor deposition.

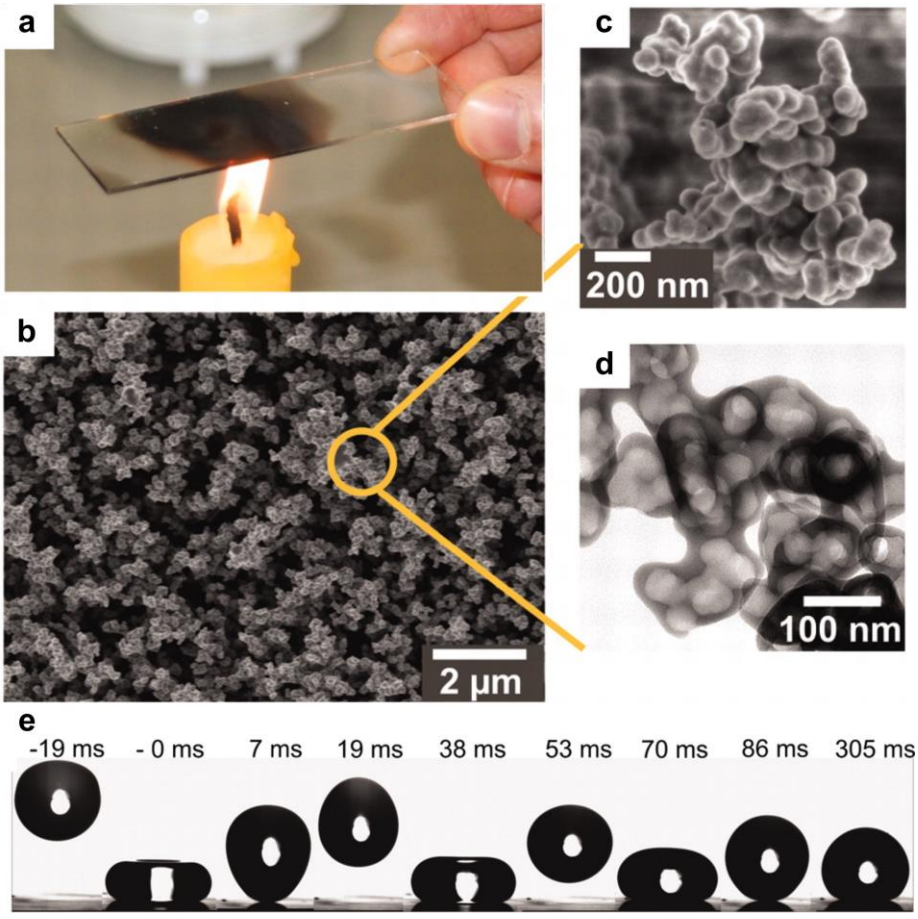

Figure 1.13. a) Deposition of a candle soot template from the flame of a parafilm wax candle. A glass slide is held into the flame until a carbon nanoparticle layer with a thickness of a few micrometers is deposited. b) SEM image of the structures after deposition of a thin silica shell. c) High-resolution SEM image of a particle cluster after removal of the carbon core by calcination. d) High-resolution TEM image of a particle cluster after calcination, revealing a silica shell thickness of 20 ± 5 nm. e) Time-resolved image sequence of a 5 µL drop of hexadecane impinging on a fluoro-functionalized candle soot templated surface. From ref.[61]. Reprinted with permission from AAAS.

Thereafter, the surfaces are calcinated to remove the carbon core, resulting in a transparent, soot-templated silica layer. The silica surface supplies the reactive hydroxyl groups necessary to tune the wetting properties via chemical functionalization. Hydrophobization with fluoro-substances results in superamphiphobic properties; the surface exhibits high static contact angles and low roll-off angles for various liquids and oils. 5 µL drops of hexadecane (27.5 mN m^{-1}) impinging with a velocity of up to v = 1 m s^{-1} easily bounce off the surface and do not penetrate the surface structures (Figure 1.13e). Typically, the drop rebounds twice followed by damped oscillation until it came to rest on the surface in the Cassie state.

Optimization of the mechanical stability while maintaining the superior wetting properties, has been investigated in terms of the deposition distance[64], the silica shell thickness, and the sintering temperatures[65]. However, this method does not allow control of the nanoparticle diameter and the aggregation of particles into three-dimensional structures.

Another technique that relies on the formation of particles in a flame is liquid flame spray, also called flame spray pyrolysis. Here, control of the particle diameter and the statistic collision, aggregation, and coalescence of particles is possible. During the coating process, a liquid feedstock containing the precursor is dispersed into the process gas flame (Figure 1.14a,b). Fine precursor droplets are formed and evaporate. The gaseous precursor is combusted and decomposed by several parallel and consecutive reactions. The gaseous molecules then react to metal oxides and at supersaturation of the gaseous product vapor, particle nucleation takes place. During transport by gas flow within the flame, the particles underlie surface growth, aggregation, agglomeration, and coalescence.[60,66] Thus, the residence time of particles within the hot zone of the flame allows control over the size and density of fractal-like aggregates of nanoparticles.[67–70] At lower temperatures further away from the flame, sintering is suppressed and particles are loosely connected via van der Waals interactions.[60,71] Process parameters such as the particle collection distance, the liquid and gas feed rates, as well as the precursor concentration, influence the resulting surface morphology.[70,72,73] The deposition mechanism can be described via the Peclet number, i.e. the ratio of particle displacement in the advective or orthogonal direction and the stochastically distributed diffusive displacement caused by Brownian motion.[66] At low Peclet numbers, undirected Brownian motion dominates, resulting in the deposition of highly porous particle films (Figure 1.14c).

A range of metallic and organometallic precursors containing for example silicon[68,74], titanium[75,76], or silver[77,78] can be applied. Particle coatings can be collected on virtually every material without previous surface activation, including paper[75–77], fabrics[78], glass[60,74] and flexible plastic films[74]. The wetting

properties can be easily tuned via chemical modifications[60,74] and thus, open up applications in a wide range of fields.

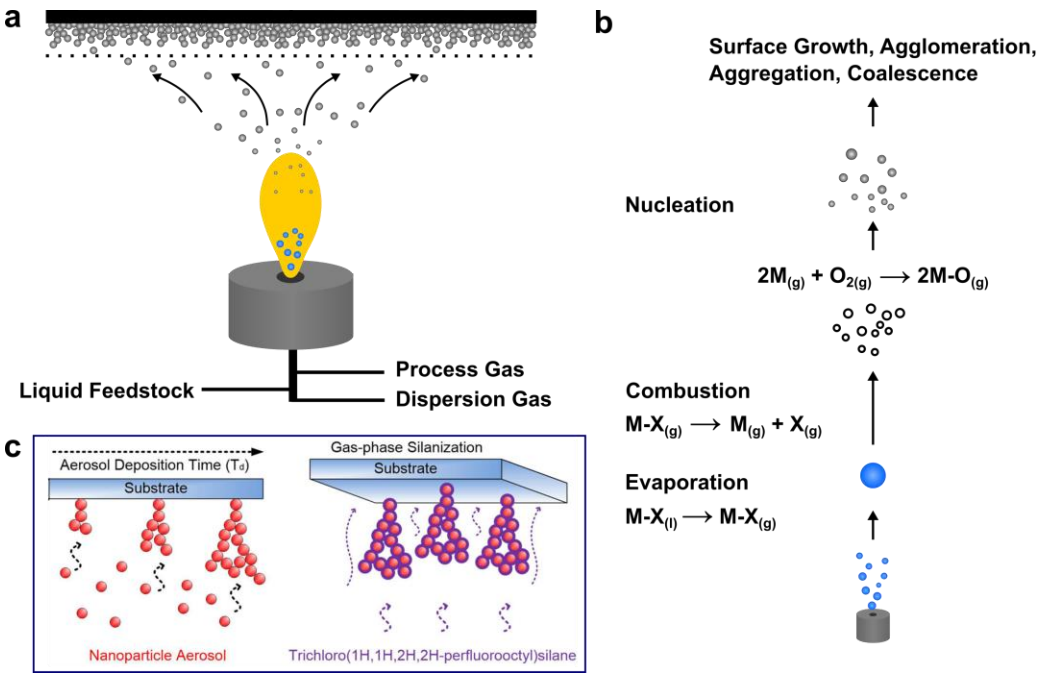

Figure 1.14. a) Schematic illustration of the LFS setup (not to scale). b) The basic steps of particle formation and growth in LFS from an organometallic precursor MX. c) Fabrication of superamphiphobic surfaces: omnidirectional particle assembly and growth of characteristic broccoli-like surface structures followed by functionalization with a fluoro-silane in the gas phase. Reprinted with permission from ref.[74] Copyright 2017, American Chemical Society.

A simple method of producing superamphiphobic particle-based surfaces is by spray coating pre-functionalized particles.[57,79] Here, control of the surface morphology and the extent of re-entrant structures itself is not possible. Rather, as shown by the work of Wong, the loading of crosslinked fluoroalkyl compounds on silica particles can be tuned to influence the surface wettability. The ability of fluorinated trichlorosilanes to form networks is used to gain superamphiphobicity.[57] Depending on the loading of fluorinated trichlorosilanes, spray coating of the pre-functionalized particles resulted in the formation of superhydrophobic or superamphiphobic surfaces. The grafting ratio of the fluorinated trichlorosilane was varied from 1 to 20 µmol m^{-2} with respect to the surface area of silica, reaching a maximum of 54 % w / w. As the maximum number of theoretical silanol groups is 4 µmol m^{-2}, the functionalization is inevitably tuned from a covalent monolayer to a network, formed by self-condensation of the highly reactive trichlorosilanes (Figure 1.15a). To achieve superhydrophobicity, the minimum amount of trichlorosilane of 1 µmol m^{-2} silica is sufficient (Figure 1.15b). This configuration is still wettable by liquids with lower surface tensions, though. To achieve low contact angle hysteresis

and low sliding angles for hexadecane, a ratio of at least 4 µmol m^{-2} is required. If the surface tension is further reduced, densification of fluoroalkyl groups is necessary: for n-decane (23.8 mN m^{-1}), 6 µmol m^{-2} are required. Since this exceeds the maximum number of reactive silanol groups, the formation of a network can be assumed. The formed network is proposed to shield surface -OH groups that remain unshielded in the case of the monolayer grafting approach. This approach circumvents the need for an optimal re-entrant geometry and highlights the importance of sufficient fluoro-loading.

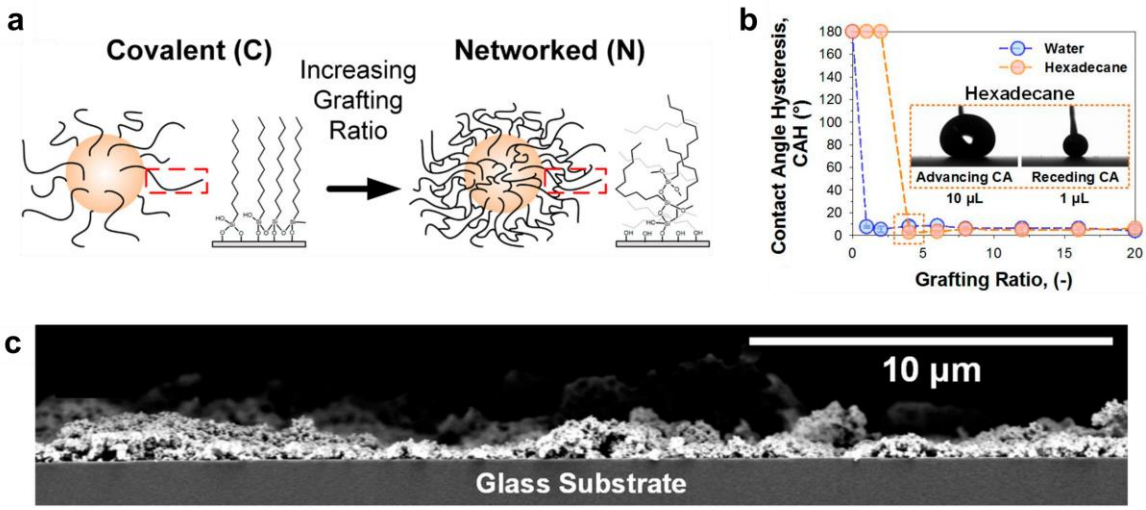

Figure 1.15. a) By increasing the ratio of fluorinated trichlorosilane with respect to the available silica surface area, the surface functionalization is tuned from a covalently bonded monolayer to an oligomeric network. b) Contact angle hysteresis using water and hexadecane on surfaces with increasing fluoro-loadings. c) Side view SEM image of the spray-coated particle surface. Reprinted with permission from ref.[57] Copyright 2019, American Chemical Society.

All the super-liquid-repellent surfaces presented so far rely on two key factors: surface topography, preferentially with optimized overhang or re-entrant morphologies, and low surface energy. Usually, minimization of the surface energy via fluoro-functionalization is a prerequisite for superamphiphobicity. However, there have been growing concerns about the environmental and health effects of perfluorinated compounds.[80] Studies have shown some of them to be persistent, bioaccumulative, and/or toxic. Some materials may affect human health causing, among others, different types of cancer and fertility problems.[81,82] Regulations on the use of perfluoroalkyl substances limit their applicability and have sparked a growing interest in alternatives.

Without the use of fluoroalkyl compounds, optimization of the structure itself is of the utmost importance. So far, only doubly re-entrant structures prepared from silicon dioxide by Liu and colleagues have exhibited superomniphobic properties (Figure 1.16c).[83] These surfaces are able to repel even perfluorohexane with a surface tension of only 10 mN m^{-1}. However, these intricate doubly re-entrant

structures are challenging to produce, and like many other super-liquid-repellent structures, they too suffer from poor mechanical stability.

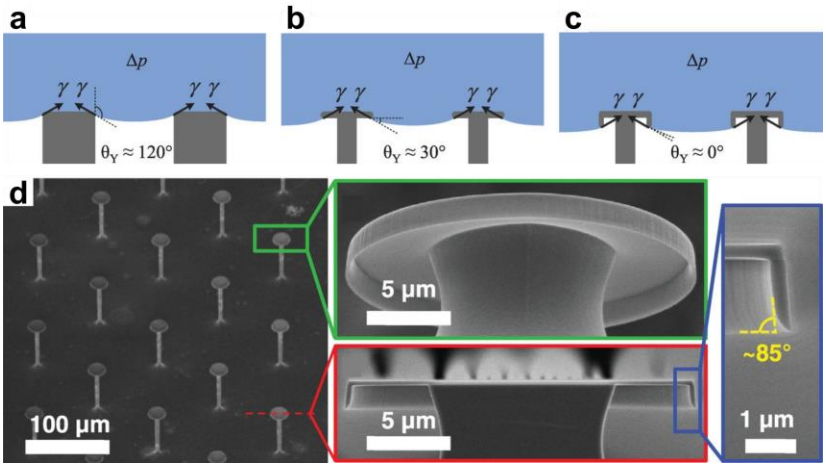

Figure 1.16. Liquids suspended on different surface morphologies. Schematic illustration of a) simple structures that rely on chemical contact angles of θ > 90°, b) re-entrant structures that allow chemical contact angles of 0 < θ < 90°, and c) doubly re-entrant structures that allow chemical contact angles of θ ≈ 0°. d) SEM images of SiO_2 microposts with doubly re-entrant structures. From ref.[83]. Reprinted with permission from AAAS.

1.4.2 Slippery, Lubricant-Infused, Porous Surfaces

Alternatively, the air between the structures can be replaced with a second, immiscible liquid (Figure 1.17a). These types of surfaces are known as slippery, lubricant-infused, porous surfaces or lubricant-impregnated, slippery surfaces (LubISS). The lubricant forms a smooth, chemically homogeneous film, acting as the repellent surface and thereby, reducing solid-liquid friction.[84,85] Generally, a wide range of structures can be used to hold the lubricant in place by capillary forces. Typically, surfaces are chemically modified to increase the affinity to the lubricant. In any case, they must be preferentially wetted by the lubricant rather than by the liquids that are to be repelled. Furthermore, the lubricant must be immiscible with the test liquids.[20–22] SLIPS are inherently self-healing; even macroscale damage to the substrate by impact or abrasion is repaired by a spontaneous flow of the lubricant to the damaged sites. Within milliseconds, defect-free behavior of the surfaces can be restored.[22]

Among the first to propose this concept for liquid-repellency, Aizenberg et al. examined two types of rough surfaces: an ordered array of epoxy-based, fluorinated nanopillars and random Teflon nanofibers (Figure 1.17b).[22] The structures were infiltrated with low surface tension, chemically inert,

perfluorinated lubricants. They reported negligible contact angle hysteresis and low roll-off angles for different low surface tension and complex test liquids.

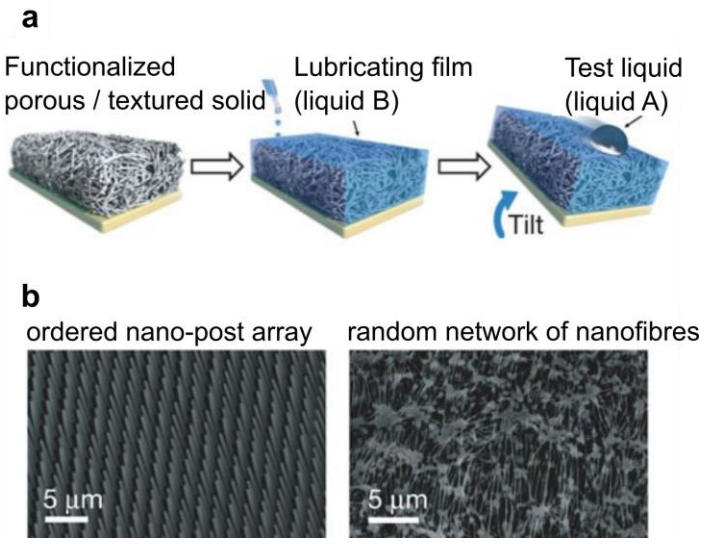

Figure 1.17. a) Schematic illustration of the fabrication procedure of slippery, lubricant-infused, porous surfaces: a functionalized porous or textured surface is infused with a suitable lubricant (liquid B), resulting in the formation of a smooth, homogeneous lubricating film that easily repels the test liquid A. b) SEM images showing the morphologies of suitable underlying surface structures. Reprinted with permission from ref.[22] Copyright 2011, Nature Publishing Group.

One of the greatest challenges to the real-life application of SLIPS is the depletion of lubricant. Multiple mechanisms, including gravitational damage, liquid cloaking or wetting ridge formation, and shear flow contribute to the depletion of lubricant (Figure 1.18).[86] Apart from enhanced chemical compatibility with the lubricant, optimization of the underlying surface morphology may reduce lubricant loss.

Recently, Baumli and Teisala et al. proposed a solution to the issue of lubricant depletion in a shear flow: here, a shear-resistant lubricant-infused surface was achieved by flow-induced self-lubrication of the substrate from an oil-in-water emulsion streaming over the substrate.[23]

Overall, exceptional surface properties such as self-cleaning and anti-biofouling were achieved using SLIPS. The problem of lubricant depletion, however, challenges the practical applicability.[20,87,88]

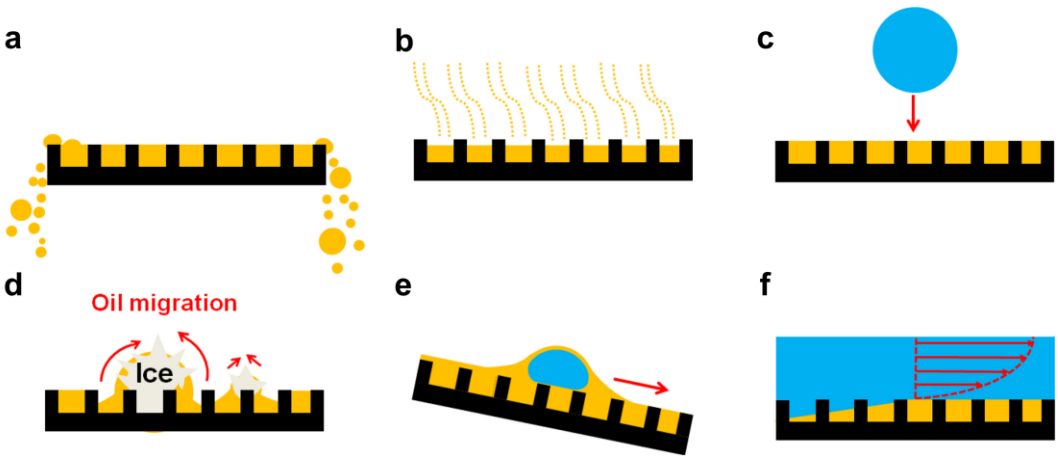

Figure 1.18. Mechanisms leading to lubricant depletion: a) gravitational drainage, b) lubricant evaporation, c) drop impact, d) oil migration on frost, e) formation of a cloaking layer on a drop that is repelled by the surface, and d) lubricant depletion under shear flow. Reprinted with permission from ref.[86] Copyright 2020, Elsevier B.V.

1.4.3 Liquid-Like Surfaces

Another approach toward low lateral adhesion and low roll-off angles are so-called liquid-like surfaces. Here, one end of a flexible polymer chain is covalently bonded to a surface. The most well-known example of a liquid-like coating is prepared using polydimethylsiloxane (PDMS). PDMS is well suited for a wide range of applications as it is biocompatible, non-toxic, and cheap. Most important for the application in liquid-repellency is the low surface energy of 20 mN m^{-1}.[89] PDMS coatings have been applied to smooth substrates such as glass and silicon wafers. Upon functionalization, they exhibit hydrophobic or even omniphobic properties with negligible contact angle hysteresis for a variety of liquids.[50,90–94] For example, coatings prepared by Wang and McCarthy exhibit a contact angle hysteresis of less than 1° for 4 µL drops and roll-off angles of less than 3° for 3 µL drops of hexadecane.[50] The coatings are prepared through acid-catalyzed graft polycondensation of dimethyldimethoxysilane (Figure 1.19c). Overall, there are several methods to covalently graft PDMS chains to a surface. Depending on the reactivity of the precursor, in solution, the reaction can occur with[50] and without a catalyst[95]. The synthesis can also be conducted in the gas phase.[92,96] Finally, PDMS itself is reactive: coatings have been produced from silicone oil under UV illumination[97,98], at elevated temperatures[99], and even at ambient temperatures[91] The wetting behavior of these surfaces is not only based on the low surface energy of PDMS: it also relies on the rheological properties of the tethered PDMS chains. Due to the low glass transition temperature, PDMS is a polymer melt at room temperature. The siloxane

backbone of grafted PDMS chains exhibits nearly vanishing torsional barriers and the polymers are free to bend and/or rotate.[94,96,100,101]

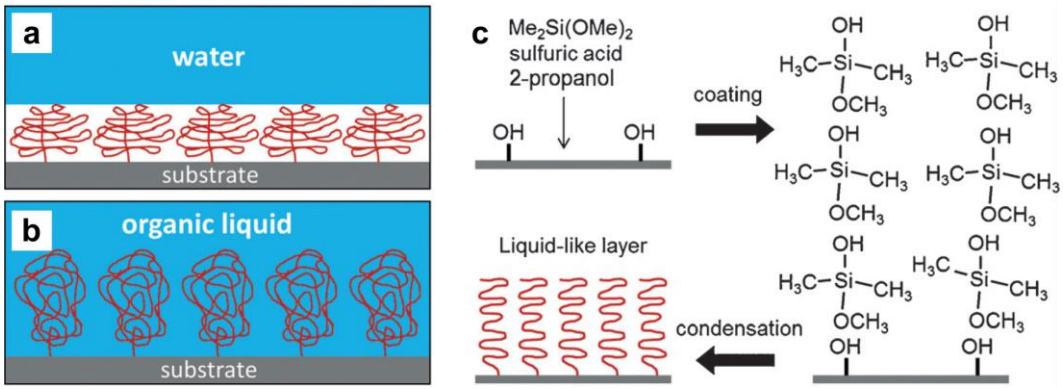

Figure 1.19. Sessile drops of a) water or b) organic liquids on a PDMS brush liquid-like surface. c) Rapid acid-catalyzed graft polycondensation of PDMS. Reprinted with permission from ref.[102] Copyright 2016, WILEY-VCH Verlag GmbH & Co. KGaA, Weinheim.

It has been observed that for some liquids, drops spread on the surface and form low static apparent contact angles. At the same time, excellent dynamic dewetting, i.e. low roll-off angles are observed.[35,103] McCarthy[50] and Hozumi[35] attributed this wetting behavior to the liquid-like properties of surface-tethered PDMS chains. With high surface tension liquids, a discrete liquid-liquid interface between PDMS and the probe liquid is expected to form (Figure 1.19a). With increasing compatibility between the two components, for example for low surface tension oils, the PDMS layer swells and blends with the probe liquids (Figure 1.19b). On smooth surfaces, increased interactions with the probe liquid result in enhanced liquid-like properties of the PDMS chains and finally, improved dynamic dewetting.

Smooth PDMS-grafted surfaces have exhibited high wear tolerance against scratching, taping, and rubbing.[91,95] Furthermore, they have shown high durability under high-temperature, water vapor, and acid treatment.[95,104] Recently, Golovin et al. presented a crosslinking procedure that allows further improvement of the mechanical properties of PDMS.[104] However, while crosslinking results in enhanced mechanical durability, the flexibility and thus, the liquid-like behavior of the PDMS chains deteriorates. For industrial applications of PDMS-grafted surfaces, a balance between these surface properties is necessary.

1.5 Application of (Super-)Liquid-Repellent Surfaces

Surfaces with high drop mobility are most well known for their self-cleaning abilities. Macroscopic contaminations resting on top of the rough surface features or on smooth liquid-repellent surfaces are easily removed by drops rolling over the surface.[21,105,106] The effect has long been observed on naturally occurring surfaces such as the Lotus leaf.[51] Over the last few decades, different strategies to produce artificial contamination-free surfaces have been explored. Apart from self-cleaning, the resistance against the accumulation of contaminations is also essential for applications in drag-reduction[107,108], membranes for gas exchange[109], anti-fogging, and the fabrication of waterproof textiles[110].

Another highly desirable application for artificial (super-)liquid-repellent surfaces is the suppression or the delay of biofilm formation. Biofilm formation describes the accumulation of bacteria, cells, and microorganisms on solid surfaces upon exposure to water or biological fluids. They can cause a variety of problems ranging from colonization of medical devices and infection of tissues to pollution of air filters and air-conditioning systems.[111,112] Commercial treatments include the use of biocides and antibiotics. However, environmental concerns and increasing resistance of bacteria limit long-term applicability and stress the requirement for coatings that deter organisms from attaching in the first place.[112,113] Super-liquid-repellent surfaces have been observed to prevent biofouling by reducing the solid-liquid interface.[114–116] The bacterial suspension rests only on the tips of the surface protrusions, therefore offering only few anchoring points for bacteria to attach to. The long-term application of super-liquid-repellent surfaces is challenged by the stability of the Cassie state, though.[117] Over time or due to changes in temperature or pressure, the suspension may penetrate the surface structures. Furthermore, the use of surfaces relying on a fluoro-functionalization may be limited due to environmental and health concerns. Lubricant-infused surfaces utilize a different mechanism to reduce bacterial adhesion: Epstein et al. showed that owing to the mobility of the slippery interface, the formation of common bacteria biofilms can be reduced by up 99 % on polytetraefluoroethylene infused surfaces.[118] For biomedical applications, SLIPSs infused with biocompatible, non-toxic silicone oil are suitable candidates.[119]

Another promising approach to prevent biofilm formation relies on the use of a well-chosen surface morphology in the wetted state.[120] Inspired by the bactericidal effect observed on some naturally occurring surfaces such as the wings of a dragonfly, Ivanova et al. have developed artificial surfaces with high aspect ratio nanoprotrusions (Figure 1.20a,b).[121–123] The nanostructures reduce biofilm formation by presenting unfavorable binding sites and mechanically lysing bacterial cells that come into contact ith the surface. Encinas et al. showed that on silicone nanofilaments, bacterial adhesion can be reduced in

the Cassie as well as the wetted state (Figure 1.20c-e). Presumably, the spacing of the three-dimensional fibrous structures falls just below the size of the bacteria, effectively suppressing bacterial adhesion in the wetted state.[124,125]

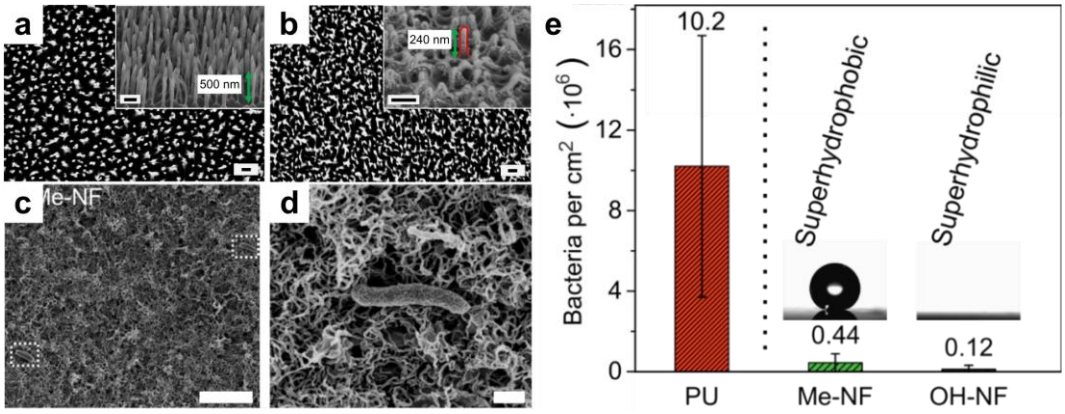

Figure 1.20. Bactericidal effect: SEM images of a) artificial black silicon and b) the wings of a dragonfly. Scale bars: 200 nm. Reprinted with permission from ref.[123] Copyright 2013, Springer Nature. c-e) Antibacterial properties of silicone nanofilaments after 168 h incubation in an *E. coli* solution. Scale bars: c) 20 µm; d) 4 µm. e) Average number of bacteria per area adhered to bare PU and silicone nanofilaments in the superhydrophobic and wetted state. Reprinted with permission from ref. [125] Copyright 2018, WILEY-VCH Verlag GmbH & Co. KGaA, Weinheim.

Another relevant feature of some (super-)liquid-repellent surfaces are anti-icing properties. The formation of frost and accumulation of ice can detrimentally affect the efficiency and operational safety of wind turbines, air crafts, power lines, or antennas.[126,127] For example, ice formation on aircrafts from supercooled water drops greatly affects the performance of aerodynamic surfaces. A number of surface modifications have been investigated toward their ability to either prevent frost and ice formation or facilitate the removal of ice.[8,128,129] Super-liquid-repellent surfaces have been proposed for easy ice removal due to low ice adhesion strength.[7] The large-scale and long-term application is typically limited by the mechanical stability of these surfaces. Lubricant-infused surfaces also exhibit ultralow ice adhesion. However, due to the strong capillary suction pressure exerted by growing frost dendrites, lubricant is depleted from the structures, and eventually, contact with the underlying solid structures may be established.[9,130,131] Again, the long-term application of SLIPS is challenged by lubricant depletion by water drops, frost, and accreted ice removal.

2 Ultrafast Bubble Bursting by Superamphiphobic Surfaces

Katharina I. Hegner, William S. Y. Wong*, and Doris Vollmer*

Physics at Interfaces, Max Planck Institute for Polymer Research, Ackermannweg 10, 55128 Mainz, Germany

E-mail: wong@mpip-mainz.mpg.de and vollmerd@mpip-mainz.mpg.de

Keywords: superamphiphobic surfaces, aerophilic surfaces, bubble bursting, bubble rupturing, liquid flame spray, defoaming, flotation

The Supporting Information is available from wiley.com:

https://onlinelibrary.wiley.com/doi/10.1002/adma.202101855

Abstract

Controlling bubble motion or passively bursting bubbles using solid interfaces is advantageous in numerous industrial applications including flotation, catalysis, electrochemical processes, and microfluidics. Current research has explored the formation, dissolution, pinning, and rupturing of bubbles on different surfaces. However, the ability to tune and control the rate of bubble bursting is not yet achieved. Scaling down surface-induced bubble bursting to just a few milliseconds is important for any application. In this work, we tuned the hierarchical structure of superamphiphobic surfaces in order to rapidly rupture contacting bubbles. Surfaces prepared using liquid flame spray show ultrafast bubble bursting (down to 2 ms) and superior durability. The coatings demonstrate excellent mechanical and chemical stability even in the presence of surface-active species. Air from the ruptured bubble is absorbed into the aerophilic Cassie state. We demonstrate long-term applicability by preventing accumulation of air in the plastron *via* a connection of the plastron to the environment. The times recorded for bubble rupture and complete reorganization of air are reduced by approximately a factor of 3 compared to previously reported values. The concept is utilized to passively control surfactant-rich foam in froth flotation. Material collection efficiency increased by a factor of 25 compared to controls.

2.1 Introduction

Bubble attachment and accumulation challenge a wide variety of industrial applications. For instance, in the fast-growing field of electrocatalysis for clean energy production, gas bubbles evolving on the electrodes block the effective catalytic sites.[132–135] At a larger scale, the chemical, water, and food processing industry often face the challenge of foam accumulation, which can lead to processing problems and reduced product yields.[136–138] In froth flotation, used in wastewater treatment[139,140] and mineral-mining industries[141,142], control of air bubbles and froth carrying hydrophobic particles from a slurry is essential for facilitating a cost-effective separation process.[138] Therefore, methods to improve control of ultrafast bubble bursting or froth are highly desirable.

Current research has focused mainly on understanding bouncing[143], pinning[144,145], spreading[146,147], and the transport[134,148] of bubbles. Wang *et al.* demonstrated bubble bursting and absorption on artificial hierarchical lotus leaves within tens of milliseconds.[149] On the contrary, on dense superhydrophobic nanowires, the bubble remained pinned. Rapoport *et al.* showed that localized microscale protrusions allow faster drainage of the liquid film separating the bubble and the protrusion.[143] When combined, these studies suggest that tuning a hierarchical and microscopically rough texture is vital toward achieving ultrafast bubble capture.[143,149]

However, current state-of-the-art surfaces remain comparatively slow in bubble capture (approximately 13 ms[143,149]) and are seemingly at their performance limit. Scalable coating methods with long-term performance are required for industrial applications. Furthermore, the mechanism for passively inducing rapid bubble bursting and air absorption is still unclear. Film thinning models suggest that features should be as small as possible to enhance bubble bursting.[150] However, the required tunable nanoscale architectures were not easily attained, until the recent advent of liquid flame spray (LFS)-based superhydrophobic / superamphiphobic surfaces.[60,74] LFS is an extremely fast and versatile coating technique that allows for tuning of surface structures and contacting protrusions at the micro- and nano-scale.[60,67,69] Therefore, it enables a deeper investigation into the surface morphology required for ultrafast bubble rupturing.

Here, we present the design principles of surface-immobilized aerophilic superamphiphobic coatings capable of ultrafast passive bubble bursting. Superamphiphobic coatings produced *via* LFS are benchmarked against surfaces developed by wet-spray coating and superhydrophobic silicone nanofilaments. On optimized LFS coatings, bubbles were fully absorbed by the aerophilic structures in less than 4 ms after contact in water. Compared to previously reported results, we were able to reduce

the time required for bubble rupture and air absorption by approximately a factor of 3.[143,149] In C12E5 soap solution, bubble rupturing required a maximum of 75 ms. Long-term performance was demonstrated by providing a continuous pathway for excess air to escape into the environment.

Rough, porous microstructures coupled to the smallest possible particulate nanostructures with diameters below 100 nm appear to provide the optimal surface properties for ultrafast bubble rupture. We applied these findings to passively control froth flotation and increased the material collection efficiency by a factor of 25.

2.2 Results and Discussion

To understand the influence of surface morphology and topography on bubble bursting, we fabricated superamphiphobic and superhydrophobic model surfaces based on particulate or fibrous structures (Figure 2.6).

On a superhydrophobic surface only the very tips of the surface structures (i.e. protrusions) are in contact with water. Superhydrophobicity is achieved by a combination of surface roughness and low surface energy.[19,151] By introducing overhanging, so-called re-entrant geometries, superamphiphobic surfaces are able to repel even low surface tension liquids.[18,61] When immersed in a liquid, the plastron (air layer) renders the surface aerophilic.[147]

Particle coatings were produced either *via* LFS or by wet-spray coating, hereafter called liquid flame spray (Figure 2.1a-d) and dense nanoparticle coating[57] (Figure 2.1e), respectively. For comparison, fibrous silicone nanofilaments[152,153] were investigated (Figure 2.1f).

Unlike many other coating techniques, LFS allows for the precise control of particle size and coating morphology by tuning of the process parameters.[60,67,69] A liquid feedstock containing the precursor, here tetraethoxysilane (TEOS) in isopropanol, is injected into a process gas flame (Figure 2.1g, Methods for details). After evaporation of the liquid phase, the precursor reacts and nucleates in the flame. Depending on the residence time of the particles in the flame, particles grow, agglomerate, and sinter until they arrive at the substrate, assembling into a highly porous particle network connected by van der Waals forces.

The morphology of resulting silicone dioxide coatings is influenced by the position of the substrate with respect to the burner (d_{burner}) and the coating time. Decreasing the coating distance from 52 cm to 22 cm at a constant coating time of 10 min led to an increase in film thickness from *ca*. 20 µm to 75 µm (Figure 2.1a-d). To stabilize the porous structures and to improve adhesion with the substrate, a silica shell was deposited by chemical vapor deposition (CVD) of TEOS.[65] The surface energy was lowered by fluoro-functionalization *via* CVD. Independent of the LFS process parameters, all surfaces show

exceptional wetting properties with roll-off angles for low surface tension *n*-hexadecane (27.5 mN m^{-1}, 6 µL) of < 2° (Figure 2.1h). Figure 2.1e shows a surface prepared by wet-spray coating of fluoro-functionalized silicone dioxide nanoparticles.[57] During wet-spray coating, the functionalized particles formed aggregates with a diameter of 62 ± 13 nm. Compared to LFS coatings, much denser geometries can be discerned, hence the term dense nanoparticle (DNP) coating. The wetting properties of the DNP surface are comparable to the porous LFS nanoparticle coatings, i.e., *n*-hexadecane drops roll off when tilting the surface by approximately 3°. To produce superhydrophobic silicone nanofilaments (SNF) a glass slide was immersed in a solution containing trichloromethylsilane (TCMS) and toluene with trace amounts of water.[152] The resulting fibers have a diameter of 33 ± 13 nm (Figure 2.1f). Upon fluoro-functionalization, the roll-off angle for *n*-hexadecane is 24° ± 3°.

We immersed the surfaces into environmentally-equilibrated milli-Q water or C12E5 surfactant solution. The distance between the needle and the surface was fixed at 2.5 mm. A bubble with a radius of 0.9 mm was produced using a syringe pump. We recorded bubble impact using a high speed camera (Figure 2.1i). The bubble was then tracked using custom image-processing algorithms (edge detection) in MATLAB, where the velocity of the 2D center-of-mass was computed. The bubble approached the surface with a velocity of up to 0.14 m s^{-1}. From the bubble velocity we reconstructed the moment of first contact between the bubble and the surface, corresponding to the minimum decelerated velocity (Figure 2.1j). We define this time as t_0. The sharp increase in velocity detected when the bubble is ruptured by the surface, followed by rapid absorption of air by the coating, is defined as t_1. At t_1, air from the ruptured bubble is absorbed by the surface but not yet fully reorganized (see second to last optical image in Figure 2.1i). The rupturing time t_r is the difference between t_1 and t_0 and is used as a quantitative measure of the bubble bursting property of a surface.

In Figure 2.1j, two possible scenarios are depicted (Supplementary Videos M1 and M2). The blue dataset depicts the velocity of a bubble that bounces off a surface multiple times. Bubble rebound corresponds to negative velocities. Finally, the bubble slows down and eventually comes to rest. After 175 ms, the bubble ruptures spontaneously. The air is rapidly absorbed into the air layer within the surface structures, resulting in the sharp increase in velocity.

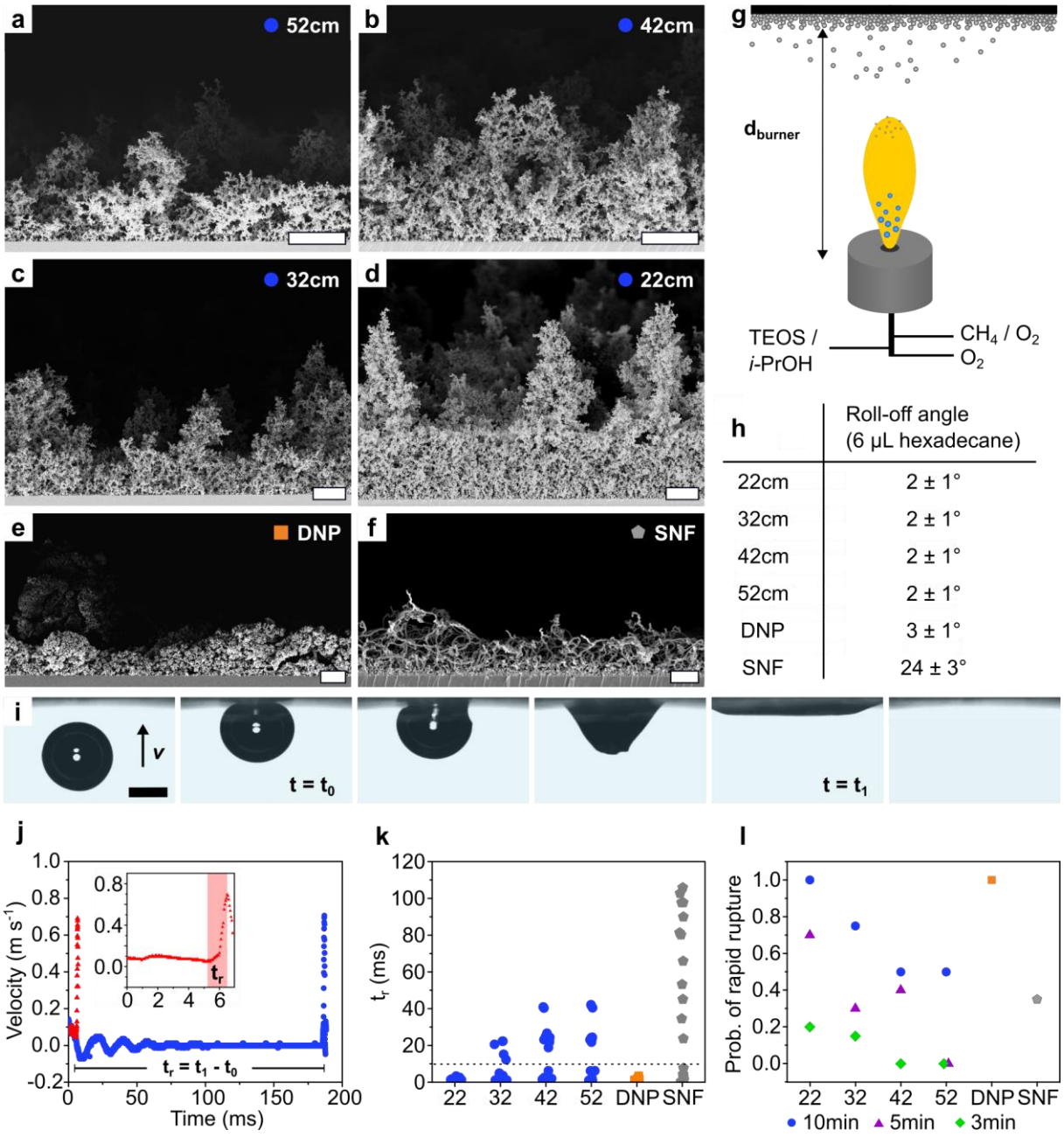

Figure 2.1. Side-view scanning electron microscopy (SEM) images of a-d) LFS surfaces coated at different distances to the burner for 10 min (scale bars are 10 µm), e) a dense nanoparticle coating, DNP (scale bar is 2 µm), and f) silicone nanofilaments, SNF (scale bar is 1 µm). g) Schematic illustration of the liquid flame spray setup (not to scale). h) Roll-off angles using 6 µL droplets of n-hexadecane as a probe liquid. i) Images acquired by a high-speed camera (scale bar is 1 mm) showing an air bubble rupturing immediately upon contacting the surface. j) Bubble velocity as a function of time, depicting two different scenarios of how 1) a bubble ruptures immediately upon impact (red dataset, inset) and 2) a bubble may also bounce off a surface multiple times before coming to rest and finally rupturing spontaneously. k) Rupturing times of bubbles rising in water against 20 different spots on pristine surfaces. l) Probability of rapid rupture (< 10 ms) upon first contact.

The red dataset shows the case of a surface inducing bubble bursting immediately upon contact, so-termed ultrafast bubble bursting. The bubble does not even slow down to zero velocity before rupture (see inset). Bubble rupturing requires less than 2 ms. Only 4 ms after the first bubble-to-surface contact, the air is fully absorbed and reorganized by the structure (see last optical image in Figure 2.1i). The rate at which air is absorbed into the structures is independent of the rupturing time and the type of surface used (see Supporting Information Figure 2.9 for velocity graphs).

Figure 2.1k depicts the time required for bubbles to rupture upon contacting LFS surfaces (blue circles) produced at different coating distances (d_{burner}), as well as the single-configuration DNP (orange square) and SNF surfaces (grey pentagons). A minimum of 20 experiments (i.e. 20 different spots) was conducted per surface. After each bubble, the surface was removed from the liquid, allowing dissipation of absorbed air. We observe an influence of LFS process parameters on the bubble rupturing time. Bubbles contacting a surface coated for 10 min at 22 cm distance to the burner always rupture immediately upon first contact with rupturing times well below 10 ms (see dotted line). For coating distances exceeding 22 cm, bubbles can rebound and oscillate, as reflected by the time intervals between data clusters. Surfaces coated at 52 cm distance induce rupturing upon first contact in only 50 % of all experiments.

To provide additional insight on the effect of coating thickness and morphology, we decreased LFS coating times from 10 min, to 5 min, and 3 min and the coating distance from 52 cm to 22 cm (see Figures 2.11 and 2.12 for surface morphology and Figure 2.13 for t_r at different coating times). Unlike LFS coatings, DNP and SNF surfaces are not tunable.

To facilitate concise comparison between all surfaces, we calculated the probability of rapid rupture (Figure 2.1l). We define rapid rupture as a t_r of less than 10 ms upon first contact between the bubble and the surface (see dotted line in Figure 2.1k). For LFS coatings, the probability of rapid rupture increases with increasing coating time and decreasing coating distance (Figure 2.1l). Per Figure 2.1k and Figure 2.1l, the DNP coating (orange squares) also shows bubble rupturing well below 10 ms. Compared to nanoparticles, the smoother silicone nanofilaments (grey pentagons) are less suitable for consistently reliable rapid bubble rupturing. Larger bubble-to-surface contact area and higher flexibility of the nanofilaments might have induced rupturing times ranging from 2 ms to 110 ms. This hints that sharp particulate structures are favorable. Based on these results, it appears that the macroscopic morphology of the coating and the size of individual particles both play crucial roles in inducing bubble rupturing.

To understand the relation between the hierarchical structures and bubble rupturing, we investigated the influence of process conditions on LFS coatings. The size of individual nanoparticles is expected to increase with increasing coating distance due to a longer residence time of particles in the hot zone. This

allows particles to further grow and sinter.[67,69] Indeed, we observe a trend in particle diameter with the coating distance (Figure 2.2a and b). The particle diameter decreased from 126 ± 18 nm to 79 ± 14 nm when the coating distance was reduced from 52 cm to 22 cm. The DNP coating is composed of nanoparticle aggregates with a diameter of 62 ± 13 nm (Figure 2.2c). This hints that the effective bubble rupturing capabilities of LFS (22 cm) and DNP surfaces are caused by the ultrafine nanoparticle and nanoparticle aggregate diameter, respectively. These observations raise the question, how the tunable nanoscale configuration influences the time required for bubble rupturing. In the left panels in Figure 2.2d, the bubble approaches a coating with prominent surface protrusions made up of particles with radii r_1. In contrast, the right panels illustrate larger nanoparticles with radii r_2, where $r_2 > r_1$.

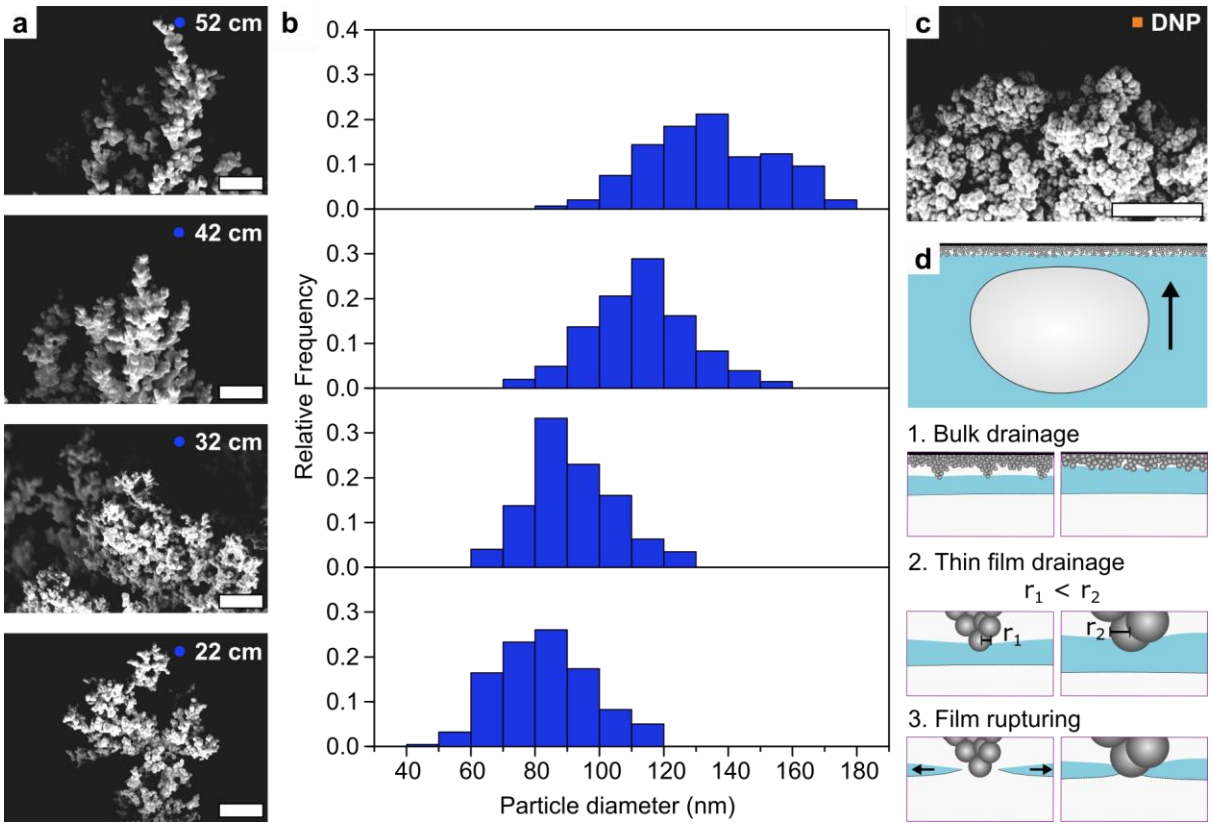

Figure 2.2. Effect of surface morphology on bubble rupturing. a) Side-view SEM images of LFS surfaces coated at decreasing distances to the burner (scale bars are 1 µm) and b) corresponding particle size distributions. c) Side-view SEM images of a DNP surface (scale bar is 1 µm). d) Schematic illustration of the bubble rupturing mechanism on nanoparticles with r1 < r2 (not to scale).

Upon bulk drainage, film thinning between the flattened bubble and the surface continues. The liquid film is squeezed between air from the bubble and an aerophilic particle. The smaller the protrusion, the higher the imposed pressure gradient which increases the force pushing liquid out of the thin film.

Additionally, less liquid needs to be moved from in-between the bubble and the particle.[154] Eventually, the particle protrusion pierces the film and establishes a three-phase contact line with the bubble. As soon as the particle pierced the film, a pressure gradient in the film within close proximity of the particle pushes the liquid away. The three-phase contact line of the bubble's air-liquid-solid interface migrates along the particle surface, maintaining its receding contact angle. Eventually, the film has thinned sufficiently that the two contact lines meet and merge (see last panels in Figure 2.2d). In this secondary process of contact line motion, the individual particle size also influences the rupturing time: a smaller particle circumference leads to a reduced length of the migrating contact line and hence, reduces possible pinning events. Our experimental findings concur with these coupled mechanisms, where bubble rupturing occurs faster on coatings having a distribution of smaller particles.[154,155]

Apart from particle size, particle aggregation and hierarchy appear to influence bubble rupture. We tuned surface hierarchy by varying the coating times at constant coating distances, thus maintaining constant particle diameters. With shorter coating times, more uniform particle networks are observed (Figures 2.11 and 2.12). In contrast, highly porous protrusions become more pronounced with increasing coating times. The rougher, more widely dispersed hierarchical structures greatly reduce the solid-liquid contact area which increases the slip length and reduces the friction the liquid film experiences.[19,156] This enhances the film thinning velocity and accordingly the rate at which contact lines of neighboring protrusion can meet and merge in case of multiple points of bubble rupture. In line with reduced rupture times, rough and widely dispersed protrusions increase the probability of a bubble contacting individual particles or smaller particle aggregates, facilitating to pierce the liquid film. Collectively, these parameters reduce the bubble bursting time and allow faster absorption of the bubble into the surface structures.

Although these results are highly promising, one might speculate about the long-term performance of such coatings because of the gradual accumulation of air from ruptured bubbles. To understand the consequences of air accumulation within the coating (i.e. an increased thickness of the air plastron), bubbles were repeatedly ruptured on the same location. The captured air was not removed between tests. To visualize the effect, results for a sub-optimal LFS coating produced at a distance of 52 cm with a thickness of 20 µm are presented (Figure 2.3a). Conceptually, the same holds for the other investigated coating parameters and surface modifications (Figure 2.14).

For the LFS coating presented here, the rupturing times increased with an increasing number of bubbles captured, from approximately 35 ms to 200 ms (Figure 2.3a and Figure 2.14 for performance of LFS

coatings produced at different process conditions and single configuration DNP). With every rupturing event, air from the bubble is absorbed into the air layer of the superamphiphobic structure (Figure 2.3b). Each bubble adds an air volume of approximately 3 µL. The air layer gradually builds up in thickness, effectively preventing direct bubble-to-particle contact. Subsequent bubbles contacting this swollen air layer encounter a flexible interface that delays rupture, akin to bubble-to-bubble[157] contact. After absorbing 100 bubbles, the captured air was released into the environment. Thereafter, the surface recovered its rupturing time, demonstrating its functional durability (Figure 2.3a).

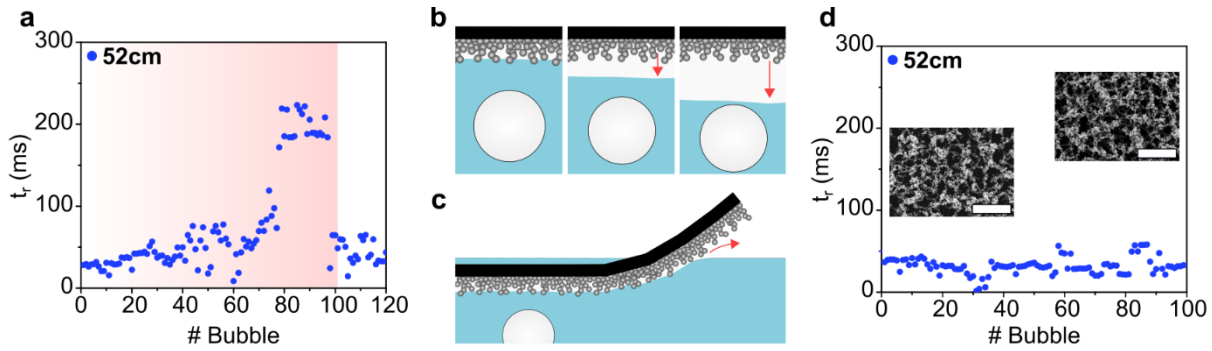

Figure 2.3. Long-term stability. a) Rupturing times of 120 consecutive bubbles on a LFS coating. To highlight the effect of air layer build-up, a surface coated for 10 min at a distance of 52 cm was used for exemplification. After 100 bubbles, the captured air was allowed to escape. b) Schematic illustration of a superamphiphobic particle surface fully submerged in a liquid. The air layer gradually builds up in thickness with addition of air from each consecutive bubble (not to scale). c) Schematic illustration of a bent surface where the air layer within the coating is connected to the environment. The air from captured bubbles is continuously released into the environment, thus preserving surface performance. d) Rupturing times of 100 consecutive bubbles on a bent LFS coating (52 cm, 10 min) connected to the ambient gaseous environment. SEM images before and after the experiment show no mechanical degradation (scale bars are 10 µm).

To resolve the influence of air layer build-up, a pathway for excess air to escape was introduced. We coated a glass slide with a 45° bend, as illustrated in Figure 2.3c. Figure 2.3d shows that t_r remained constant within experimental accuracy for all 100 captured bubbles (see Figure 2.15 for the performance of an optimized LFS coating). We observe no mechanical degradation of the LFS coating after the impact and absorption of 100 consecutive bubbles (insets in Figure 2.3d). This highlights the durability and utility of such surfaces for long-term bubble capture.

In most real-world systems, surface-active species such as surfactants are present. Dissolved in an aqueous environment, they spontaneously adsorb at hydrophobic interfaces. To investigate the behavior of bubbles contacting an optimized LFS surface in the presence of a surface active species, experiments were conducted using the nonionic surfactant pentaethylene glycol monododecyl ether (C12E5)[158].

When immersed in water (purple), bubbles ruptured immediately upon contact with the LFS (Figure 2.4a) and DNP (Figure 2.4b) surfaces. Upon addition of C12E5 (red) at half the critical micelle concentration (0.03 mM, surface tension 30.7 mN m^{-1} [159]), the time required for bubble rupturing on the LFS surface increased to 33 ± 21 ms. Bubbles did not bounce off the surface but rather rested on it until they spontaneously ruptured. Due to the presence of surfactant molecules at the liquid-gas and liquid-solid interfaces, the thin liquid film between the two phases is temporarily stabilized. The molecules increase the elasticity of the thin film and reduce the Laplace pressure while increasing pinning of the three phase contact line, causing the overall increase in bubble rupturing times.

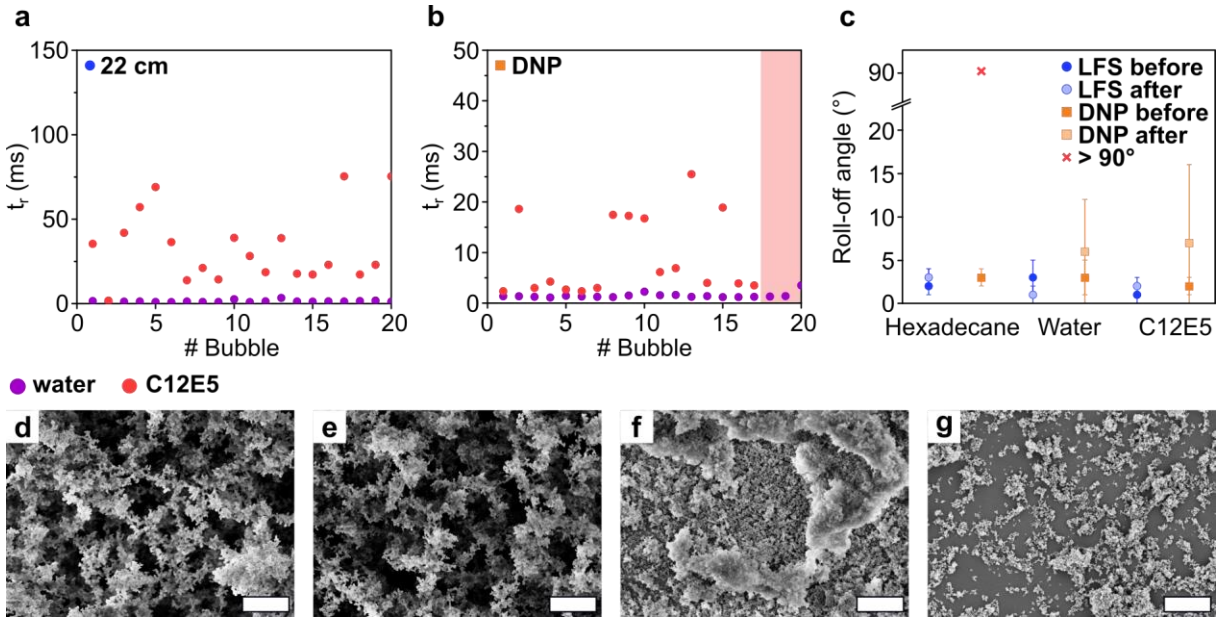

Figure 2.4. Surface-active species. Rupturing times of individual bubbles in 20 different spots on a) a LFS surface (22 cm, 10 min) and b) a DNP surface at equilibrium in water (purple) and C12E5 (red). After 17 bubbles, the DNP surface failed to induce bubble rupturing within 2 min. Bubbles remained pinned on the surface (red area). c) Roll-off angles using 6 µL of n-hexadecane, water, and C12E5 before and after conducting single-bubble rupture experiments in C12E5 on LFS (blue) and DNP (orange). SEM images of the LFS (d,e) and DNP (f,g) surface before (d,f) and after (e,g) conducting experiments in C12E5 (scale bars are 2 µm).

SEM images before (Figure 2.4d) and after (Figure 2.4e) the experiment in soap solution show no mechanical degradation of the LFS coating. The LFS surface maintains its superamphiphobic wetting properties (Figure 2.4c). However, for the DNP surface, we observed delamination and partial imbibition of the coating starting with the impact of the first bubble and during repeated release of captured air into the environment. While the DNP surface initially showed comparatively low rupturing times of 9 ± 8 ms, it eventually failed to induce bubble rupturing (Figure 2.4b, red area). After experiments in the C12E5 solution, only patchy particle aggregates remained on the substrate (Figure 2.4f and g). Interestingly, the

damaged surface was able to retain superhydrophobic properties (Figure 2.4c). Drops of water and C12E5 solution rolled off when the surface was tilted by only a few degrees. The poorer durability of the DNP surface can be attributed to its lack of having a binder or adhesion promoter. A binder increases adhesion of the coating to the substrate, thus counteracting delamination. The LFS surface is able to maintain its mechanical structure and superamphiphobic properties even after repeated bubble rupturing in the soap solution, demonstrating the superior performance of these surfaces.

The ability to rupture bubbles even in solutions of low interfacial tension offers the possibility to destabilize bubbles in froth flotation, a heterogeneous mixtures of a liquid, a gas and a solid phase. Flotation has long been used to selectively separate solid materials using stable froths from a slurry generated, for example, in industrial wastewater treatment[139,140] and mineral processing[141,142]. Froth flotation efficiency is gauged with respect to froth collection, production efficiency, and the purity of the "final concentrate".[160]

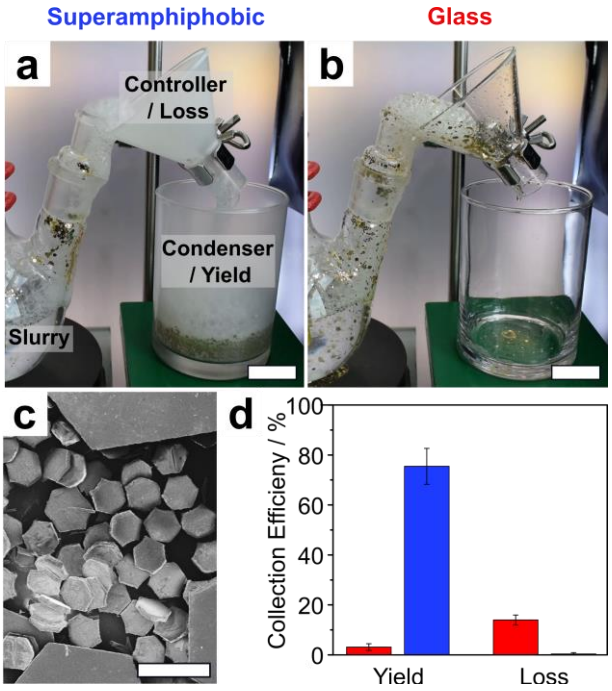

Figure 2.5. Separation of solid plates via froth flotation using a) a superamphiphobic and b) a pristine glass froth controller and condenser (scale bars are 5 cm). Froth produced from the slurry composed of C12E5 in water and hydrophobized hexagonal PET plates via a stirrer, is transported along the froth controller to the condenser. The setup was run for 2 minutes of a) continuous and b) pulsed flotation. c) The size distribution (tip-to-tip) of the solid component is 1:1:1 w/w/w of 2600 µm, 1200 µm, and 250 µm. d) The high material collection yield demonstrates the potential of superamphiphobic froth control systems. While the glass control suffers from clogging and losses at the outlet, the superamphiphobic system experiences minimal clogging and no losses.

Here, we demonstrate the separation efficiency of both, a superamphiphobic (Figure 2.5a) and an uncoated (Figure 2.5b) froth controller and condenser. The uncoated device serves as a control. The froth was generated *via* stirring from 400 mL of an aqueous slurry composed of C12E5 (1.0 mM) and 600 mg of hydrophobized PET plates[161] (Figure 2.5c) with an air inlet pressure of 0.5 bar. The setup was run for 2 minutes of continuous and pulsed flotation (Supplementary Video M3). The control runs had to be pulsed to prevent excessive spillage during froth / particle collection. In contrast, the superamphiphobic system demonstrated 1) continuous flotation due to efficient bubble rupturing by both the froth controller and condenser, 2) successful particle collection with high yields of 75 ± 7 %, and 3) minimal delivery channel (i.e. funnel) losses. The uncoated device exhibited low yields of only 3 ± 1 % with excessive particle clogging and losses within the delivery channel.

2.3 Conclusion

In conclusion, ultrafast bubble bursting by superamphiphobic surfaces requires control of the nano- and micrometer scale architecture of the hierarchical structures. Superhydrophobicity, superamphiphobicity, and even aerophilicity do not automatically guarantee efficient bubble rupturing capabilities. Liquid flame spray is a highly tunable technique, suitable for the design of hierarchical textures with optimized length scale, network geometry and particle diameters below 100 nm to induce so-termed ultrafast bubble bursting in less than 2 ms. The surfaces demonstrate long-term bubble rupturing properties without chemical or mechanical degradation in both pure water and surfactant solution. Therefore, liquid flame spray serves as a promising candidate for passive bubble capturing. We demonstrated the use of superamphiphobic coatings for froth control by enhancing the efficiency of a flotation setup. We envision the use of these optimal design principles for applications in industrial water treatment, foam control, and electrocatalytic gas-evolving reactions for clean energy production.

2.4 Methods

Liquid Flame Spray Coatings. A flame was created by oxygen (2 L min^{-1}) and methane (1 L min^{-1}). A liquid feedstock consisting of TEOS (98 %, Sigma Aldrich) dissolved in isopropanol (Fisher Scientific) was dispersed into the flame using oxygen (5 L min^{-1}) at a feed rate of 1 mL min^{-1}. The concentration of TEOS in isopropanol was 370 mg mL^{-1}. The distance between the burner unit and the glass substrate was varied from 22 cm to 52 cm, the maximum distance accessible. The coating time was varied from 3 min, to 5 min and 10 min. To enhance the mechanical stability of the particle coatings, a silica shell was added *via* CVD. The surfaces were placed in a desiccator together with TEOS (98 %, Sigma Aldrich, 2 mL in 2.400 cm^3) and aqueous ammonia solution (25 %, VWR Chemicals, 2 mL in 2.400 cm^3). The reaction was allowed to proceed for 16 h at atmospheric pressure. Thereafter, the coatings were sintered for 3 h at 500 °C in air. The surfaces were fluorinated using 100 µL 1*H*,1*H*,2*H*,2*H*-perfluorooctyl-trichlorosilane (PFOTS, 97 %, Alfa Aesar) in a desiccator (9.200 cm^3) at 50 mbar. After 2 h, the surfaces were removed and placed into a vacuum oven at 60 °C for 2 h to remove unreacted silane.

Dense Nanoparticle Coatings. The particle spray coating was synthesized according to the procedure described by Wong[57] The synthesis was conducted under argon atmosphere. Under gentle stirring, 1 g of fumed silica nanoparticles (Aldrich, 7 nm, SSA = 395 m^2/g) and 0.9 mL of 1*H*,1*H*,2*H*,2*H*-perfluorodecyl-trichlorosilane were added to 30 mL of dried chloroform (> 99.8 %, Fisher Scientific). The reaction was allowed to proceed at 25 °C and a stirring rate of 500 rpm for 96 h. Afterward, the particles were washed with chloroform and dried at 50 °C for 24 h. For spray coating, the particles were re-dispersed in acetone at a concentration of 10 mg mL^{-1}. 10 mL of the suspension were used to coat an area of 76 x 26 mm. The suspension was sprayed onto microscope glass slide with a flow rate of 0.2 mL s^{-1} at 3 bars and a working distance of 10 cm using a spray gun (nozzle diameter of 0.2 mm). The surfaces were allowed to dry for 24 h.

Silicone Nanofilaments. A mixture of TCMS (400 µL, 99 %, Sigma Aldrich) and toluene (100 mL, Sigma Aldrich) with a water content between 150 and 170 ppm was stirred for 60 s. The water content was evaluated using a coulometer (Mettler Toldeo C20 Compact KF coulometer). Microscope glass slides (Thermo Scientific) were immersed into the solution and the reaction vessel was tightly sealed. After 3 h, the surfaces were briefly washed with hexane (95 %, Fisher Scientific) and dried under a nitrogen flow. The nanofilaments were activated with oxygen plasma (Diener Electronic Femto, 6 cm^3 min^{-1} oxygen flow rate) for 2 min at 120 W. Thereafter, the surfaces were placed in a desiccator (9.200 cm^3) together

with 100 µL PFOTS (97 %, Alfa Aesar). The pressure was reduced to 50 mbar and the reaction was allowed to proceed for 2 h at room temperature. Afterward, the surfaces were placed in a vacuum oven for 2 h at 60 °C.

Characterization. The roll-off angles were measured using water, *n*-hexadecane, and C12E5 (0.03 mM, CMC: 0.07 mM at 25 °C [159]). The surface tensions are 72.8 mN m^{-1}, 27.5 mN m^{-1}, and 30.7 mN m^{-1} [159], respectively. Roll-off angles were measured by carefully placing a 6 µL droplet onto the surface and subsequently tilting the surface at a rate of 1 degree per second until the droplet slides completely out of the field of view. A minimum of 5 spots were analyzed for each surface. Scanning electron microscopy images were acquired at a voltage of 3 kV (InLens Detector, LEO 1530 Gemini, Zeiss). To reduce charging effects and enhance the image quality, surfaces were coated with a 9 nm Pt layer (BalTec MED 020 Modular High Vacuum Coating System, Argon at 2×10^{-2} mbar and 30 mA). For the particle size distributions, a minimum of 100 particles per surface were evaluated using ImageJ. Dynamics of single bubble rupturing were recorded using a high-speed camera (Fastcam AX10, Photron) and a high magnification objective (2x, Mitutoyo) at a frame rate of 20,000 frames per second. Bubble mobility was analyzed using image processing algorithms in MATLAB (edge detection). This enabled tracking of bubbles and their respective center-of-mass. The velocity of the center-of-mass is computed and used to determine key events: 1) Initial decrease to minimum represents surface approach, 2) Sharp increase to maximum represents rupture, and 3) Final decrease from maximum triggers the end of the analysis.

2.5 Supporting Information

2.5.1 Supplementary Discussions

Liquid Flame Spray. Liquid flame spray (LFS) is a promising technology for the rapid one-step synthesis of nanoparticles. Single- and multicomponent materials have been produced from a plethora of elements.[162] LFS allows the fabrication of nanoparticle films with well controlled surface morphologies and high reproducibility. Due to the high surface-to-volume ratio, nanoparticle-based materials find various application for example as gas-sensors[163], biomedical sensors[164,165], and in batteries[166].
In the present LFS setup, the precursor dissolved in a carrier fuel is dispersed using oxygen as a dispersion gas and ignited by the surrounding methane/oxygen process gas flame. The fine precursor droplets are evaporated and the gaseous precursor is combusted and decomposed by several parallel and consecutive reactions. At supersaturation of the gaseous product, particle nucleation takes place. During transport by

gas flow within the flame, the particles experience surface growth, aggregation, and sintering. At lower temperatures further away from the burner, sintering is suppressed and particles form weakly bonded agglomerates.[60,71] Nanoparticles and agglomerates thereof can be directly deposited on a substrate. The residence time of particles in the hot zone of the flame controls the size and structure of the collected product.[70] Therefore, parameters including the collection distance from the burner, the precursor feed rate and concentration, and the dispersion gas feed rate directly influence the morphology of the resulting film.[72,163] Careful engineering of the appropriate nanoparticle surface, bulk composition and the nanoparticle architecture is required.

The deposition mechanism of aerosol-based nanoparticles into three-dimensional microstructures has been described by the Peclet number, i.e. the scaled ratio between the displacement by an orthogonal/advective velocity and the stochastically distributed diffusive velocity caused by Brownian motion.[66,163] In general, there are three different self-assembly regimes. In the ballistic regime, the advective flow dominates and the initial trajectory of the particles is mostly preserved. The directed self-assembly of nanoparticles results in the formation of relatively dense structures. At low Peclet numbers, undirected Brownian motion dominates. In this diffusive regime, highly porous structures are formed. The third regime describes a combination of the two mechanisms, leading to a range of porosities and surface morphologies.

The resulting macro-morphology depends on the primary particle size and the number of particles in an agglomerate.[66,163,167] Mathematical models[66,163] and experimental studies[163] consistently show that a larger primary particle size and a higher number of particles in an agglomerate lead to the formation of a more porous structure. The degree of particle agglomeration is dependent on the particle concentration and collision events.[71]

Thin Film Interactions. In the present system, an air bubble driven by buoyancy is rising against a surface, causing the aqueous film between the air bubble and the surface to thin. The deformation of the air bubble due to the proximity of the surface is described by an augmented Young-Laplace equation.[150] The disjoining pressure Π is the sum of van der Waals, steric, and electrical double layer forces. For air bubbles in pure water, the contributions from the electrical double layer are small and there is no steric hindrance. Therefore, the disjoining pressure is dominated by van der Waals interactions. They sensitively depend on the thickness of the thin film.

The hydrodynamic drainage of the thin aqueous film confined between the bubble and the surface protrusions is a key physical process controlling the impact of the bubble and can be approximated by the Stokes-Reynolds equation.[150,168] This governing equation is based on 2 primary assumptions: 1) low

Reynolds number[169,170], and 2) no-slip boundary condition (often occurs due to rapid environmental contamination).[157] After the film thinned to a thickness of a few ten nanometers, we expect that the highest protrusion causes rupture. It is still under debate whether rupturing is induced by thermal fluctuations or by hydrophobic interactions and how this depends the viscosity and composition of the surrounding phase.[171,172]

2.5.2 Supplementary Figures

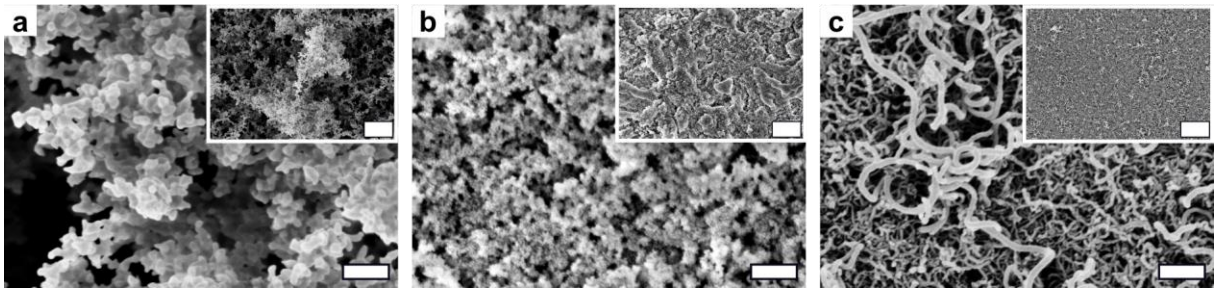

Figure 2.6. SEM images of typical model surfaces at two different magnifications: a) hierarchical particle coating prepared by liquid flame spray, b) dense nanoparticle coating prepared via wet-spray coating and c) silicone nanofilaments (main scale bars and scale bars in insets are 500 nm and 5 µm, respectively).

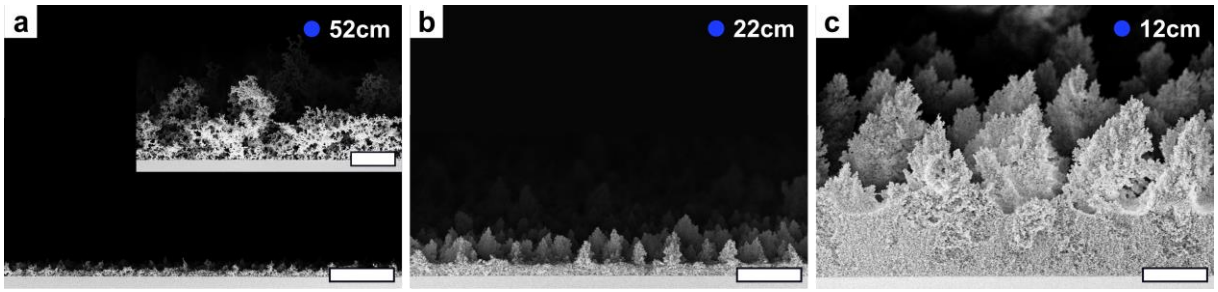

Figure 2.7. SEM images of LFS surfaces coated at a) 52 cm, b) 22 cm, and c) 12 cm distances to the burner for 10 min (main scale bars are 100 µm, scale bar in the inset is 10 µm). With decreasing coating distance / increasing coating thickness, the cone-shaped surface structures are more pronounced.

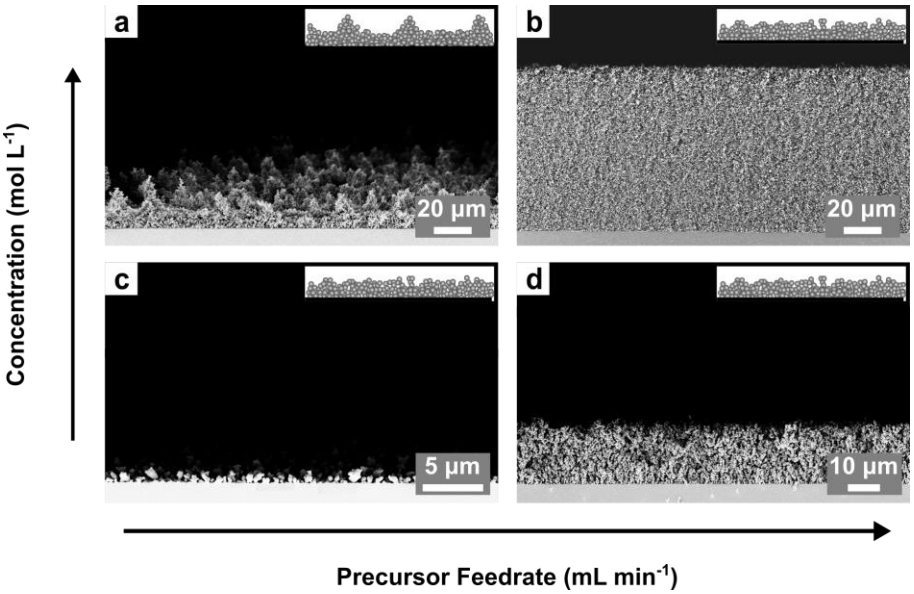

Figure 2.8. The surface morphology of in situ deposited liquid flame spray films depends on the precursor feed rate and the precursor concentration. All samples were coated at a distance of 22 cm to the burner with the following parameters: a) 5 min, 1 mL min^{-1}, 1.8 mol L^{-1}, b) 5 min, 5 mL min^{-1}, 1.8 mol L^{-1}, c) 10 min, 1 mL min^{-1}, 0.18 mol L^{-1}, and d) 10 min, 1 mL min^{-1}, 0.18 mol L^{-1}. The SEM micrographs reveal, that a high precursor concentration in combination with a low feed rate results in the formation of conically structured surfaces.

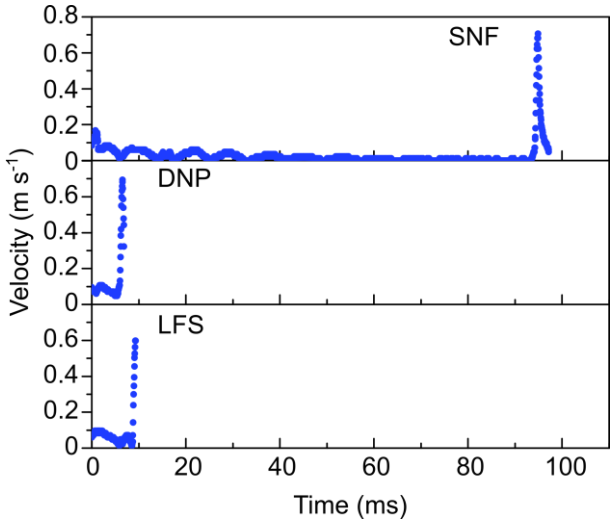

Figure 2.9. Bubble rupturing on different types of surfaces: the air absorption rate (slope of the sharp increase in velocity) is independent of the rupturing time and the surface morphology.

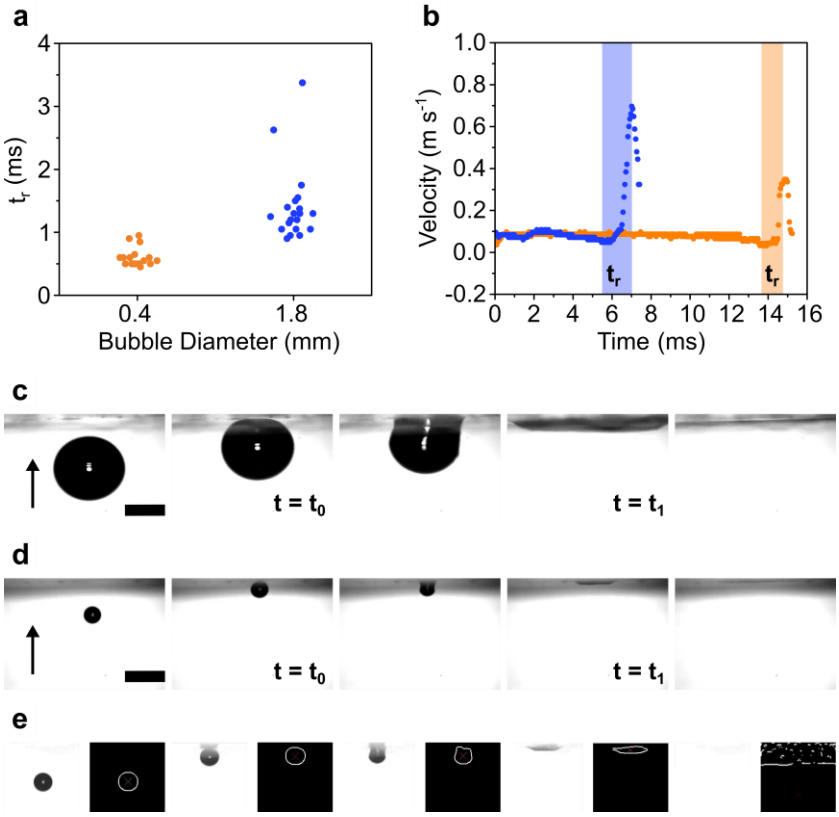

Figure 2.10. a) Rupturing times of single bubbles with a diameter of 0.4 mm (orange) and 1.8 mm (blue) on pristine LFS surfaces coated at a distance of 22 cm for 10 min. b) Bubble velocity as a function of time. The bubble diameters are 0.4 mm (orange) and 1.8 mm (blue). The difference in the rate of air absorption is attributed to the respective bubble / air volume. This also causes the extremely short rupturing times observed for bubbles with a volume of 0.034 µL (0.4 mm) compared to 3.0 µL (1.8 mm). c,d) Images acquired by a high speed camera (scale bars are 1 mm) of a bubble with a diameter of c) 1.8 mm and d) 0.4 mm rupturing immediately upon contacting a pristine LFS surface. e) Analysis of bubble mobility using MATLAB. After background subtraction, the bubble's center of mass was tracked and the velocity was computed.

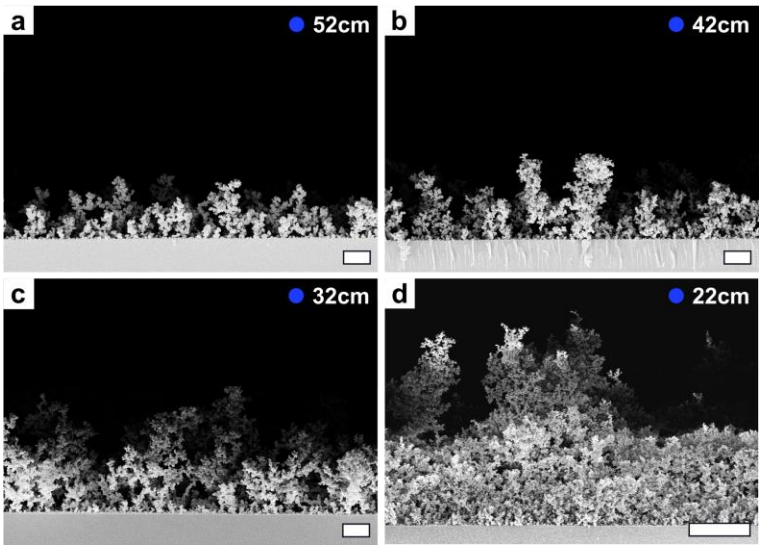

Figure 2.11. Morphology of LFS coatings. Side-view SEM images of a-d) LFS surfaces coated at different distances to the burner for 5 min (scale bars are a,b) 2 µm and c,d) 10 µm). Decreasing the coating distance from 52 cm to 22 cm leads to an increase in coating thickness from approximately 5 µm to 35 µm.

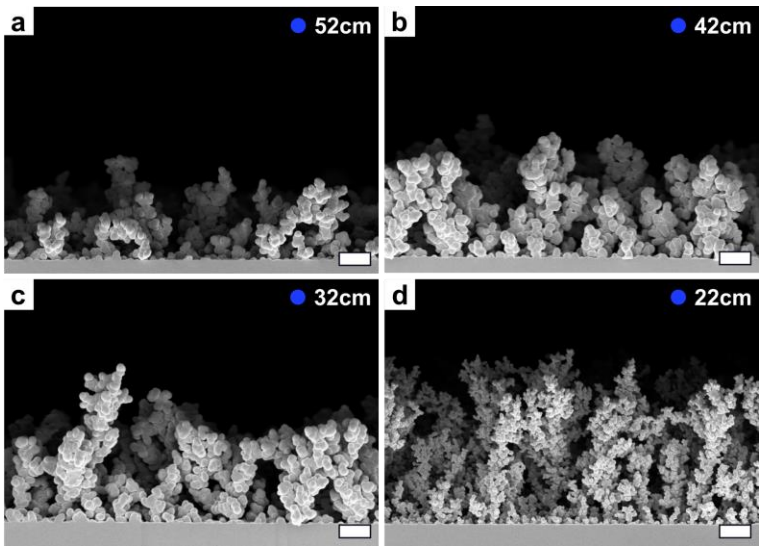

Figure 2.12. Morphology of LFS coatings. Side-view SEM images of a-d) LFS surfaces coated at different distances to the burner for 3 min (scale bars are 1 µm). Decreasing the coating distance from 52 cm to 22 cm leads to an increase in coating thickness from approximately 3 µm to 6 µm.

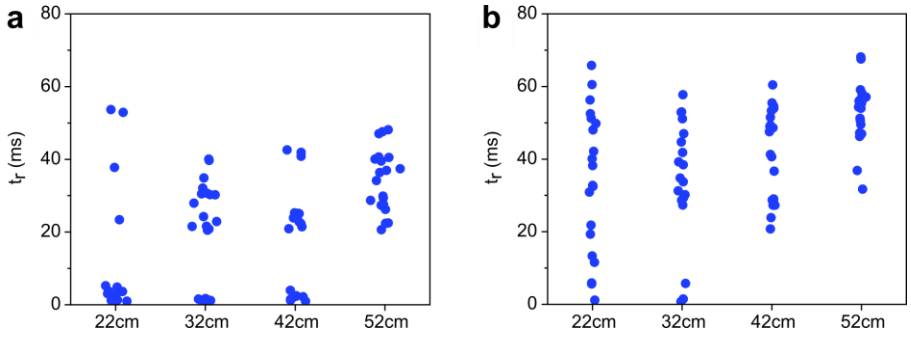

Figure 2.13. Rupturing time of air bubbles rising in water against 20 different spots on pristinely synthesized surfaces. After each bubble, the captured air was released to the environment. LFS surfaces coated at increasing distances to the burner for a) 5 min and b) 3 min. Independent of the coating time, the probability of bubbles rupturing immediately upon contact decreases with increasing coating distance. For example, 70 % of bubbles contacting a surface coated at 22 cm distance for 5 min rupture immediately with rupturing times of less than 10 ms. In case of a surface coated at 52 cm distance for 5 min, bubbles always rebound.

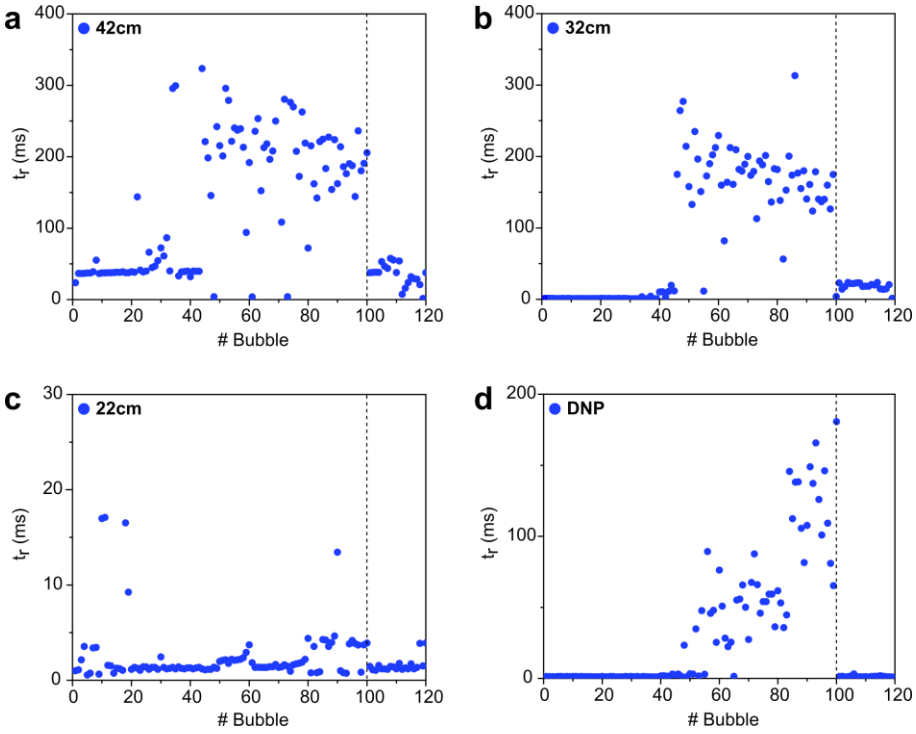

Figure 2.14. Rupturing times of 120 consecutive bubbles on a-c) LFS coatings and d) a DNP coating. The LFS surfaces were coated for 10 min at a) 42 cm, b) 32 cm, and c) 22 cm distance to the burner. After 100 bubbles (see dashed line) the accumulated air from the captured bubbles was released to the environment. Afterward, the coatings were able to recover their rupturing times, demonstrating their durability.

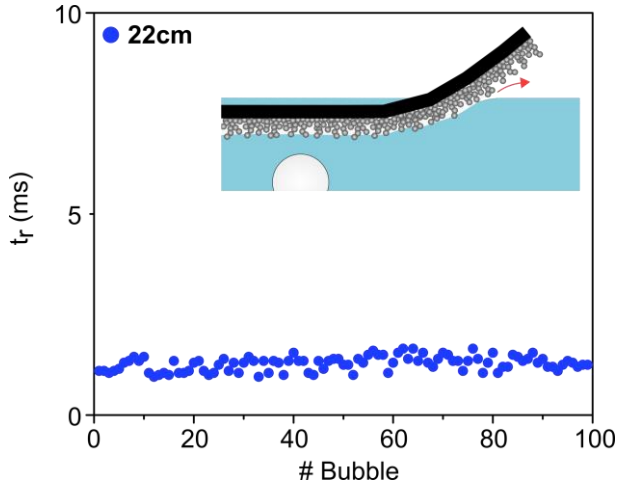

Figure 2.15. Rupturing times of 100 consecutive bubbles on a bent LFS coating (22 cm, 10 min) connected to the ambient gaseous environment. Introducing a pathway for excess air to escape allows constant ultrafast bubble bursting with rupturing times of less than 2 ms for all 100 captured bubbles within experimental accuracy. This highlights the durability and utility of such surfaces for long-term bubble capture.

2.6 Author Contributions

K.I.H fabricated the surfaces, carried out the experiments and characterization, unless stated otherwise below, and wrote the manuscript. W.S.Y.W. wrote the image processing algorithms used to analyze bubble motion. K.I.H., W.S.Y.W, and D.V. contributed to experimental planning, data analysis, and manuscript preparation. All authors reviewed and approved the manuscript.

2.7 Acknowledgments

The authors thank H.- J. Butt, L. Hauer, A. Naga, and A. Sharifi for stimulating discussions and technical support. This work was supported by the Max Planck Graduate Center (K.I.H.), the European Union's Horizon 2020 research and innovation program LubISS No. 722497 (W.S.Y.W., D.V.) and the ERC Advanced Grant No. 340391 "SUPRO" and the priority program SPP 2171 (D.V.).

3 Fluorine-Free Super-Liquid-Repellent Surfaces: Pushing the Limits of PDMS

Katharina I. Hegner, [redacted], [redacted], [redacted]

Physics at Interfaces, Max Planck Institute for Polymer Research, Ackermannweg 10, 55128 Mainz, Germany

E-mail: [redacted]

Keywords: Friction, Nanoparticles, Superhydrophobic, Surface chemistry, Wetting

This manuscript is submitted for publication, 2022.

Abstract

Until now, methods for fabricating super-liquid-repellent surfaces have typically relied on perfluoroalkyl substances. However, growing concerns about the environmental and health effects of perfluorinated compounds have caused increased interest in fluorine-free alternatives. Polydimethylsiloxane (PDMS) is most promising because it is non-toxic, environmentally friendly, and has low surface energy. Here, we demonstrate that a well-designed two-tier structure combined with a fluorine-free, low surface energy PDMS functionalization allows super-liquid-repellency toward low surface tension liquids. The surfaces consist of silicon dioxide nanoparticles functionalized with surface-tethered PDMS chains. Drops of water-ethanol solutions with surface tensions as low as 31.0 $mN\ m^{-1}$ easily roll and bounce off the surface. Friction force measurements demonstrate excellent surface homogeneity and easy mobility of drops. Our work shows that fluorine-free super-liquid-repellent surfaces can be achieved using scalable fabrication methods and an environmentally friendly surface functionalization.

3.1 Introduction

Inspired by structures found on various plants[51] and insects[52,173][22,85], artificial super-liquid-repellent surfaces have been developed for applications including self-cleaning[174], heat transfer[175], anti-icing[176], or anti-biofouling[124,125]. On super-liquid-repellent surfaces, drops exhibit apparent contact angles exceeding 150° and roll off when the surface is tilted by less than 10°.[4,177] In order to achieve this, appropriate surface structures combined with low surface energy are required.[18,19] Perfluoroalkyl substances are conventionally used to achieve super-liquid-repellency toward low surface tension liquids[178,179], yet there are growing concerns toward this class of chemicals. They are persistent and may bio-accumulate in humans, animals, and plants,[80–82] thereby posing a danger to human health such as thyroid disease, liver damage and effects on reproduction and fertility.[80]

Therefore, fluorine-free alternatives are urgently needed. Various strategies have been tested to design fluorine-free surfaces, where droplets of water and low surface tension liquids easily roll off. Silicones, waxes, alkanes, or carbon materials are considered promising although it is still unclear, how to achieve super-liquid-repellency even toward low surface tension liquids using scalable methods.[180] There are multiple benefits to silicones; they are non-toxic, biocompatible, colorless, and cheap. Most importantly, they have a low surface energy of approximately 20 mN m^{-1}.[89] The most common silicone is trimethylsiloxyl-terminated linear poly(dimethylsiloxane) (PDMS). On flat surfaces, hydrophobicity and even repellency toward oils and organic liquids have been achieved.[50,91,92,95] Although these surfaces often exhibit very low roll-off angles, the velocity of drop mobility is typically a few orders of magnitude below those on superhydrophobic surfaces. Superhydrophobic PDMS surfaces have been prepared successfully by coating of preformed structures[98,180] or through one-step processes such as the formation of fibrous silicone nanofilaments[153]. Water has a high surface tension of 72 mN m^{-1}, thus superhydrophobicity is relatively easy to achieve. The lower the surface tension of the liquid, the more difficult it becomes to engineer a suitable surface. Recently, a silica particle-based coating has been shown to also repel ethylene glycol (γ_{EG} = 47.7 mN m^{-1}).[181] To the best of our knowledge, so far only silicon-based double reentrant structures allowed fluorine-free super-liquid-repellency toward even lower surface tension liquids.[83] These intricate surface structures suffer from a costly multistep fabrication procedure.

In this work, we present surfaces that are able to repel liquids with surface tensions as low as 31.0 mN m^{-1}. Contact angles above 150°, low roll-off angles below 10°, and rebound of impacting drops ensure high drop mobility. The surfaces consist of silicon dioxide nanoparticles that are functionalized

with surface-tethered PDMS chains. We demonstrate that a well-designed roughness on the nano- and micrometer scale is essential to achieve super-liquid-repellency. Equally important is that the structures can be produced via fabrication methods that are applicable to virtually any substrate and over large areas.

3.2 Results and Discussion

To investigate the significance of surface topography and overhang morphologies on the nano- and microscale on fluorine-free super-liquid-repellency, we prepared a range of silicon dioxide particle-based surfaces. The three fabrication methods, namely liquid flame spray, spray coating, and the deposition of soot from a paraffin candle can be scaled up (Figure 3.1a-d, Figure 3.5, and Figure 3.6).

In liquid flame spray (LFS), a liquid feed containing the precursor (tetraethoxysilane in isopropanol) was injected into a CH_4/O_2 flame where the feed evaporates, and the precursor combusts. Silica particles nucleate and grow. The time and process distance at which nanoparticles are collected determine their diameter, degree of aggregation, and the coating's microscale roughness.[182] A thin silica shell of approximately 10 nm was added by chemical vapor deposition to enhance the mechanical stability of the coatings. For the sample LFS I, coated for 3 min at 15 cm distance from the burner, nanoparticles with diameters of 83 ± 19 nm aggregate into structures with heights between approximately 8 and 10 µm (Figure 3.1a, Inset red lines). The sample LFS II was coated for 2 min at a distance of 10 cm and displays porous protrusions that vary in height by up to 5 µm. Neighboring surface protrusions are spaced out by approximately 10 to 20 µm. The lower process distance causes reduced growth times resulting in smaller nanoparticle diameters of 47 ± 8 nm (Figure 3.1b).

The second type of sample was prepared by spray coating fumed silica particles with a diameter of 7 nm. The particles were dispersed in acetone (5 mg mL^{-1}) and sprayed onto the substrates at a flow rate of 0.2 mL s^{-1} at 2 bar and 10 cm distance. During spray coating and drying, the particles form aggregates with a diameter of 32 ± 5 nm. These aggregates assemble into porous features with heights varying by up to 20 µm and distances of up to several tens of micrometers (Figure 3.1c). The sprayed silica particle (SSP) surface exhibits the highest degree of micrometer scale roughness. Candle soot coatings (CSC) were formed from the combustion of paraffin wax in a flame.[61] The soot deposit is coated with a silica shell to introduce the surface hydroxyl groups necessary for surface functionalization. The resulting nanoparticles have a diameter of 85 ± 18 nm. The surfaces are homogeneous on the microscale; the height varies by less than 1 µm (Figure 3.1d).

If not stated otherwise, the surfaces are functionalized with linear PDMS chains via solvent-free chemical vapor deposition of dichlorotetramethyldisiloxane at ambient environment (Supporting Information, Experimental Section). [92,183] The chlorosilane dimer is hydrolyzed by water from the environment and reacts with hydroxyl-groups via condensation reactions (Figure 3.1e). This reaction can occur between several species including the surface hydroxyl groups, the hydrolyzed dimers, surface grafted PDMS chains, and loose oligomers. On flat surfaces, a two-dimensional PDMS coating with a thickness of a few nanometers is formed.[50,91,95]

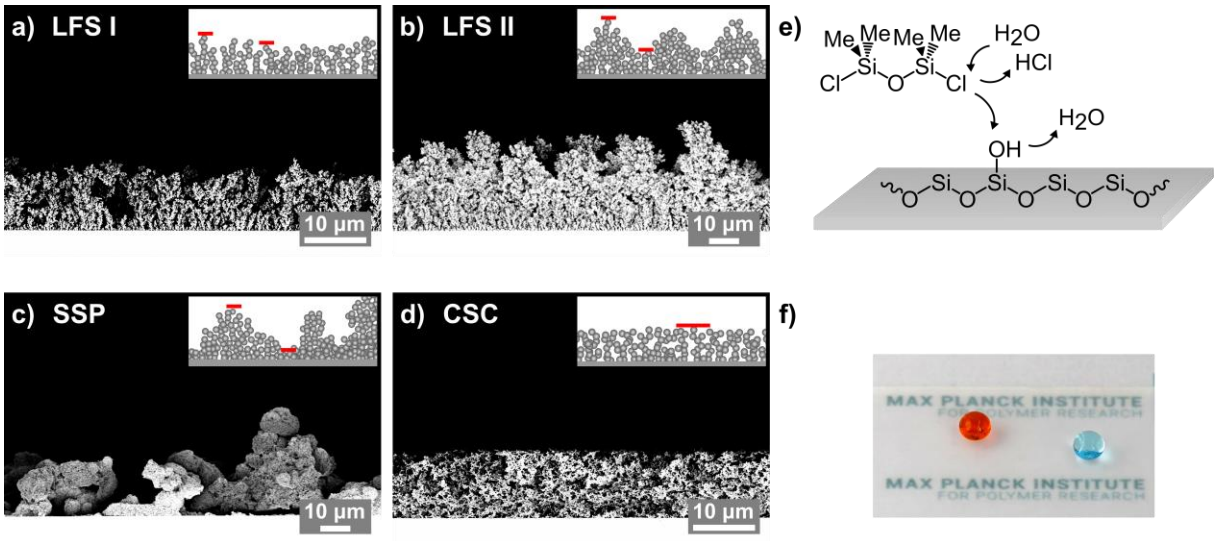

Figure 3.1. Scanning electron microscopy images of various particle-based surfaces: a) liquid flame spray I (LFS I), b) liquid flame spray II (LFS II), c) sprayed silica particles (SSP), and d) a candle soot coating (CSC). The insets show schematic illustrations of the particle structures with the red lines indicating the structural differences in height. e) Functionalization with dichlorotetramethyldisiloxane results in the formation of surface-tethered linear PDMS chains which render the surfaces super-liquid-repellent. f) Optical images of dyed 15 µL drops of water (blue) and ethylene glycol (orange) on a PDMS-functionalized SSP surface.

To quantify the super-liquid-repellency we used water-ethanol solutions. Increasing the fraction of ethanol allowed us to gradually reduce the surface tension (Supporting Information, Table T2). For all samples, the contact angles of 6 µL drops of milli-Q water exceed 165° (Figure 3.2a). Notably, both liquid flame spray surfaces, LFS I-PDMS (green) and LFS II-PDMS (orange) even exhibit contact angles of more than 150° for water-ethanol solutions with a surface tension of 31.0 and 32.8 mN m^{-1}, respectively. Impacting drops bounce off (Supporting Information Movie M4). We observed roll-off angles of less than 10° for all test liquids (Figure 3.2b, Supporting Information Movie M1). The high contact and low roll-off angles are in line with a stable Cassie state, where the liquids rest on a composite solid-air interface.[16,184] On the sprayed silica particle surface (blue), contact angles abruptly dropped to

less than 100° for surface tensions lower than 34.8 mN m^{-1}. While the candle soot coating (red) could repel liquids with surface tensions down to 32.8 mN m^{-1}, the contact angles were continuously lower than the values observed using the LFS surfaces.

For diiodomethane (γ_{DI} = 50.9 mN m^{-1}) roll-off angles between 3° and 6° and contact angles well above 150° were observed for all samples (Figure 3.2c). Drops of ethylene glycol (γ_{EG} = 47.7 mN m^{-1}) rolled off both LFS surfaces (green, orange) at a 2° to 3° tilt. Overall, superior super-liquid-repellency was observed for the LFS I-PDMS surface, which is able to repel water-ethanol solutions with a surface tension of only 31.0 mN m^{-1}. This suggests that a porous two-tier structure with protrusions varying by a few micrometers in height is most appropriate. Liquids with even lower surface tensions such as hexadecane (γ_{HD} = 27.6 mN m^{-1}) wet the surface.

In order to resolve pinning of the three-phase contact line and detect spatial heterogeneities even on the micrometer scale, we directly measured the friction force a drop experiences during motion.[5,6,45,48,185] The friction force is determined from the deflection of a flexible glass capillary while the substrate velocity was kept constant at v = 0.5 mm s^{-1}: $F_F = k_s \cdot \Delta x$ (Figure 3.2d). Here, Δx is the deflection and k_s the spring constant of the capillary (Supporting Information, Characterization). Drop friction depends on the solid-liquid interfacial area and therefore, on the drop volume. Hence, we normalized the force to the drop radius (r = 1.5 mm from V = 15 mm^3).

Using water, the friction forces measured on the LFS I-PDMS surface were as low as 1.8 ± 0.4 µN mm^{-1}, varying by 20 % across the investigated distance (Figure 3.2e, Supporting Information Movie M2). For LFS II-PDMS, the average force increased by 17 % to 2.1 ± 0.3 µN mm^{-1}. This is in line with a slight deterioration of the wetting properties compared to the LFS I-PDMS sample (Figure 3.2a). On the SSP-PDMS surface, a stick-slip motion was observed resulting in variations of the friction force of up to ± 30 %. The pronounced topographic roughness results in localized pinning sites. On the candle soot-based surface the force measurements reveal noticeable surface inhomogeneities on the millimeter scale, caused by the less-controlled sooting process. Depending on the surface, the friction forces agree within 60 to 115 % with friction forces calculated from the integration of the horizontal component of the liquid-air surface tension γ along the three-phase contact line[6] (Supporting Information, Table 1).

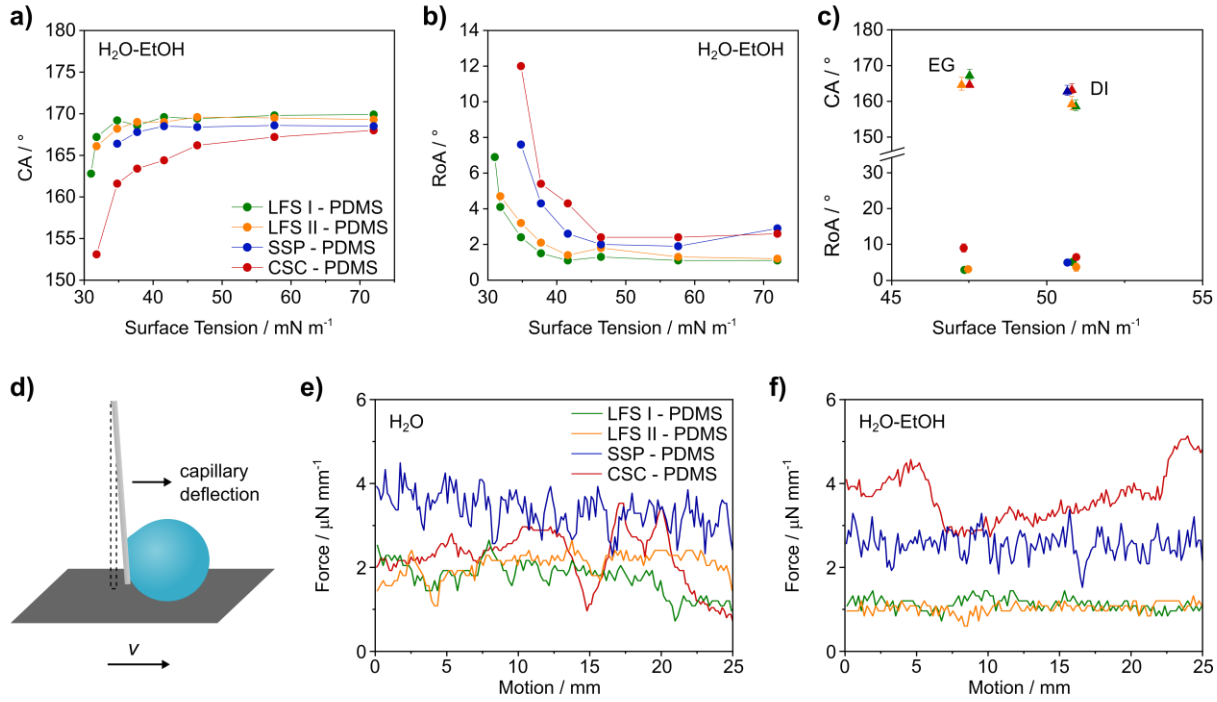

Figure 3.2. Wetting properties of structured PDMS-functionalized surfaces prepared by liquid flame spray (LFS), sprayed silica particles (SSP), and candle soot coatings (CSC). a) Contact angle and b) roll-off angle measurements using 6 µL drops of water and water-ethanol solutions. The amount of ethanol was increased from 0 to 35 wt% in steps of 5 wt%. Surface tensions were measured using the pendant drop method. c) Contact (▲) and roll-off (●) angle measurements using 6 µL drops of ethylene glycol (EG) and diiodomethane (DI). Drop friction measurements: d) A thin glass capillary is brought into contact with the drop (V = 15 µL). The surface is then moved laterally at a constant velocity (v) of 0.5 mm s^{-1}. Deflection of the glass capillary is measured using an optical microscope camera. Drop friction measurements using e) water and f) a 20 wt% water-ethanol solution.

Using a water-ethanol solution (γ = 37.7 mN m^{-1}), the normalized friction force decreases on both LFS by approximately a factor of two, i.e. proportional to the decrease of the interfacial tension (Figure 3.2f, Supporting Information Movie M3). The homogeneity of the surfaces is reflected in the smooth shape of the force curves. The candle soot-based surface exhibits the highest drop friction with 3.7 ± 0.59 µN mm^{-1}. The larger friction of the water-ethanol mixture on the candle soot coating hints that the lower contact angle (Figure 3.2a) and likely larger contact width cause the increase of the normalized friction force (Supporting information).

Both, the apparent contact angle and the friction force measurements show that the LFS I surface, followed closely by the LFS II surface, exhibits the most suitable surface morphology for super-liquid-repellency. A homogeneous microscale topography increases the solid-liquid interface, thereby reducing the super-liquid repellency (CSC, Figure 3.1d). On the other hand, a pronounced microscale roughness induces pinning sites which increase drop friction and roll-off angles (SSP, Figure 3.1c)

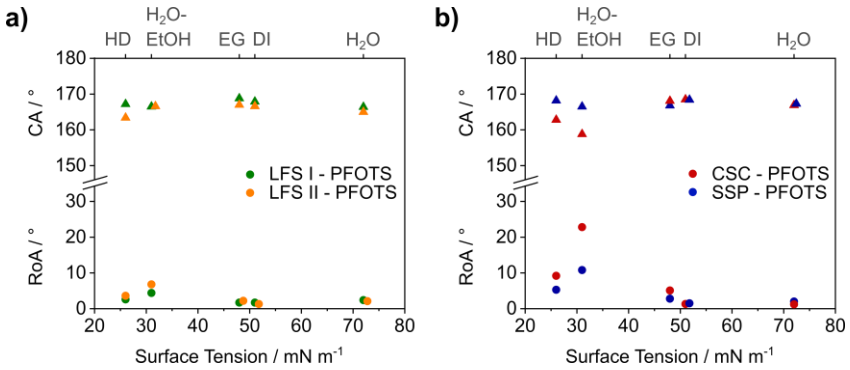

Figure 3.3. Contact angle (▲) and roll-off angle (●) measurements on structured PFOTS-functionalized surfaces prepared by a) liquid flame spray (LFS) and b) sprayed silica particles (SSP) and candle soot coating (CSC). The wetting properties were measured using water (γ_{H2O} = 72.0 mN m^{-1}), diiodomethane (γ_{DI} = 50.9 mN m^{-1}), ethylene glycol (γ_{EG} = 47.7 mN m^{-1}), a 35 wt% aqueous ethanol solution ($\gamma_{H2O\text{-}EtOH}$ = 31.0 mN m^{-1}), and hexadecane (γ_{HD} = 27.6 mN m^{-1}).

Nevertheless, structured fluorinated surfaces are the current benchmark for super-liquid-repellency. Therefore, we functionalized the four particle-based structures with perfluorooctyltrichlorosilane (PFOTS) via chemical vapor deposition (Figure 3.3a,b and Supporting Information, Table 3). Again, we observe the lowest roll-off angles using the LFS surfaces. For hexadecane, both surfaces exhibit roll-off angles of only 3° to 4°. The highest roll-off angles are observed for the candle soot-based surface, supporting that the inferior super-liquid-repellency is indeed due to the underlying particle structures.

3.3 Conclusion

Fluorine-free super-liquid-repellency can be achieved using PDMS. Here, the underlying surface topography is critical. Surfaces prepared via liquid flame spray show a suitable combination of dual-scale topography with overhang structures. With concerns about the bioaccumulation and toxicity of perfluoroalkyl substances on the rise, these results point a way toward fluorine-free alternatives based on suitable surface morphologies and a PDMS functionalization.

3.4 Methods

Sample Preparation. Silicon dioxide particle-based coatings were prepared via liquid flame spray (LFS), spray coating (SSP), and candle soot (CSC), Figure 3.5.

For liquid flame spray, a pilot flame was created by the process gases oxygen (2 L min^{-1}) and methane (1 L min^{-1}). A liquid feedstock consisting of tetraethyl orthosilicate (98 %, Sigma Aldrich) in isopropanol (Fisher Scientific) was dispersed into the flame. As a dispersion gas, oxygen was used at a flow rate of 5 L min^{-1}. The concentration of the precursor in isopropanol was 370 mg mL^{-1}. The particles were collected on glass substrates (Thermo Scientific) at a distance of 10 cm and 15 cm with respect to the burner unit for 2 min and 3 min, respectively. A silica shell was added via chemical vapor deposition to enhance the mechanical stability of the coatings. The surfaces were placed in a desiccator together with tetraethyl orthosilicate (98 %, Sigma Aldrich, 1 mL in 2.400 cm^3) and aqueous ammonia solution (25 %, VWR Chemicals, 1 mL in 2.400 cm^3). The reaction was allowed to proceed for 16 h at atmospheric pressure. Afterward, the coatings were sintered for 3 h at 500 °C in air.

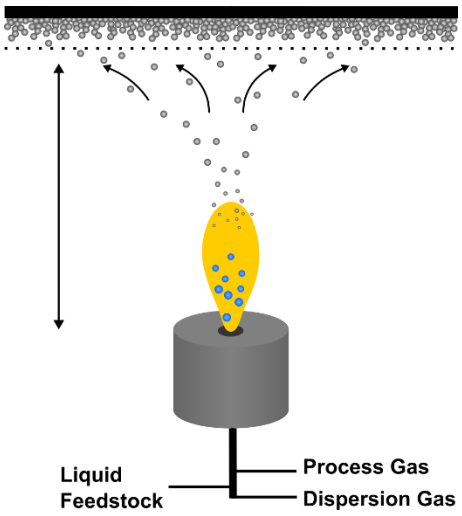

Figure 3.4. Schematic illustration of the LFS setup.

For the samples prepared via spray coating, fumed silicon dioxide nanoparticles (Aldrich, 7 nm, SSA = 395 m^2 g^{-1}) were dispersed in acetone at a concentration of 5 mg mL^{-1}. 5 mL of the dispersion were used to coat a microscope glass slide (Thermo Scientific) with an area of 76 x 26 mm. Samples were sprayed with a flow rate of 0.2 mL s^{-1} at 2 bar at a distance of 10 cm using a spray gun with a nozzle diameter of 0.5 mm. Afterward, the samples were allowed to dry for 24 h.

The candle soot-based particle surfaces were prepared according to a procedure described by Deng et al.[61]

Prior to surface functionalization, the samples were activated with oxygen plasma (Diener Electronic Femto, 6 cm^3 min^{-1} oxygen flow rate) for 10 min at 300 W. For the PDMS functionalization, the surfaces were placed in a desiccator (2.150 cm^3) together with 50 µL of 1,3-dichlorotetramethyldisiloxane (96 %, Alfa Aesar). The reaction was allowed to at ambient temperature (21 °C) and ambient humidity (40 – 60 %) for 1.5 h. Thereafter, the samples were placed in a vacuum oven (200 mbar) for 2 h at 60 °C, to remove non-covalently bonded oligomers. For fluorine functionalization, the plasma-activated

surfaces were placed into a desiccator (9.200 cm^3) together with 100 µL of 1*H*,1*H*,2*H*,2*H*-perfluorooctyltrichlorosilane (PFOTS, 97 %, Alfa Aesar). The pressure was reduced to 50 mbar and the pump was turned off. After 2 h, the surfaces were removed and placed into a vacuum oven (200 mbar) for 2 h at 60 °C.

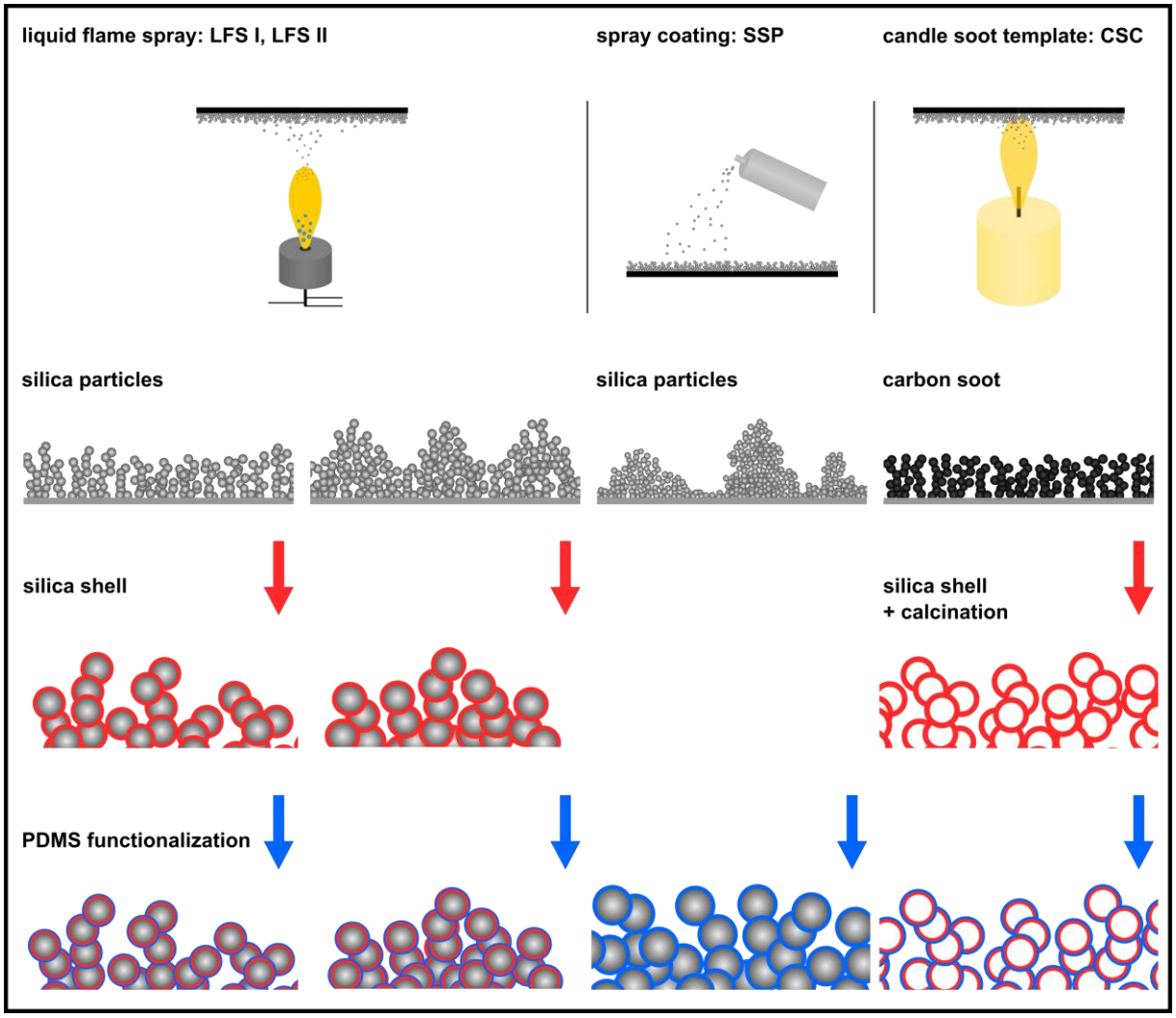

Figure 3.5. Schematic illustration of sample preparation: Silica particles prepared via liquid flame spray and carbon soot from a candle flame are coated with a silica shell via CVD (red). Thereafter, the candle soot template is calcinated causing combustion of the carbon core. In a final step, all samples are functionalized with PDMS (blue), rendering them super-liquid-repellent.

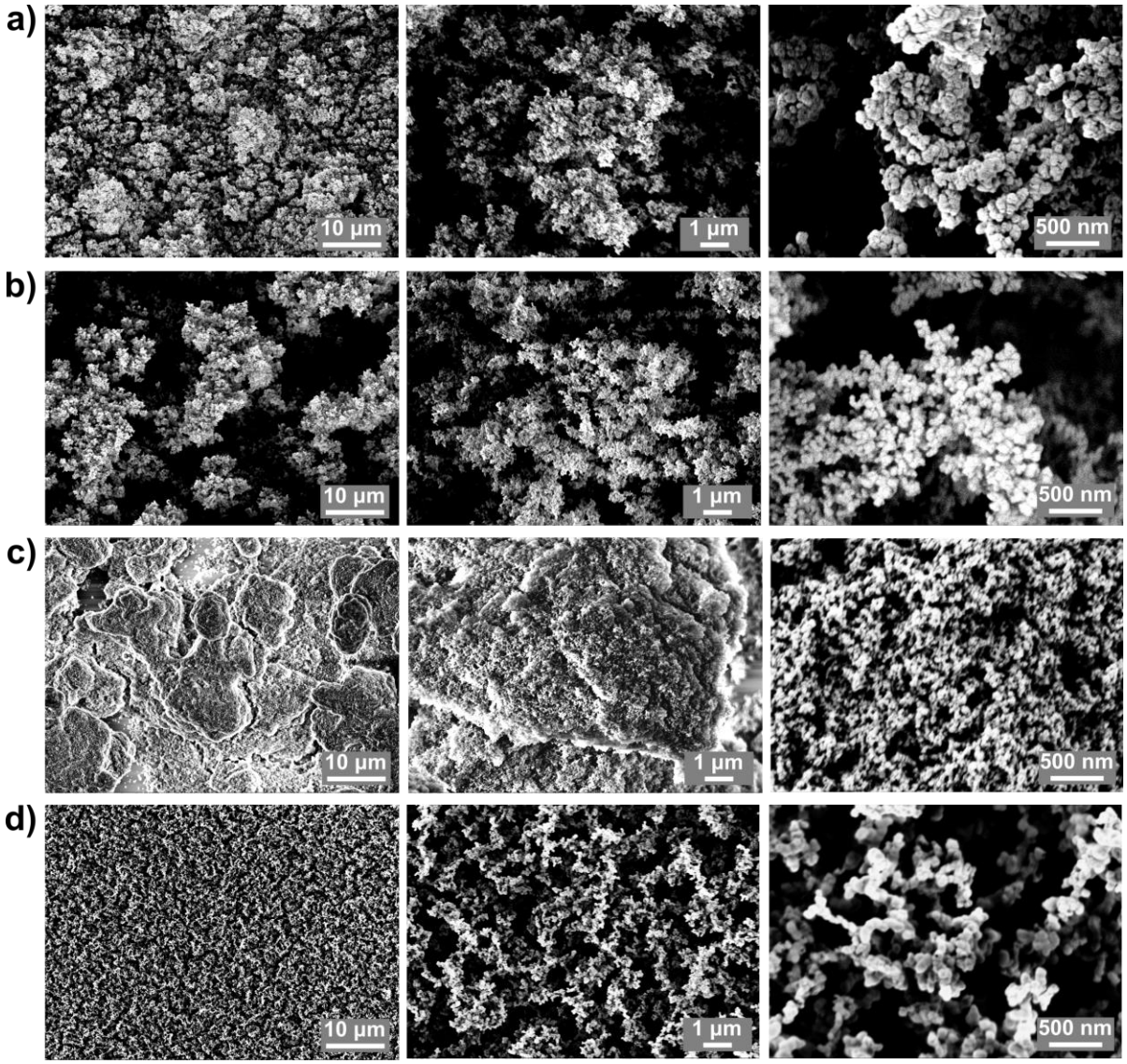

Figure 3.6. Top-view scanning electron microscopy images of the model surfaces at different magnifications: a) LFS I, coated for 3 min at 15 cm distance, b) LFS II, coated for 2 min at 10 cm distance, c) sprayed silica particles, and d) candle soot coating. LFS: liquid flame spray; SSP: sprayed silica particles; CSC: candle soot coating.

Characterization. The morphology of the particle-based surface structures was analyzed via scanning electron microscopy (Figure 3.6). Images were acquired at a voltage of 0.5 to 3 kV using an InLens Detector, LEO 1530 Gemini, Zeiss. To reduce charging effects, the surfaces were coated with a 9 nm thick Pt layer (BalTec MED 020 Modular High Vacuum Coating System, Argon at 2×10^{-2} mbar and 30 mA).

The wetting properties of the coatings were analyzed using a contact angle goniometer (DSA100S, KRÜSS). The wettability toward different probe liquids was investigated, namely water, water-ethanol solutions, diiodomethane, ethylene glycol, and hexadecane. For water-ethanol solutions, the surface

tension was gradually decreased by increasing the fraction of ethanol in steps of 5 wt%. Surface tensions were measured using the pendant drop method and showed good agreement with literature values[186]. The wetting properties were analyzed via the apparent static contact angle and the roll-off angle. The advancing contact angle should be close to 180°, thus too high to be measured using a contact angle goniometer.[37] The measurement of the receding contact angle on rough, super-liquid-repellent surfaces suffers from variations of the contact angle by a few degrees caused by pinning sites. Therefore, the apparent contact angle which takes a value between the advancing and receding contact angle is determined.[37] The apparent contact angles were measured from carefully deposited 6 µL drops. Roll-off angles were measured by placing a 6 µL drop onto the surface and subsequently tilting the surface at a rate of 0.5 degrees per second until the drop rolled completely out of the field of view. A minimum of 6 spots was analyzed for each surface.

Drop impact was measured using water and a water-ethanol solution (35 wt% EtOH, γ = 31.0 mN m^{-1}) on a liquid flame spray I surface functionalized with PDMS and PFOTS. The substrate was tilted by 15°. Drops were produced at a height of 3.5 mm above the substrate using a gauge 32 needle. This resulted in drop volumes of approximately 4 µL and 2.3 µL for water and the water-ethanol solution, respectively. Drop impact was recorded using a high-speed camera (Fastcam AX10, Photron) and a high magnification objective (2x, Mitutoyo) at a frame rate of 5000 frames per second.

Furthermore, we measured the friction force F_F between a drop and a surface using a dynamic adhesion force instrument (DAFI). The drop is pushed over the surface at constant velocity using a glass capillary. The friction causes a deflection of the capillary. According to Hooke's law, the force required to move the drop is equal to the deflection of the cantilever Δx multiplied by the spring constant of the capillary k_s:

$$F_F = k_s \cdot \Delta x. \tag{16}$$

If the drop friction is dominated by contact line friction, it has been shown that the force can be calculated using Furmidge's equation. The Furmidge equation is used to calculate the force of a drop just before motion. The so-termed lateral adhesion force (or static friction force) follows from the integration of the horizontal component of the liquid-air surface tension γ along the three-phase contact line[6,45,187,188]:

$$F_F = k \cdot w \cdot \gamma \cdot (\cos \theta_R - \cos \theta_A), \tag{17}$$

where w is the drop contact width, and θ_R and θ_A are the apparent receding and advancing contact angles of the drop, respectively. The dimensionless factor k accounts for angular variations of the contact angle around the contact line, where $k \leq 1$. When the drop is in continuous motion, friction opposes the motion.

Motion also changes the contact width and the advancing and receding contact angle which become a function of velocity:

$$F_F = k \cdot w(v) \cdot \gamma \cdot (\cos \theta_R(v) - \cos \theta_A(v)). \quad (18)$$

According to Eq. 18, friction decreases with decreasing interfacial tension. It increases with increasing contact width. For drops on a hydrophobic surface, friction also increases for decreasing rear contact angles.

Friction forces were analyzed using water and a water-ethanol solution (20 wt% EtOH, γ = 37.7 mN m^{-1}). 15 µL drops of the respective probe liquid were placed onto the surface and brought into contact with the sensor. Then, the surface was moved at a constant velocity of 0.5 mm s^{-1} over a distance of 25 mm. The deflection of the sensor was analyzed using a Matlab script from side-view videos and the friction force was calculated from equation 1. Since drop friction is volume-dependent, the forces were normalized to the radius of the 15 µL drop (r = 1.5 mm from $(^{3V}/_{4\pi})^{1/3}$). The radius was chosen for normalization because the contact width perpendicular to the direction of surface motion is not accessible with a goniometer. Furthermore, this is in analogy to the normalization in colloidal probe atomic force microscopy. As a sensor, a glass capillary (50 mm x 0.5 mm x 0.05 mm, CM Scientific Ltd.) with a stiffness of 105 µN mm^{-1} was used. The sensor was calibrated by monitoring the deflection of the end of the glass capillary when a known load is applied. For each surface, three spots were analyzed using fresh probe liquid for each scan.

The measured friction forces (F_{exp}) were compared to values calculated according to Eq. 18 with k = 1 (F_F, Table 1). Since the contact width w is not accessible with goniometry, the contact length along the direction of surface motion in the kinetic state was used.

For both LFS surfaces and the candle soot surface, the calculated forces slightly exceed the experimental values. There are several possible sources of error in the calculation of the friction forces: for super-liquid-repellent surfaces, the contact width and the contact length may vary by up to 20 %. Furthermore, the macroscopic advancing and receding contact angles measured from the video files may be off by a few degrees. The contact angles could be influenced by gravity and by the capillary, which may slightly pull up the drop on the advancing side. Only in the case of the spray-coated surface, the calculated values are lower than the experimental values. This may be due to the pronounced stick-slip motion that does not become apparent in the advancing and receding contact angle used for the calculation.

For the LFS and the spray-coated surfaces, a decrease in the friction forces in line with a decrease of the probe liquid's surface tension is observed. In case of the candle soot surface, both the experimental and the calculated friction forces increase with decreasing surface tension due to a change in the solid-liquid interfacial area and the receding contact angle.

3.5 Supporting Information

Table 1. Friction forces from experiments (F_{exp}) and forces calculated using Eq. 18 (F_F). Both values were normalized to the drop radius of r = 1.5 mm. Experimentally, the friction forces were determined from the deflection of a flexible glass capillary in contact with the drop while the substrate was moved at a constant velocity. The force was calculated according to equation 1. 15 µL drops of water (γ = 72.0 mN m^{-1}) and a water-ethanol solution (20 wt% EtOH, γ = 37.7 mN m^{-1}) were used as probe liquids. LFS: liquid flame spray; SSP: sprayed silica particles; CSC: candle soot coating.

Sample	γ / mN m^{-1}	F_{exp} / µN	$F_{exp}\, r^{-1}$ / µN mm^{-1}	F_F / µN	$F_F\, r^{-1}$ / µN mm^{-1}
LFS I - PDMS	72.0	2.7	1.8	4.6	3.0
	37.7	1.7	1.1	2.8	1.8
LFS II - PDMS	72.0	3.2	2.1	5.3	3.6
	37.7	1.6	1.1	1.7	1.1
SSP - PDMS	72.0	5.2	3.4	4.5	3.0
	37.7	3.9	2.6	2.0	1.3
CSC - PDMS	72.0	3.4	2.3	5.0	3.3
	37.7	5.6	3.7	5.8	3.9

Table 2. Contact angle (θ) and roll-off angle ($\theta_{roll\text{-}off}$) measurements conducted on different PDMS-functionalized surfaces. 6 µL drops of water, water-ethanol solutions, diiodomethane (DI), and ethylene glycol (EG) were used as probe liquids. The surface tension of water-ethanol solutions was gradually reduced by increasing the ethanol fraction in steps of 5 wt% to a maximum of 35 wt%. Apparent contact and roll-off angles were recorded until the Cassie-to-Wenzel transition occurred. LFS: liquid flame spray; SSP: sprayed silica particles; CSC: candle soot coating.

	LFS I - PDMS		**LFS II - PDMS**		**SSP - PDMS**		**CSC - PDMS**	
γ / mN m^{-1}	θ	$\theta_{roll\text{-}off}$	θ	$\theta_{roll\text{-}off}$	θ	$\theta_{roll\text{-}off}$	θ	$\theta_{roll\text{-}off}$
72.0	170±1°	1±1°	169±1°	1±1°	169±1°	3±1°	168±2°	3±1°
57.6	170±1°	1±1°	170±1°	1±1°	169±1°	2±1°	167±1°	2±1°
46.4	169±1°	1±1°	170±1°	1±1°	168±1°	2±1°	166±1°	2±1°
41.6	169±1°	1±1°	169±1°	1±1°	169±1°	3±1°	164±1°	4±1°
37.7	169±1°	2±1°	169±1°	2±1°	168±1°	4±1°	163±2°	5±1°
34.8	169±1°	2±1°	168±1°	3±1°	166±1°	8±1°	162±2°	12±1°
32.8	167±1°	4±1°	166±1°	4±1°			153±1°	> 10°
31.0	163±1°	7±1°						
50.9 (DI)	158 ±1°	4±1°	160±1°	3±1°	165±1°	4±1°	164±1°	6±1°
47.7 (EG)	168±1°	2±1°	165±1°	3±1°			165±1°	8±1°

Table 3. Contact angle (θ) and roll-off angle ($\theta_{roll\text{-}off}$) measurements conducted on different PFOTS-functionalized surfaces. 6 µL drops of water, a 35 wt% water-ethanol solution (EtOH), diiodomethane (DI), ethylene glycol (EG), and hexadecane (HD) were used as probe liquids. LFS: liquid flame spray; SSP: sprayed silica particles; CSC: candle soot coating.

	LFS I - PFOTS		**LFS II - PFOTS**		**SSP - PFOTS**		**CSC - PFOTS**	
γ / mN m^{-1}	θ	$\theta_{roll\text{-}off}$	θ	$\theta_{roll\text{-}off}$	θ	$\theta_{roll\text{-}off}$	θ	$\theta_{roll\text{-}off}$
72.0 (H_2O)	166±1°	2±1°	165±1°	2±1°	169±1°	1±1°	167±1°	1±1°
50.9 (DI)	168±1°	2±1°	167±1°	1±1°	168±1°	2±1°	169±1°	1±1°
47.7 (EG)	169±1°	2±1°	167±1°	2±1°	167±1°	2±1°	168±1°	5±1°
31.0 (EtOH)	167±1°	4±1°	167±1°	7±1°	167±1°	11±1°	159±1°	23±1°
27.6 (HD)	167±1°	3±1°	163±1°	4±1°	167±1°	5±1°	163±1°	9±1°

3.6 Author Contributions

K.I.H. and [redacted] conceived and designed experiments. [redacted] fabricated the surfaces and performed all contact angle experiments. [redacted] performed the friction force measurements. [redacted] contributed with conceptual advice. K.I.H. wrote the manuscript, supported by [redacted] and [redacted] All authors approved the manuscript.

3.7 Acknowledgments

The authors would like to thank [redacted] and [redacted] for stimulating discussions and [redacted] for technical support. This project was supported by the Max Planck Graduate Center (K.I.H.), by the German Research Foundation (DFG) with the Priority Program 2171 ([redacted]) and the Collaborative Research Center 1194 ([redacted]).

4 Effect of Solid-Liquid Interactions on the Wettability of Super-Liquid-Repellent PDMS Surfaces

Katharina I. Hegner, [redacted], [redacted]

Physics at Interfaces, Max Planck Institute for Polymer Research, Ackermannweg 10, 55128 Mainz, Germany

E-mail: [redacted]

Keywords: fluorine-free, liquid-like, swelling, solubility

This manuscript is currently in the final stages of preparation and is close to submission.

Abstract

Super-liquid-repellent surfaces rely on a combination of roughness and low surface energy, usually achieved by functionalization with fluoroalkyl substances. Growing concerns about this class of chemicals have sparked an interest in fluorine-free alternatives. The functionalization with non-toxic, biocompatible polydimethylsiloxane presents a promising alternative. Smooth surfaces functionalized with liquid-like polydimethylsiloxane have been extensively studied for their ability to repel water and non-polar, low surface tension liquids. Suitable solvents have been observed to swell the polymer chains and thereby, improve the liquid-like nature. The question arises as to how this behavior affects Cassie state drops on structured surfaces. Here, we observe the adverse effect: increased solid-liquid interactions cause the liquid to wet a larger portion of the particle structures, introducing more pinning sites. In case of strong interactions, the Cassie-to-Wenzel transition may occur regardless of comparatively high surface tensions. The extent of solid-liquid interactions and therefore, the swelling of PDMS chains, can be estimated using swelling ratios and solubility parameters. Combined with surface tension, these parameters allow the understanding and characterization of wetting on smooth and rough surfaces.

4.1 Introduction

Repellency toward water, organic liquids, and oils is a desirable surface feature that can introduce self-cleaning[105,174], anti-biofouling[114,124,125], or anti-icing[7,189] properties. Inspired by structures found on plants[51] and insects[52], the field of artificial superhydrophobic or superamphiphobic surfaces[61,74,153] has grown rapidly. Super-liquid-repellency ($\theta_{receding} > 150°$ and $\theta_{roll\text{-}off} < 10°$) is based on two principles: suitable surface roughness and low surface energy allow drops to rest on top of solid protrusions and air entrapped between the structures, thereby reducing the solid-liquid interface.[19,26]

While superhydrophobic surfaces are able to repel water, low surface tension liquids can still penetrate the underlying structures. To achieve superamphiphobicity toward organic and oily liquids, surface features with so-called overhang or re-entrant structures are required.[19,62] The surface energy is typically minimized via functionalization with perfluoroalkyl substances. However, the application of this group of chemicals becomes increasingly restricted because of concerns regarding their persistency and mobility in the environment, their ability for bioaccumulation, and their effect on the human health.[80]

Functionalization with polydimethylsiloxane (PDMS) offers a promising alternative to conventional fluorinated surfaces: PDMS is non-toxic, biocompatible, and has a low surface energy of approximately 20 mN m^{-1}.[89] Due to its many desirable properties, wetting of liquid-repellent[50,91,95,103] and superhydrophobic[17,97,98,180,190] PDMS surfaces, specifically, liquid-like PDMS surfaces, by water and other probe liquids has been widely studied. These surfaces consist of covalently bonded, linear PDMS chains. Because of the low glass transition temperature and the low torsional barrier of the Si-O bond, the chains are highly mobile. [35,50,96,101] On smooth surfaces, excellent amphiphobic behavior has been observed: although drops may exhibit apparent contact angles below 40°, they hardly pin and can be removed when tilting the surface by a few degrees. This particular wetting behavior was explored by McCarthy et al.[50,101] and Hozumi et al.[35] who attributed it to the liquid-like properties of surface-tethered PDMS chains. It has been proposed that the PDMS chains adapt to increasing interactions with most non-polar probe liquids by swelling and chain stretching (Figure 4.1a).

Spontaneous surface adaptation due the contact with a liquid can be observed for a range of surfaces. The adaptation may result from polymer reconstruction, diffusion and swelling, reorganization of mixed polymer brushes, reconstruction of organic monolayers, and replacement of contaminations or an adsorption layer.[191,192] These time-dependent processes are associated with a change in the solid-liquid interfacial energy. It decreases from the initial value γ_{SL}^{0} to a final value γ_{SL}^{∞}, when equilibrium is reached. In a recently proposed model, Butt et al.[32] assume an exponential decrease in interfacial energy to its

equilibrium value γ_{SL}^{∞}, causing the drop to spread. Depending on the system, the specific adaptation time τ_{SL} can vary between nanoseconds (liquid ordering) and minutes or hours (polymer reorganization). Wetting-induced adaptation of PDMS has been observed, for example, by Wong et al.[33] Here, the crosslinked PDMS adapts to the presence of water via diffusion of mobile oligomers from the PDMS matrix to the surface, effectively introducing lubricating properties. Furthermore, the solvent-dependent swelling of crosslinked PDMS has been investigated as it determines the suitability of PDMS for applications in microfluidics.[193]

The swelling of liquid-like PDMS chains depends on the degree of solid-liquid interactions and thus on the probe liquid's chemical and physical properties. Therefore, adaptation is expected to be reflected in suitable parameters characterizing the interaction between the solvent and the PDMS coatings. Here, the wetting properties are discussed in terms of the Hansen solubility parameter and a swelling ratio.

Wetting on smooth and structured surfaces differs fundamentally. The question arises, how interactions between PDMS and a probe liquid affect the dynamic wettability of PDMS-functionalized super-liquid-repellent coatings. The nanoparticle-based surface was prepared via liquid flame spray (LFS) and has previously shown excellent repellency toward water-ethanol solutions with surface tensions as low as 31 mN m^{-1}. Here, we investigate the wetting behavior toward different types of liquids with respect to surface tension, solubility parameters, and swelling ratios.

4.2 Results and Discussion

Herein, we investigate the influence of different probe liquids on the wettability of PDMS-functionalized particle-based structures, generated using LFS (Figure 4.1c). In LFS, a liquid feed consisting of the precursor (tetraethoxysilane) and a solvent (isopropanol) is finely dispersed into a flame. The droplets evaporate and the precursor combusts. Nucleation of silica particles takes place. Particles grow and may collide, agglomerate, and sinter. Depending on a number of parameters such as the precursor concentration, the liquid and gas feed rates, and the distance between the flame and the substrate used for particle collection, the nano- and microscale surface structures may vary.[70,72,73]

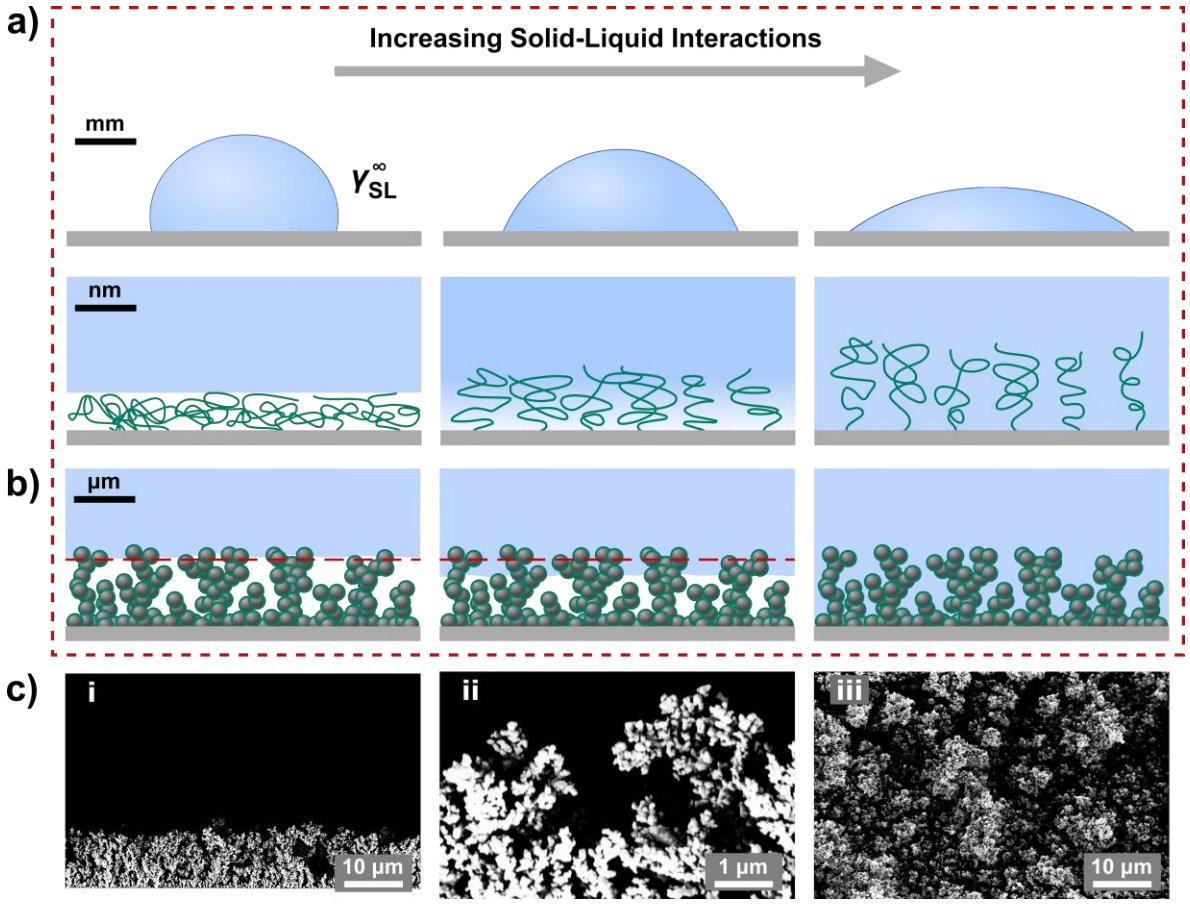

Figure 4.1. Behavior of surfaces functionalized with PDMS chains upon contact with a probe liquid. a) Schematic illustration of a smooth surface. On the macroscale, increasing solid-liquid interactions cause probe liquids to form lower apparent contact angles. On the nanoscale, increasing affinity with the probe liquid causes swelling of the PDMS chains and the formation of a blended interface. b) On nanoparticle-based surfaces in the Cassie state, liquids rest on top of surface protrusions and air between the structures. Increasing solid-liquid compatibility may cause the liquid to sink further down the structures and eventually result in the liquid completely penetrating the structures. c) i,ii Side-view, and iii top-view SEM micrographs of the particle-based surface prepared via LFS at different magnifications.

Afterward, the silica particles are functionalized with a thin layer of covalently bonded PDMS. The reaction takes place in the gas phase, at room temperature and humidity.[96]

Upon PDMS-functionalization the surface successfully repels water-ethanol solutions (orange) with surface tensions down to 31 mN m^{-1} (Figure 4.2a,b). The surface tension was gradually reduced by increasing the amount of ethanol in steps of 5 wt%. However, both polar liquids are expected to exert a low degree of solid-liquid interactions and swelling of PDMS. Therefore, we prepared a range of Triton X100 surfactant solutions. Minute amounts of the nonionic surfactant TX 100 are sufficient to reduce the surface tension (cmc = 0.33 mM). The surfactant molecules accumulate at the drop interface where the non-polar carbon group can interact with the PDMS surface. The bulk polarity of the aqueous Triton X100 solution can be assumed as constant. Compared to water-ethanol solutions, we observed an earlier deterioration in wettability with decreasing surface tension (Figure 4.2b). While a water-ethanol solution with a surface tension of 31 mN m^{-1} can easily roll and bounce off the surface, the lower limit for TX100 solutions is at a surface tension of approximately 39.0 mN m^{-1}. Drops of a solution with a surface tension of 33.0 mN m^{-1} stick to the surface.

Furthermore, standard test liquids and oils were investigated. For diiodomethane (DI, γ = 50.9 mN m^{-1}) and ethylene glycol (EG, γ = 47.7 mN m^{-1}) the coating exhibits roll-off angles of 5° and 3°, respectively (Figure 4.2c). Two different oils, namely castor oil (CO, $\gamma \approx 39$ mN m^{-1}) and peanut oil (PO, γ = 34.5 mN m^{-1}) are examined because of their comparatively high surface tensions. Both are composed of a range of different fatty acids. The two oils immediately spread into the structures forming contact angles between 10° and 20°. Finally, the fluorinated ionic liquid [C_4mim][NTf_2] (IL, γ = 33.6 mN m^{-1})[194] is investigated: the ionic liquid also spreads into the structures, resulting in contact angles of approximately 30°.

The results show that surface tension alone does not fully determine the behavior of a probe liquid in contact with the PDMS surface. Interactions between surface and probe liquid determine the interfacial energy and thereby, the position of the contact line and the contact angle formed on a particle-based surface (Figure 4.2d,e). For liquids with low surface tension, local fulfillment of the chemical contact angle causes the liquid to wet a larger portion of the particle structure (Figure 4.2e). The contact angle may be further reduced by increased swelling of the PDMS layer, causing the three-phase contact line to depin and move further down the particle aggregate.

On a macroscale, deeper penetration of the liquid into the structures causes an increase in the solid-liquid interface (Figure 4.1b). A greater number of pinning sites results in a deterioration of drop mobility. In

the extreme case of the two non-polar oils and the ionic liquid, enhanced solid-liquid interactions cause the liquids to spread into the structures, regardless of their comparatively high surface tensions.

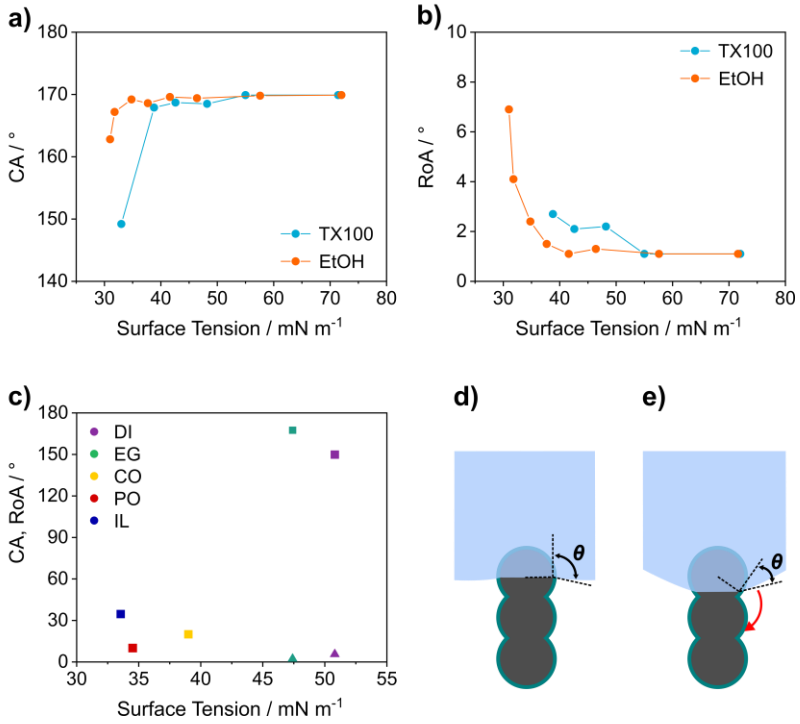

Figure 4.2. Wettability of nanoparticle-based surfaces functionalized with PDMS. a) Apparent static and b) roll-off angles using 6 µL drops of aqueous Triton X100 (TX100, blue) and ethanol (EtOH, orange) solutions. The surface tension is gradually reduced by increasing the surfactant concentration and the ethanol weight percentage, respectively. c) Apparent static (■) and roll-off angles (▲) using 6 µL drops of diiodomethane (DI, γ = 50.9 mN m^{-1}), ethylene glycol (EG, γ = 47.7 mN m^{-1}), castor oil (CO, $\gamma \approx$ 39 mN m^{-1}), peanut oil (PO, γ = 34.5 mN m^{-1}), and the ionic liquid [C_4mim][NTf_2] (IL, γ = 33.6 mN m^{-1}). Schematic of a particle aggregate with a liquid interface. d) In case of a low degree of solid-liquid interactions, local fulfillment of the chemical contact angle results in a metastable Cassie state. e) Liquids with a high degree of solid-liquid interactions form lower contact angles and depinning can occur more easily.

For the successful implementation of fluorine-free super-liquid-repellent surfaces, defining and understanding the limits of liquid-repellency is essential. Typically, the performance of this class of surfaces is discussed in terms of the liquid's surface tension. However, the previous experiments show that surface tension by itself is insufficient. Super-liquid-repellent surfaces functionalized with an adaptable polymer layer require a discussion in terms of interaction parameters.

Smooth surfaces of the same chemical nature allow a more detailed analysis of the wetting behavior of different types of liquids. Therefore, smooth liquid-like surfaces are prepared from silicon wafers via chemical vapor deposition. After the synthesis, non-bonded oligomers are removed by washing the

surfaces in toluene, isopropanol, and water for 30 s each. Measurements with Atomic Force Microscopy (AFM) reveal a roughness of only Ra ≈ 0.15 nm over an area of 3 x 3 µm^2 (Figure 4.3a). Probe liquids with a range of surface tensions, Hansen solubility parameters, and swelling ratios are used to investigate the wetting properties. Contact angles are measured using water (γ = 72.8 mN m^{-1}), aqueous ethanol (35 wt% EtOH, γ = 31.0 mN m^{-1}) and an aqueous Triton X100 solution (TX100, γ = 39.0 mN m^{-1}). Furthermore, diiodomethane (DI, γ = 50.9 mN m^{-1}), ethylene glycol (EG, γ = 47.7 mN m^{-1}), and toluene (TOL, γ = 28.5 mN m^{-1}) were utilized as test liquids.

Independent of other physical properties, the liquids exhibit an increase in apparent static and advancing contact angle with increasing surface tension (Figure 4.3b,c). Deviations from this trend can only be observed for diiodomethane. However, the receding contact angles and the resulting contact angle hysteresis differ substantially, depending on the type of liquid.

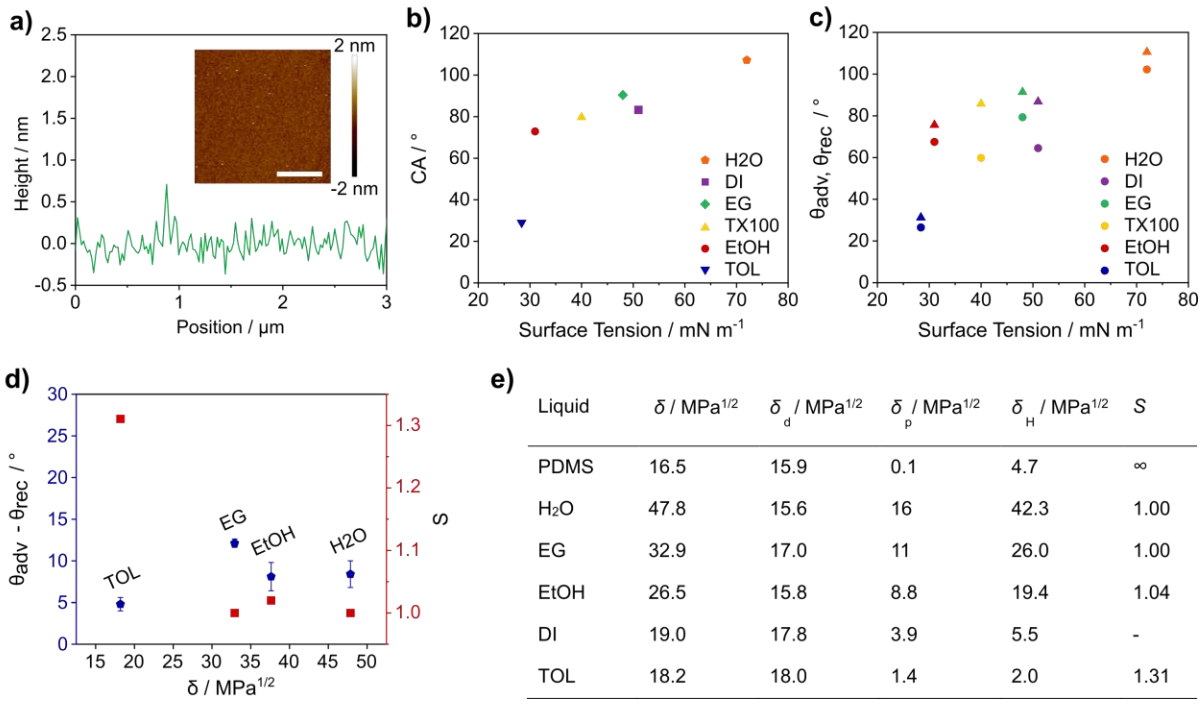

e)

Liquid	δ / MPa$^{1/2}$	δ_d / MPa$^{1/2}$	δ_p / MPa$^{1/2}$	δ_H / MPa$^{1/2}$	S
PDMS	16.5	15.9	0.1	4.7	∞
H_2O	47.8	15.6	16	42.3	1.00
EG	32.9	17.0	11	26.0	1.00
EtOH	26.5	15.8	8.8	19.4	1.04
DI	19.0	17.8	3.9	5.5	-
TOL	18.2	18.0	1.4	2.0	1.31

Figure 4.3. Wettability of smooth PDMS-functionalized surfaces. a) Vertical profile and morphology over an area of 3 x 3 µm^2 of a PDMS-functionalized silicon wafer acquired by AFM. b) Apparent static contact angles and c) advancing (▲) and receding (●) contact angles using water (H2O), diiodomethane (DI), ethylene glycol (EG), one aqueous Triton X100 (TX100) and one ethanol solution (EtOH), and toluene (TOL). Errors in measurements typically fall within ± 1° and are smaller than the symbol sizes in the figures. d) Contact angle hysteresis and swelling ratio *S* vs. the Hansen Solubility Parameter δ. e) Properties of the probe liquids: Hansen solubility parameters with the dispersive, polar, and hydrogen-bonding components[195,196], and swelling ratios[193].

To understand the differences in the repellency toward the various probe liquids, the Hansen solubility parameter[195,197] and the swelling ratio of PDMS[193] in the respective liquid are considered. The Hansen solubility parameter is related to the interfacial tension and describes the cohesive energy from intermolecular attractive interactions within a material. The parameter is composed of the dispersive, polar, and hydrogen-bonding components. As a first approximation, materials with similar parameters interact stronger with one another.[195,197] The swelling ratios employed here were determined by Lee et al. A solid piece of crosslinked PDMS (ratio between oligomer to crosslinker was 10:1 by weight) was placed in different solvents for 24 h and thereafter, the change in dimensions of the solid was measured in the solvents.[193] While they did not observe a linear relationship between solubility parameter and swelling ratio, moderate to high swelling of crosslinked PDMS was typically observed for liquids with solubility parameters of less than 20 $MPa^{1/2}$. The solubility parameter of PDMS is 16.5 $MPa^{1/2}$ with a dispersive component of 15.9 $MPa^{1/2}$ and a comparatively low polar component of 0.1 M[196]

Indeed, the lowest contact angle hysteresis of 5° ± 1° is observed for toluene which has a solubility parameter of 18.2 $MPa^{1/2}$ and a swelling ratio of 1.31. Even though toluene forms apparent static contact angles of 29° ± 1°, thereby increasing the solid-liquid interface, it exhibits a low contact angle hysteresis. The solubility of PDMS in toluene was further confirmed by preparing a 50 wt% solution of PDMS (1000 cSt).

Although diiodomethane has a fairly low solubility parameter, the contact angle hysteresis is comparatively large. The swelling ratio is not available. However, preparing merely a 5 wt% PDMS (1000 cSt) solution was not possible, demonstrating the low compatibility. Diiodomethane as a probe liquid shows that there are limitations to using the readily available Hansen solubility parameter for gauging the solid-liquid interactions.

On the other hand, solvents with higher solubility parameters and low swelling ratios such as water, ethylene glycol, and the water-ethanol solution exhibit higher contact angle hysteresis than toluene (Figure 4.3d). This corresponds to the trend observed by Lee et al.: larger differences in solubility parameters result in little interaction with and swelling of the PDMS chains and therefore, no measurable improvement of the liquid-like properties.

For the aqueous surfactant solution (TX 100) stronger interactions are expected, namely by the non-polar 4-(1,1,3,3-tetramethylbutyl)-phenyl group oriented toward the PDMS chains. However, the solution exhibits a comparatively high contact angle hysteresis. This may be due to a non-equilibrium distribution of the surfactant molecules at the interface during dispensing and retrieving volume from the drop: while

volume is added, a low surfactant concentration at the three-phase contact line may introduce a higher surface tension and less solid-liquid interactions, locally. In contrast, while volume is retrieved, interactions of the non-polar carbon group with PDMS may result in an enhanced surfactant concentration at the solid-liquid interface.[198]

The experiments show that liquids that interact more strongly with the PDMS functionalization, i.e. cause more swelling, exhibit lower contact angle hysteresis. The wetting behavior of most one-component liquids can be related to the swelling ratio and/or the solubility parameter.

While a high degree of solid-liquid interactions has proven to enhance the wetting properties of liquid-repellent surfaces, the opposite effect can be observed on structured surfaces. For non-polar oils, both the solubility parameters and the swelling ratios suggest a high degree of interaction. Indeed, both the castor and peanut oil immediately wet the surface, regardless of the comparatively high surface tensions. Superior super-liquid-repellency is observed for liquids that exhibit low swelling ratios and/or dissimilar solubility parameters. Here, water-ethanol solutions with surface tensions of only 31 mN m^{-1}, diiodomethane, and ethylene glycol can be easily repelled.

Different behavior is observed for TX100 solutions where drops of 33.0 mN m^{-1} already fail to roll off the surface. The surfactant exhibits a low receding contact angle on smooth PDMS-functionalized surfaces, suggesting enhanced solid-liquid interactions at the receding three-phase contact line due to surfactant accumulation. This may explain the abrupt deterioration in super-liquid-repellency with increasing surfactant concentration.

4.3 Conclusion

Our results show that the consequences of wetting-induced surface adaptation are vastly different on smooth and structured surfaces. On smooth surfaces, swelling of the covalently bonded PDMS chains due to strong solid-liquid interactions reduces the number of pinning sites and the contact angle hysteresis, causing drops to roll off easily. On structured surfaces, on the other hand, stronger interactions cause the probe liquid to penetrate the coating and remain pinned to the surface. The degree to which probe liquids interact with and cause swelling of the PDMS layer can usually be estimated via the Hansen solubility parameter and a swelling ratio. Combined with the surface tension, these parameters allow the characterization of the surface’s wetting properties.

4.4 Methods

Materials. Tetraethoxysilane (98 %) and 1-butyl-3-methylimidazolium bis(trifluoromethanesulfonyl)imide (≥ 98.0 %) were purchased from Sigma Aldrich. Isopropanol (≥ 99.8 %), hexane (> 95 %), toluene (≥ 99.8 %), and castor oil were purchased from Thermo Fisher Scientific. Aqueous ammonia solution (25 %) was purchased from VWR Chemicals. Ethanol (≥ 99.8 %) was purchased from Honeywell. 1,3-dichlorotetramethyldisiloxane (96 %) and Triton X-100 were purchased from Alfa Aesar. Ethylene glycol (99.8 %, anhydrous) was purchased from Acros Organics. Diiodomethane (> 98.0 %) was purchased from TCI. Glass substrates were purchased from Thermo Fisher Scientific. Silicon wafers were purchased from Si-Mat (Kaufering, Germany).

Surface preparation. The nanoparticle-based surfaces were prepared using liquid flame spray according to the procedure described in Chapter 3.4. Thereafter, the samples were activated with oxygen plasma (Diener Electronic Femto, 6 cm^3 min^{-1} oxygen flow rate) for 10 min at 300 W. The samples were placed in a desiccator (2.150 cm^3) together with 50 µL 1,3-dichlorotetramethyldisiloxane (96 %, Alfa Aesar) and the reaction was allowed to proceed at ambient temperature (21 °C) and ambient humidity (40 – 60 %) for 1.5 h. Thereafter, non-covalently bonded oligomers were removed by placing the samples in a vacuum oven (200 mbar) for 2 h at 60 °C.

To prepare smooth PDMS surfaces, plasma-activated silicon wafers (10 min at 300 W) were placed in a desiccator (2.150 cm^3) together with 50 µL 1,3-dichlorotetramethyldisiloxane (96 %, Alfa Aesar) and the reaction was allowed to proceed at ambient temperature (21 °C) and ambient humidity (40 – 60 %) for 3.0 h. Non-bonded oligomers were removed by washing the samples in toluene, isopropanol, and water for a minimum of 30 s each.

Characterization. The morphology of the particle-based surface structures was analyzed via scanning electron microscopy. Images were acquired at a voltage of 3 kV using an InLens Detector, LEO 1530 Gemini, Zeiss. To enhance the image quality and reduce charging effects, surfaces were coated with a 9 nm thick Pt layer (BalTec MED 020 Modular High Vacuum Coating System, Argon at 2×10^{-2} mbar and 30 mA).

Furthermore, the surface topography was analyzed via scanning force microscopy. Measurements were performed with a soft tapping mode in air (Bruker, Dimension ICON). An OTESPA silicon probe was used (Bruker, nominal spring constant 26 N m^{-1} and a nominal resonance frequency of 300 kHz).

The wetting properties were analyzed using a goniometer (DSA100S, KRÜSS). Errors in measurements typically fall within ± 1° and are smaller than the symbol sizes in the figures. Contact angles of 6 µL drops were measured. For roll-off angles, a 6 µL drop was deposited onto the surface which was subsequently tilted at a rate of 1° per second until the drop rolled completely out of the field of view. A minimum of 6 spots was analyzed for each surface. Advancing and receding contact angles were measured by adding and retrieving a volume of 15 µL in the case of toluene and 30 µL for all other test liquids to a 5 µL drop at a rate of 0.5° per second. A minimum of 6 spots were analyzed for two sets of surfaces each. The surface tension of aqueous ethanol and TX100 solutions was measured using the pendant drop method.

4.5 Supporting Information

Table 4. Contact angle (θ) and roll-off angle ($\theta_{roll\text{-}off}$) measurements conducted on PDMS-functionalized silicon wafers. 6 µL drops of water, water-ethanol solutions, and aqueous TX 100 solution (TX 100) were used as probe liquids. The surface tension of water-ethanol solutions was gradually reduced by increasing the ethanol fraction in steps of 5 wt% to a maximum of 35 wt%. Apparent contact and roll-off angles were recorded until the Cassie-to-Wenzel transition occurred.

water-ethanol solutions			TX 100 solutions		
γ / mN m^{-1}	$\boldsymbol{\theta}$	$\boldsymbol{\theta_{roll\text{-}off}}$	γ / mN m^{-1}	$\boldsymbol{\theta}$	$\boldsymbol{\theta_{roll\text{-}off}}$
72.0	169.9±0.7°	1.1±0.2°	72.0	169.9±0.7°	1.1±0.2°
57.6	169.8±0.7°	1.1±0.3°	55.0	169.9±0.8°	1.5±0.2°
46.4	169.4±0.9°	1.3±0.4°	48.2	168.5±1.0°	1.4±0.4°
41.6	169.6±0.6°	1.1±0.1°	42.6	168.7±0.8°	3.9±0.8°
37.7	168.6±1.1°	1.5±0.2°	38.8	167.9±1.0°	5.1±1.3°
34.8	169.2±0.8°	2.4±0.3°	33.0	149.2±0.5°	
32.8	167.2±1.0°	4.1±0.6°			
31.0	162.8±1.0°	6.9±1.3°			

Table 5. Contact angles (θ), advancing and receding contact angles (θ_{adv}, θ_{rec}), and contact angle hysteresis (θ_{adv} - θ_{rec}) measured on PDMS-functionalized silicon wafers. 6 µL drops of water (H_2O), diiodomethane (DI), ethylene glycol (EG), an aqueous TX 100 solution (TX 100), a 35 wt% water-ethanol solution (EtOH), and toluene (TO) were used as probe liquids.

γ / mN m^{-1}	$\boldsymbol{\theta}$	$\boldsymbol{\theta_{adv}}$	$\boldsymbol{\theta_{rec}}$	$\boldsymbol{\theta_{adv}}$ **-** $\boldsymbol{\theta_{rec}}$
72.0 (H_2O)	107.2±0.6°	110.6±0.6°	102.2±0.9°	8.4±1.6°
50.9 (DI)	83.3±1.4°	86.8±0.7°	64.5±0.7°	22.3±1.3°
47.7 (EG)	90.4±0.5°	91.4±0.2°	79.3±0.8°	12.2±0.5°
39.0 (TX100)	79.7±0.9°	85.8±1.4°	59.8±2.2°	25.9±0.9°
31.0 (EtOH)	72.9±0.3°	75.6±0.4°	67.5±1.5°	8.1±1.7°
27.6 (TO)	29.0±0.8°	31.2±0.4°	26.5±1.1°	4.8±0.8°

4.6 Author Contributions

K.I.H. and [redacted] conceived and designed experiments. K.I.H. fabricated the surfaces and performed all contact angle measurements. [redacted] contributed with conceptual advice. K.I.H. wrote the manuscript, supported by [redacted] and [redacted] All authors approved the manuscript.

4.7 Acknowledgments

The authors would like to thank [redacted] for technical support. This project was supported by the Max Planck Graduate Center (K.I.H.), the German Research Foundation (DFG) with the Priority Program 2171 ([redacted]), and the Collaborative Research Center 1194 ([redacted]).

5 Capillary Balancing: Designing Frost-Resistant Lubricant-Infused Surfaces

William S. Y. Wong[1,*], Katharina I. Hegner[1], Valentina Donadei[1,2], Lukas Hauer[1], Abhinav Naga[1], and Doris Vollmer[1,*]

[1] Physics at Interfaces, Max Planck Institute for Polymer Research, Ackermannweg 10, 55128 Mainz, Germany

[2] Faculty of Engineering and Natural Sciences, Tampere University, P.O. Box 589, FI-33014 Tampere, Finland

E-mail: wong@mpip-mainz.mpg.de and vollmerd@mpip-mainz.mpg.de

Keywords: slippery surfaces (SLIPS), anti-icing, anti-frosting, capillary pressure, confocal microscopy

The Supporting Information is available from acs.org:
https://pubs.acs.org/doi/10.1021/acs.nanolett.0c02956

Abstract

Slippery, lubricant-infused surfaces (SLIPS) have shown great promise for anti-frosting and anti-icing. However, small length scales associated with frost dendrites exert immense capillary suction pressure on the lubricant. This pressure depletes the lubricant film and is detrimental to the functionality of SLIPS. To prevent lubricant depletion, we demonstrate that interstitial spacing in SLIPS needs to be kept below those found in frost dendrites. Densely packed nanoparticles create the optimally sized nanointerstitial features in SLIPS (Nano-SLIPS). The capillary pressure stabilizing the lubricant in Nano-SLIPS balances or exceeds the capillary suction pressure by frost dendrites. We term this concept capillary balancing. Three-dimensional spatial analysis via confocal microscopy reveals that lubricants in optimally structured Nano-SLIPS are not affected throughout condensation (0 °C), extreme frosting (−20 °C to −100 °C), and traverse ice-shearing (−10 °C) tests. These surfaces preserve low ice adhesion (10-30 kPa) over 50 icing cycles, demonstrating a design principle for next-generation anti-icing surfaces.

5.1 Introduction

Frost formation occurs whenever cold surfaces interact with warmer and more humid environments.[199–202] In Nature, frosting is far more prevalent than icing and can be even more detrimental. The formation of frost on wind turbines, power lines, antennas, or heat exchangers affects operational safety, performance, and efficiency.[126,127] Therefore, novel strategies to prevent frost formation are highly desired.[176,203–205] Among promising anti-icing surfaces,[8,128,129] slippery, liquid-infused, porous surfaces (SLIPS) have been discussed for anti-frosting due to frosting-retardant and ultralow ice adhesion properties. The low ice adhesion enables the removal of ice by environmental forces such as vibration or wind shear.[21,22,204] The lubricant layer confers SLIPS with slippery properties, resulting in low liquid, ice, and frost adhesion capabilities. However, the formation of frost at micrometric length scales exerts a strong capillary suction pressure on the lubricant. The lubricant in the porous layer depletes, resulting in direct frost-to-substrate contact.[9,23,84,131,206–208] When lubricant-covered ice/frost is removed, lubricant which was sucked into frost interstitials is lost.[23,176] Loss of the lubricant leads to increased ice-to-substrate contact and therefore, increased ice adhesion.[176,206]

The pioneering work[22,85] of Quéré, Aizenberg, and Varanasi have described the importance of nanostructures in keeping lubricants in place. Aizenberg et al. described the use of nanostructuring in resisting lubricant depletion from body forces.[208] However, these hierarchical surfaces possess microinterstices, which are susceptible to lubricant depletion. Varanasi et al. studied static equilibrium behaviors of frozen drops with frost, which appear to induce lubricant depletion in both micro- and nanostructured slippery surfaces.[131] Despite the use of nanostructures, lubricant depletion was not prevented, likely due to interstices which are still too large. Therefore, anti-icing and anti-frosting properties of these coatings are potentially ruined after a single frosting event.[9,131,206] To the best of our knowledge, the understanding and control of frost-induced lubricant depletion is still unresolved. To solve this standing problem and to prevent frost-induced depletion in SLIPS, it is important to correlate the characteristic length scales between the surface and the frost. The capillary suction of oil into frost is governed by surface energy and local curvatures of both entities.

Hoarfrost is one of the most common types of frost found in both man-made and natural environments.[209] In the natural environment, crystal sizes vary between 10 μm[210] and 0.2 m.[211,212] Sizes depend on the intensity of undercooling, air circulation, and the amount of moisture.[143,213] Lubricant depletion induced by micrometric frost may be avoidable by designing smaller interstitial spacing (nanointerstices) in SLIPS (Nano-SLIPS) than that found in frost dendrites. Micron-sized

interstices need to be avoided. Therefore, Nano-SLIPS should provide a stabilizing capillary pressure, P_{nS} that exceeds the capillary-induced suction pressure posed by frost dendrites, P_{ice}. We term this design principle "capillary balancing". P_{nS} is approximated by $P_{nS} = \gamma / R_{nS}$, where γ is the surface tension of the lubricant and R_{nS} is the dimension (characteristic radii) of the nanointerstices. P_{ice} is approximated by $P_{ice} = \gamma / R_{ice}$, where R_{ice} is the length scale of air gaps between frost dendrites. Can SLIPS follow the design principle of $P_{nS} > P_{ice}$, resulting in long-lasting anti-icing and anti-frosting surfaces?

To test this design principle, we exposed microinterstices-based Micro-SLIPS and nanointerstices-based Nano-SLIPS at low- to ultralow subzero temperatures (−20 °C to −100 °C) to condensation-frosting. To quantify lubricant depletion, we monitored the dynamic condensation-frosting processes using a custom-built confocal microscope. Here, the capillary pressure stabilizing the smallest interstitially spaced Nano-SLIPS (30 nm) dominates over the capillary suction pressure of the frost dendrites, resulting in a stabilized lubricant layer. Under all tested frosting conditions, lubricants in Nano-SLIPS (30 nm) did not suffer from frost-induced capillary depletion. Our design principle successfully achieved frost-resistant anti-icing surfaces, showing a consistently low ice adhesion (N) per unit area (m^2) of between 10 and 30 kPa over 50 icing cycles.

5.2 Results and Discussion

To assess the influence of capillary balancing on condensation frosting (Figure 5.1), microstructured SLIPS (Micro-SLIPS, 18 μm, μS, Figure 5.1a,b, Supporting Information, Figure 5.5) are investigated alongside as proposed nanostructured SLIPS composed of nanointerstitials (Nano-SLIPS, 30 nm, nS, Figure 5.1c,d). Micro-SLIPS (18 μm, μS) have a maximum spacing between pillars (interstices) of $D_{\mu S,max}$ = 27 μm or $D_{\mu S,mean}$ = 18 μm (Figure 5.1b,h). This corresponds to an effective interstitial radius of $R_{\mu S,mean}$ = 9 μm. The corresponding mean of interstitial spacing ($D_{\mu S/nS,mean}$ or $2 \times R_{\mu S/nS,mean}$) is presented for each variant tested. Nano-SLIPS (30 nm, nS) is comprised of the same micropillar array, infused with a bed of covalently connected (epoxy-amine) nanoparticles (Figure 5.1d, Supporting Information, Methods).

The range of interstitial spacing in Nano-SLIPS (0−60 nm) shows a mean characteristic length scale, $R_{nS,mean}$, of about 15 nm (Figure 5.1g, Figure 5.6), contrasting the interstitial spacing of Micro-SLIPS (10−27 μm), $R_{\mu S,mean}$, at about 9 μm. Differentiating from hierarchical surfaces (micro- and nanostructured), this dense packing of nanoparticles represents a nanostructured layer (between invariant micropillars) that is optimal for capillary balancing.

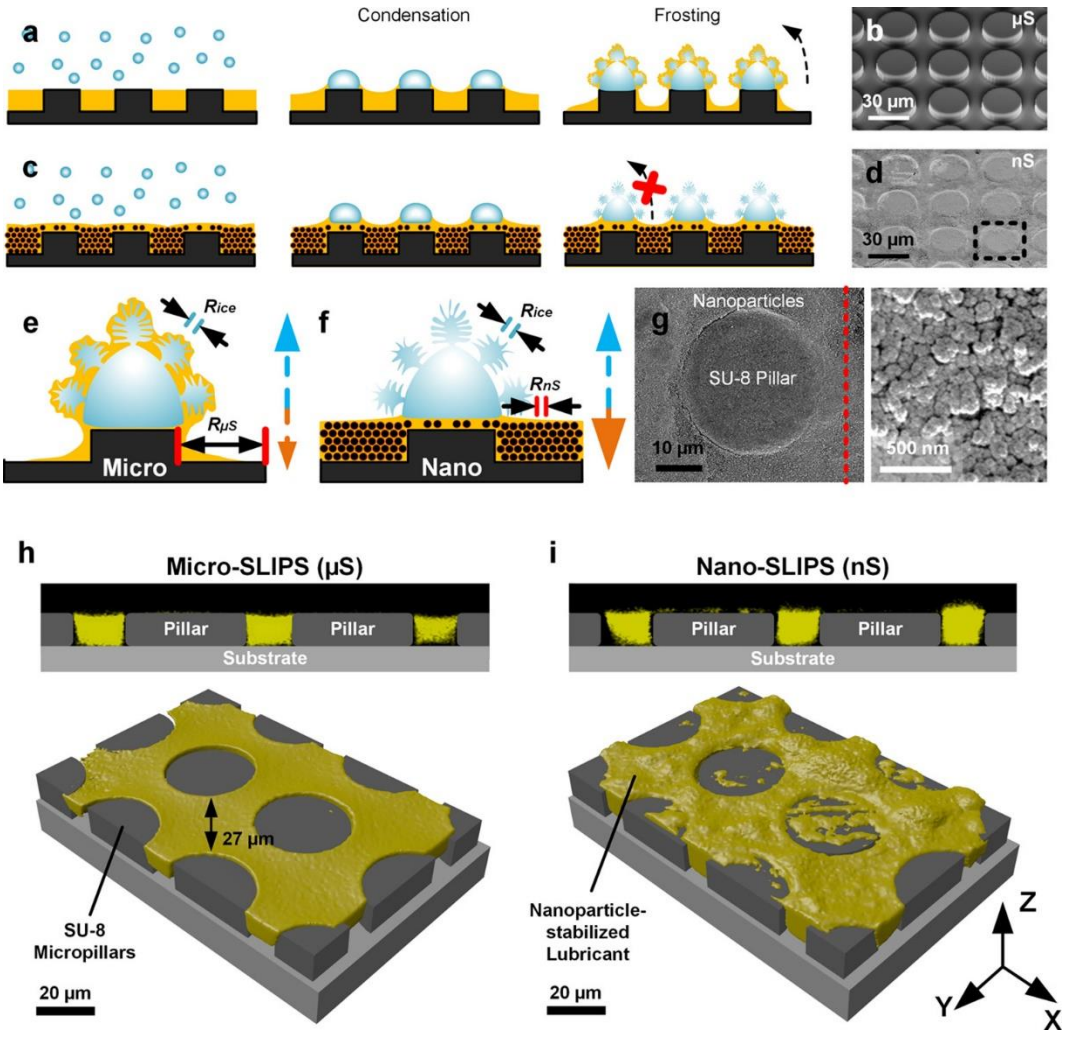

Figure 5.1. Capillary balancing. SU-8 micropillar arrays are used as invariant visualization markers: They have a height of 10 μm and a diameter of 30 μm. The pitch distance is 40 μm. (a) Sketch of condensation and frost formation on (b) micropillar arrays (Micro-SLIPS, 18 μm, μS, SEM micrograph) resulting in drainage of lubricant from the surface due to strong capillary forces. (c) Sketch of condensation and frost formation on (d) lubricant-infused micropillar arrays filled with nanoparticles (Nano-SLIPS, 30 nm, nS, SEM micrograph). The capillary pressure exerted by nanointerstices keeps lubricants in place. (e) Sketch of capillary balancing: Micro-SLIPS (18 μm) experience strong capillary-induced drainage because of the interstitial spacing R_{ice} imposed by frost-geometries, which falls below those between pillars $R_{ice} < R_{\mu S}$. (f) Capillary-balanced Nano-SLIPS (30 nm, nS) impede capillary-induced drainage by frost R_{ice} due to retentive capillary forces imposed by nanointerstices R_{nS}. (g) Magnified SEM micrograph of one SU-8 micropillar surrounded by nanoparticles. The nanoparticles and associated interstices are indicated by a representative cross-sectional cut on the right (red dashed line). A high-resolution three-dimensional confocal microscopy image of (h) Micro-SLIPS (18 μm, μS) and (i) Nano-SLIPS (30 nm, nS) under ambient conditions. The yellow color represents the fluorescence from the dyed (Lumogen Red 300, 0.1 mg/mL) lubricant (silicone oil, 200 cSt). The pillars and base substrate are inserted as augmented reality, fitted to experimental confocal surface maps using Blender.

Infusion of the micropillars and the nanoparticle-infused micropillars with silicone oil (Sigma-Aldrich, Silicone oil AR 200, 200 cSt) results in the upper (μS) and lower limits (nS) of Micro-SLIPS (18 μm, μS) and Nano-SLIPS (30 nm, nS) respectively. The silicone oil possesses a glass transition temperature of about −90 °C, Figure 5.7. Therefore, we expect significant increase of the viscosity and decrease in fluidity of the silicone oil when approaching the glass transition temperature. The design of Nano-SLIPS (30 nm, nS) is based on our concept of capillary balancing (Figure 5.1e,f). In contrast to Micro-SLIPS (18 μm, μS, Figure 5.1e), the smaller length scales in a nanostructured filler provide much stronger capillary retentive forces, thus preventing lubricant depletion during frosting (Figure 5.1f). R_{ice} was experimentally measured down to about 100−400 nm (Supporting Information, Movie M1), that is, $R_{nS} < R_{ice} < R_{\mu S}$.

We monitored the height and reorganization of lubricant for Micro-SLIPS (18 μm, μS) and Nano-SLIPS (30 nm, nS) using a custom-built laser scanning confocal microscopy (LSCM) setup under a variety of frosting conditions. The 3D reconstructions are obtained from the fluorescence signal of the silicone oil (Methods).[214] The oil-air interface is noticeably smoother in Micro-SLIPS (18 μm, μS, Figure 5.1h) as compared to Nano-SLIPS (30 nm, nS, Figure 5.1i). Here, the micropillars allow for comparative visualization of frosting and depletion dynamics with pillars as location markers (fixed boundary conditions). In situ frosting was performed in a custom-built frosting chamber (Figure 5.8). The chamber (0.24 L) is inverted, and condensation-frosting is imaged directly from the side facing the objective (about 2−3 mm working distance). The SLIPS variants were mounted on a cooling element with a set-point temperature of between 20 °C to −100 °C. Depending on the set-point temperature, the surface temperature might be a few degrees higher (Figure 5.7). If not stated otherwise, all temperatures refer to the set-point temperature. Gas lines deliver dry or wet nitrogen gas into the chamber at 20 °C, 6 L min^{-1}. To induce frosting, surfaces are cooled down to the set-point temperature under constant dry nitrogen purge and equilibrated for 5 min. Thereafter, a premixed wet nitrogen stream (about 60 % RH) is delivered into the chamber for 30 s. The chamber is then sealed as condensation-frosting commences and chamber humidity drops. Confocal microscopy imaging of the surface is performed in parallel, providing in situ temporal observations of dynamic processes. This protocol avoids severe frost densification, thus preventing optical scattering of fluorescence. Observation of lubricant reorganization in micropillar arrays is possible despite closer objective-to-frost proximity.

To understand the effect of capillary balancing in dynamic lubricant depletion, we used a low magnification objective (10×/NA0.40), complemented with a high-magnification objective (100x/NA0.80). The 10× objective allows for high temporal-resolution intensity analysis (Figure 5.9).

Alternatively, the 100× objective's depth-sensitive numerical aperture allows us to monitor and analyze depletion dynamics in 3D. We mapped the fluorescence and reflection signals with time. As the pillars' tops are facing toward the objective, depletion can be monitored at a vertical resolution of about 1 μm and a horizontal resolution of 0.2 μm. Macroscopic top-down static images (10× objective) of lubricant (yellow) on Micro-SLIPS (18 μm, μS) are presented on the left and Nano-SLIPS (30 nm, nS) on the right (Figure 5.2). The analysis is typically performed within interstitial sites (Figure 5.2a,c,e, red squares, Figure 5.10) between pillars to provide additional micro microscopic intuition behind frosting-induced lubricant reorganization.

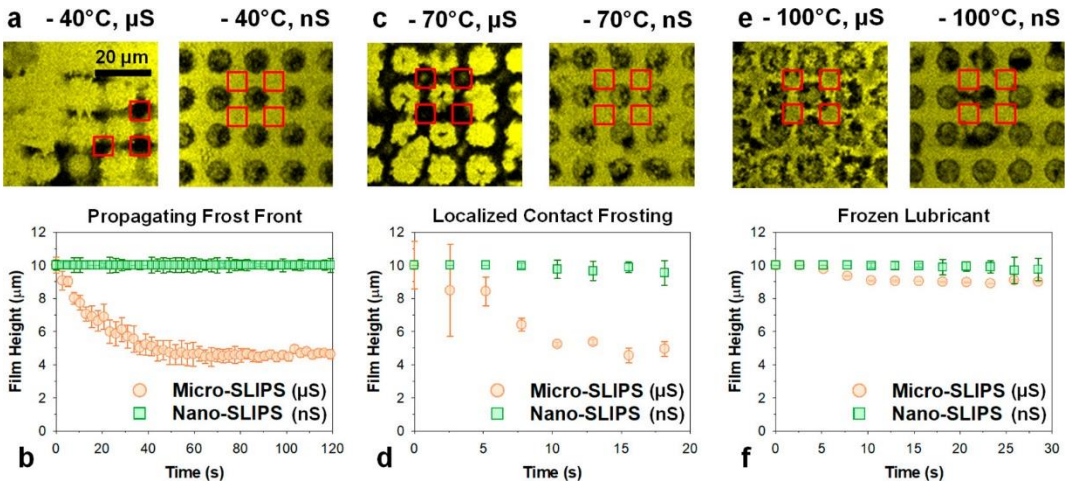

Figure 5.2. Fluorescence signal (lubricant) of confocal microscopy images of Micro-SLIPS (18 μm, μS) and capillary-balanced Nano-SLIPS (30 nm, nS) under moderate to extreme frosting conditions. (a,c,e) At exposure time, t = 100 s. Top view (XY) images of the frosting behavior, 10× objective. Left panels depict Micro-SLIPS (18 μm, μS) while the right panels depict Nano-SLIPS (30 nm, nS). Different frosting conditions: (a) frost front propagation-induced frosting (−20 °C to −40 °C); (c) localized contact frosting (−50 °C to −70 °C); and (e) thermal reorganization of frozen lubricant (−80 °C to −100 °C). The dark circles show the top faces of the micropillars which are easily observed in Nano-SLIPS (30 nm, nS) even after frost formation. Black grid lines between micropillars are lubricant-depleted zones (a,c). (e) Small black irregular regions may depict frost crystals which have grown out of the focal plane. Quantitative dynamic drainage of Micro-SLIPS (18 μm, μS) and Nano-SLIPS (30 nm, nS) at (b) −40 °C, (d) −70 °C, and (f) −100 °C, 100× objective. Location of analysis is always performed on the largest interstitial sites; lubricant heights are averages over the representative area marked in red-colored squares.

We observe the following three dominant modes of frosting and lubricant reorganization: (1) propagating frost front (−20 °C to −40 °C), (2) localized contact frosting with the formation of frost crowns (−50 °C to −70 °C), and (3) thermal reorganization of frozen lubricants due to latent-heat effects (−80 °C to −100 °C). For conciseness, we discuss the −40 °C, −70 °C, and −100 °C states as representative of these respective modes (Figures 5.9 and 5.11 for different temperatures).

At −20 °C to −40 °C, we observe that frosting is triggered by nucleation at a random spot. Frost spreads outward from these spots in a quasi-circular front that sweeps over the entire observable domain (Movie M2). On Micro-SLIPS (18 μm, μS), the frost front moved at a velocity of about 8 ± 1 μm s^{-1}, forming frost dendrites that suck lubricant (yellow) up into the frost structures as they form (Figure 5.2a, μS). This partially empties the large lubricant-filled interstices surrounding the frost (Figure 5.2b and Figures 5.9 to 5.11). After frost growth and propagation stops, no further lubricant is absorbed and the film height stabilizes. Note that as soon as the chamber's relative humidity drops below about 5−10 % (temperature-sensitive), frosting stops (Supporting Information, Table 6). Measurement errors result from frost propagation-induced spatial shifts (inhomogeneities) in frosting and lubricant depletion.

In contrast to Micro-SLIPS (18 μm, μS), the lubricant height in the capillary-balanced Nano-SLIPS (30 nm, nS) stayed at about 10 μm throughout the frosting process (despite frost growth, Movie M2). This demonstrates an innate stability of the nanoparticle-stabilized lubricant layer (Figure 5.2a,b and Figures 5.9 and 5.11). At the set-points of −50 °C to −70 °C, the substrate surface is well below −39 °C (Figure 5.2c,d and Figure 5.7). This is the critical temperature at which contacting water vapor freezes immediately, regardless of surface-based nucleation sites.[215] On Micro-SLIPS (18 μm, μS) at −70 °C, frost forms around each pillar, giving rise to crownlike domains surrounding each pillar (Figure 5.2c, μS and Movie M3). This results in a rapid drainage of lubricant in its local vicinity (Figure 5.2d, circles). The completion of drainage occurred in just about 10 s of exposure, alongside a decrease of lubricant height by about 6 μm. As contact frosting is highly localized, the time scale of depletion in this temperature range is significantly faster compared to depletion at higher temperatures. The experiment was not evaluated beyond 20 s due to frost densification that reduces optical contrast for high temporal scan resolutions. Once again, capillary-balanced Nano-SLIPS (30 nm, nS) demonstrate a lubricant layer that is largely stable within the same time (Figure 5.2d, squares) and temperature domain (Figures 5.9 and 5.11). At even colder temperatures, we reach the domain where the lubricant begins to freeze/solidify (set-point of −80 °C to −100 °C). The lubricant is completely frozen at set points of −90 °C to −100 °C (Figure 5.2e, Figure 5.11 and Movie M4). With Micro-SLIPS (18 μm, μS) at −100 °C, the lubricant height still decreased by about 2 μm during frosting after a small time delay (10 s) although the lubricant should be frozen (Figure 5.2f, circles). This might be caused by the localized melting and reorganization of solidified lubricant, as latent heat is released from the condensation and frosting of water.

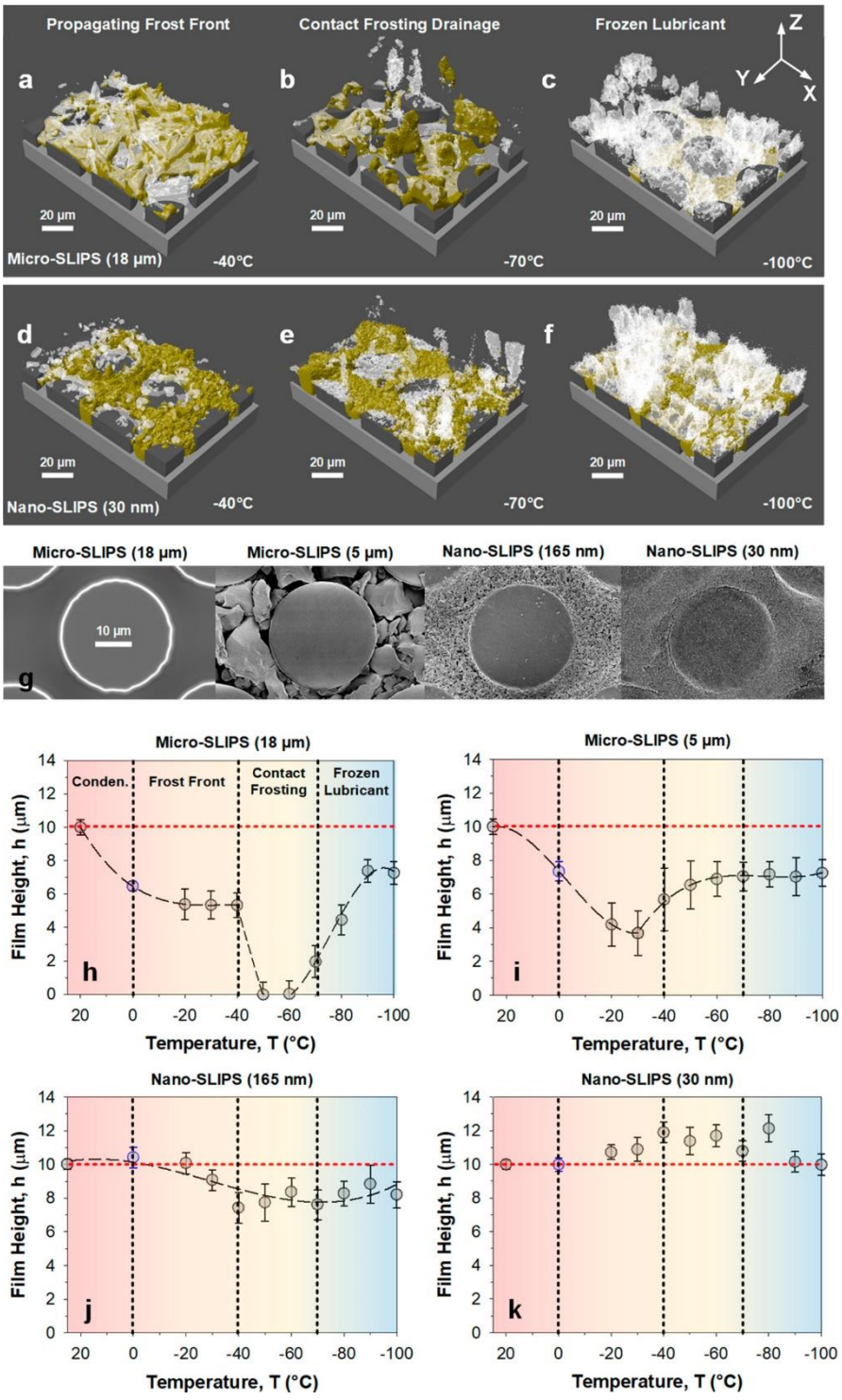

Figure 5.3. Three-dimensional confocal microscopy imaging for frosting-induced drainage under equilibrium conditions (exposure time, t = 5 min, 100× objective). Micro-SLIPS (18 μm) when exposed to (a) −40 °C, resulting in frost front depletion, (b) −70 °C, contact frosting depletion, and (c) −100 °C, thermal reorganization of molten lubricant. The translucent white surface layer is processed confocal microscopy data, via data from the reflection channel. For Nano-SLIPS (30 nm), the same exposure conditions at (d−f) −40 °C to −100 °C did not appear to induce frosting-induced drainage. (g) In Micro-SLIPS (18 μm), the interstitial spacing varies between 10−27 μm

(g, first panel). Depletion occurs almost immediately, even during condensation (second blue data point, h). Depletion increases with lower temperatures until they deplete completely between (h) −50 °C to −70 °C. When adding (i) microparticles ($D_{\mu S,mean}$ of 5 μm), the interstitial spacing varies between 0−10 μm. It is zero when particles touch, (g, second panel). (j) For larger nanoparticles ($D_{nS,mean}$ of 165 nm), the interstitial spacing varies between 0−400 nm (g, third panel). For Micro-SLIPS (5 μm) and Nano-SLIPs (165 nm), depletion is noticeably reduced. Lubricant depletion was maximum between −30 °C to −40 °C (about 5 μm) for the former and between −40 °C to −70 °C (about 3 μm) for the latter. Even after the addition of micro- or nanometer-sized particles, interstitial spacing remains too large to prevent lubricant drainage by frost dendrites. The dashed lines serve to guide the eye. (k) For Nano-SLIPS (30 nm) with an interstitial spacing of between 0−60 nm (g, fourth panel), they appear to resist depletion with an undepleted base height throughout experiments. The lubricant, silicone oil (yellow) was dyed with Lumogen Red 300 at 0.1 mg mL^{-1}.

As before, the measurement was terminated after 30 s of exposure due to frost densification, as the underlying lubricant-infused micropillar array becomes obscured. The capillary-balanced lubricant layer in Nano-SLIPS (30 nm, nS) remained stable within the same time domain (Figure 5.2f, squares).

As frost densification obscures the direct observation of lubricants and height measurement after 20−30 s of exposure under ultracold temperatures (−50 °C to −100 °C), detailed information at equilibrium remains unknown. Nonetheless, the final state of frosting and lubricant depletion can still be obtained by performing high-resolution 3D scans (50 μm height, 0.25 μm resolution, 32-line scans, Figure 5.3). The 3D reconstructions of the overlaid reflection (translucent white) and fluorescence (yellow) channels are then coupled to an augmented array of micropillars (gray) for visualization (Figure 5.12). Note: The reflection signal represents a frosted ice layer if no fluorescence signals are overlapping. It is also important to acknowledge that fine frost structures may cause scattering.

Frost on Micro-SLIPS (18 μm). At −40 °C, frost dendrites (about 2−3 μm layer) have a rodlike shape and a diameter of 1.9 ± 0.5 μm (Figure 5.3a and Figure 5.13). Notably, even the uppermost parts of the frost dendrites are covered in lubricants. At −70 °C, frost appeared to be agglomerate-like with submicron features. The submicron frost features efficiently soaked lubricants up to about 20−30 μm above pillar tops, deep into the frost layer (Figure 5.3b and Figure 5.13). At −100 °C, these submicron features persisted (Figure 5.3c and Figure 5.13). The frost is porous and dendritic, Movie M1.

Fluorescence signals within the micrometric interstitial spacing ($D_{\mu S,mean}$ = 18 μm, Figure 5.3g, first panel) are analyzed as equilibrium heights. Lubricant depletion occurs immediately upon condensation (Figure 5.3h, blue symbol at 0 °C). This is attributed to the formation of wetting ridges around condensed droplets.[216] Between −20 °C to −40 °C, the propagation of a frost front results in partial depletion of lubricant within the interstices (Figure 5.3h and Figure 5.1h, orange domain). Some lubricant is left in the interstices between the micropillars (gray areas). Depending on the exact location chosen for analysis,

the degree of depletion may differ. The improved height and intensity resolution of these so-termed equilibrium scans reveal that lubricant heights in the interstices decrease to near-zero at temperatures between −40 °C to −70 °C (Figure 5.3h, yellow domain). At even colder temperatures of between −70 °C to −100 °C, the degree of depletion decreases, due to a semifrozen lubricant layer. However, a slightly depleted height of about 8 μm ± 1 μm is still detectable (Figure 5.3c,h). This decrease in lubricant height within pillars' interstices hints of a latent heat effect during frosting, which induces localized melting and reorganization of the frozen lubricant (Supporting Information).

Scaling Micro-SLIPS to Nano-SLIPS. To provide a description of scale, variations of both Micro-SLIPS and Nano-SLIPS were designed using different filler microparticles (Figure 5.3g, second panel) and nanoparticles (Figure 5.3g, third panel), respectively. The resulting range of interstitial spacings are between 0−10 μm and 0−400 nm, respectively. Interstitial spacings were determined by thresholding and 500 sampling circle fits using ImageJ. It appears that the supplementary use of micro- to nanoscale particles promotes lubricant retention with smaller interstices (Figure 5.3i,j). However, the maximum extent of drainage in these variants: Micro-SLIPS (5 μm) and Nano-SLIPS (165 nm), remains significant (about 3−6 μm). Nonetheless, drainage is still notably reduced compared to Micro-SLIPS (18 μm). Lubricant drainage reaches about 6 μm between −20 °C to −40 °C for Micro-SLIPS (5 μm) and about 3 μm between −40 °C to −70 °C for Nano-SLIPS (165 nm). With a further decrease in temperatures, we noted reduced extents of depletion, likely because of increasing lubricant viscosity when approaching the glass transition temperature (−90 °C). Lubricant heights reach a final steady value of about 7−9 μm at −100 °C. This improved lubricant retention behavior is likely caused by the partial success (Figure 5.3i,j and Figure 5.14) of capillary balancing, relevant at nanometer length scales.

Frost on Nano-SLIPS (30 nm). First, frost morphology differs slightly at warmer temperatures (compared to aforementioned SLIPS variants). At −40 °C, the frost appears to be significantly more spherical or cuboidal in shape, at diameters of 4.1 ± 0.9 μm (Figure 5.3d and Figure 5.13). Below −40 °C, frost appears agglomerate-like with submicron features, which persists even at −100 °C within a similar length scale (Figure 5.3e,f and Figure 5.13). Frost was also detected up to a height of 30 μm above pillar tops. At all exposure temperatures, pillar tops remain free of lubricant and the interstices between pillars remain filled with lubricant. These results showcase the core discovery: Dense nanostructuring is required for capillary balancing (interstitial spacing of 0−60 nm). Hierarchical surfaces should not work due to the presence of large microinterstices where lubricant can be drained. High capillary retention requires surfaces that possess only densely spaced geometries with nanointerstices. On Nano-SLIPS

(30 nm), we did not observe lubricant drainage after the condensation of water droplets (Figure 5.3k, blue data point). Notably, throughout the entire temperature range (−20 °C to −100 °C), no lubricant depletion within the bulk phase was observed within experimental resolution. At a few locations, some lubricant was observed at 1−2 μm above its initial height. This small increase was predominantly found from −40 °C to −80 °C (Figure 5.3k). Lower temperatures have been observed to lead to finer frost crystals and potentially higher capillary suction. Therefore, tiny amounts of excess lubricant (after infusion) that are not nanointerstitially retained may be easily drawn into the frost. This excess lubricant was not removed post synthesis (i.e., by washing) as the Micro-SLIPS and Nano-SLIPS configurations were treated identically to ensure a fair comparison. While minor traces of excess lubricant are likely a primary cause for our observations, the possibility of cloaking is also discussed (Supporting Information, Lubricant-Cloaked Frost Ice).

Influence of Frosting on Ice Adhesion Behavior. We now question what consequences frosting and capillary balancing have on icing and deicing in SLIPS (Figure 5.4). Essentially, icing rarely occurs independently from frosting. To quantify ice adhesion strength, Micro-SLIPS (18 μm, μS) and Nano-SLIPS (30 nm, nS) were enclosed in an icing chamber kept at −10 °C. Upon equilibrium, a small drop of water (10 μL) is deposited on its surface and allowed to freeze (Figure 5.4a). Frost halos[217]

Micro-SLIPS (18 μm, μS, Figure 5.4b, orange squares) experience a gradual rise in ice adhesion. This rise originates from a gradual depletion of lubricant volume, as confirmed by confocal microscopy (Figure 5.4b, depletion inset). Occasional large errors in force measurements were caused by contact-shear damage of the pillars, leading to a lubricant depleted zone with direct ice contact and very high ice adhesion (Figure 5.4b, damage inset). After 50 cycles, ice adhesion strength leveled off. Micro-SLIPS (18 μm, μS) were almost completely drained of lubricant by the 50th cycle (Figure 5.4c).

In contrast, Nano-SLIPS (30 nm, nS) experience a consistently low ice adhesion (<30 kPa) even after 50 deicing cycles (Figure 5.4b, green circles) with no noticeable loss of lubricant (Figure 5.4d). However, adhesion did increase from about 2−18 kPa by the 10th cycle. This may be caused by removal of tiny amounts of excess lubricant and excess nanoparticle agglomerates (i.e., tops of pillars) originating from sample preparation. By the 10th cycle, the originally rough pristine nanoparticle-infused lubricant domains are now notably smoother (Figure 5.4d). In contrast to Micro-SLIPS (18 μm, μS), the integration of densely packed nanoparticles within the micropillar arrays may have also enhanced the overall mechanical stability. Therefore, the lubricant layer in Nano-SLIPS (30 nm, nS) remains stable and functional (30 ± 10 kPa) even after 50 cycles (Figure 5.4d).

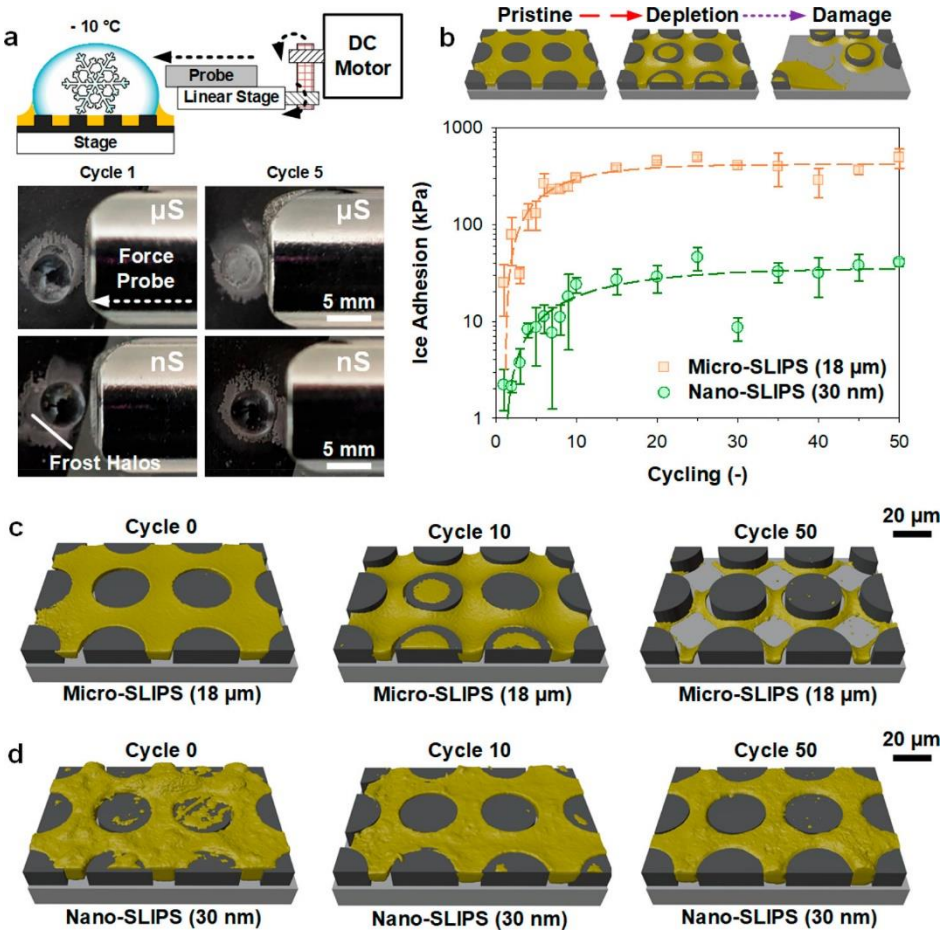

Figure 5.4. Influence of freezing and associated drainage dynamics on anti-icing adhesion performance. (a) A custom-built setup was designed for ice adhesion measurements at −10 °C. Water drops of 10 μL (diameter of about 0.6 cm) were deposited on surfaces: Micro-SLIPS (18 μm, μS, top panels) and Nano-SLIPS (30 nm, nS, bottom panels) and frozen. Thereafter, a force probe (sensitivity of 0.01 N, contact point: 0.5 mm above the surface) is driven toward the ice drop at about 30 μm s-1 until the ice drops are detached. The continuous force curves were collected and the peak forces measured. (b) The capillary-balanced Nano-SLIPS (30 nm, nS) variants kept their excellent low surface adhesion (N) per unit area (m2) to ice drops during cyclic testing (<20 kPa) up to 10th cycle and equilibrated at about 30 kPa by the 50th cycle. (c,d) Notably, near-complete lubricant depletion occurred for (c) Micro-SLIPS (18 μm, μS) as compared to a nearly unaffected lubricant layer for (d) Nano-SLIPS (30 nm, nS). By the 10−50th cycles, Nano-SLIPS (30 nm, nS) appear to be significantly more uniform as compared to the pristine version. This is attributed to the direct removal of inhomogeneous asperities during ice shear and removal.

5.3 Conclusion

The severe problem of lubricant depletion in SLIPS during frosting and icing can be prevented if the interstitial spacing of the infused surface is smaller than that between frost dendrites. To avoid capillary-suction induced depletion, the design principle of "capillary balancing" needs to be followed: All nanointerstitial spacing needs to be lesser than those found in frost dendrites. If not, lubricant depletion can be reduced but not avoided. Dense packing of small nanoparticles (in the order of 10 nm) creates effective nanoscale interstitial spacing. Densified nanostructured packing is shown to preserve performance even after multiple traverse shear icing−deicing cycles. After 10 cycles, ice adhesion per unit area remains as low as 12 ± 4 kPa and levels off at 30 kPa after 50 cycles. In contrast, the microstructured variation reaches an ice adhesion of 500 kPa after 50 cycles. The design principle of capillary balancing allows for the development of frost-resistant, durable anti-icing lubricant-infused surfaces that may survive extreme terrestrial (−20 °C to −70 °C) and even extra-terrestrial environments (< −70 °C).

5.4 Methods

Terminology. All SLIPS surfaces synthesized are defined by the mean ± standard deviation (where possible) of their respective interstitial spacing, i.e. Micro-SLIPS (18 μm), Micro-SLIPS (5 ± 5 μm), Nano-SLIPS (165 ± 90 nm), and Nano-SLIPS (30 ± 20 nm). For conciseness within the manuscript, surfaces are predominantly labeled with their respective means. The limits of Micro-SLIPS (18 μm) and Nano-SLIPS (30 ± 20 nm) are also referred to as μS and nS respectively.

Fabrication of Microstructured SLIPS (Micro-SLIPS, interstitial spacing: 18 μm). Micro-SLIPS (18 μm) was synthesized by coating an epoxy based SU-8 photoresist (SU-8 5, MicroChem) on a thin cover slip (170 μm thick). The SU-8 film was cured into a structured array pattern of micropillars (pillar diameter: d = 30 μm; center to center distance: l = 40 μm; height: h = 10 μm), utilizing photolithography, Figure 5.5a. After UV-exposure (8 s) using a height: h = 10 μm photomask and baking cycles at 65 °C (30 min), 95 °C (3 min) and 65 °C (30 min), the uncured SU-8 was dissolved in a developer solution and washed in propanol. The rigid micropillar array was then plasma cleaned and infused with 1 μL cm^{-2} of lubricant per substrate area.

Fabrication of Nanostructured SLIPS (Nano-SLIPS, interstitial spacing: 30 nm). Nano-SLIPS (30 nm) has a micropillar base that is identical to that of Micro-SLIPS (18 μm) (Figure 5.5b-c). From here, a nanoparticle filler was synthesized (Figure 5.1d). The nanoparticle filler comprises of two components, an -epoxy terminated variant and an -amine terminated variant. Fumed silica nanoparticles (Aldrich, 7 nm, 395 $m^2 g^{-1}$) were functionalized with an amine-terminated end (amine, Part I) or a glycidyl-terminated end (epoxy, Part II). The -epoxy terminated variant was synthesized by a methoxy-based sol-gel method, by stirring 1 g of fumed silica (Aldrich, 7 nm) in 50 mL of deionized water and 2.6 mL of (3-Glycidyloxypropyl)trimethoxysilane (Aldrich, 99.9 %) at 500 rpm, 20 °C, 72 hours. The -amine-terminated variant was synthesized by an ethoxy-based sol-gel method, by stirring 1 g of fumed silica (Aldrich, 7 nm) in 50 mL of toluene (200 ppm water) and 2.8 mL of aminopropyltriethoxysilane (Aldrich, 99.9 %) at 500 rpm in a round-bottom flask, under reflux at 80 °C for 72 hours. Both surface grafting recipes were designed in excess (30 μmol m^{-2}). Both colloidal solutions are then centrifuged at 10000 rpm for 10 minutes and washed in their respective solvents (50 mL) for 3 cycles before being dried in a vacuum oven (50 mbar, 60 °C) overnight. Thermogravimetric analysis indicates that nanoparticles are functionalized to ca. 10 w/w% in both instances (-amine and -epoxy variants). This results in an average grafting density of

ca. 0.75 ± 0.1 chains nm^{-2} in each variant respectively (Supporting Information, Figure 5.5). Once dried, the nanoparticles are re-suspended in acetone (25 mg mL^{-1}) before spray-coating, by stirring both powders at approximately 1000 rpm using a Teflon-coated stir bar for 1 hour. This is followed by sonication for another hour. As the functionalization density is almost identical in both -epoxy and -amine-functionalized nanoparticles, both dispersions are mixed together in a 1:1 v/v ratio (i.e. 2 mL + 2 mL) for 30 s. The total loading of 4 mL (100 mg of mixed particles) is then immediately sprayed (2-3 bars, at 0.2 mL s^{-1}) from a distance of 7.5 cm onto a SU-8 pillar coated cover slip (6 cm x 1 cm area). To form a covalently bonded epoxy-amine nano-silica network, the coating is left to cure for at least 48 hours. The nanoparticle coating hardens over this period, forming a dense nanoparticulate layer (Figure 5.5b,e). However, the nanoparticles not only fill up the gaps between the pillars but also cover the pillar tops (Figure 5.1b). To remove the particles from the pillar tops, the surface needs to be polished. The over-coated particles are removed by surface abrasion with a nitrile glove. After rubbing for up to a minute, the particles above the top surfaces are removed (Figure 5.5c,e). Notably, one cannot physically remove the entrapped nanoparticles below the maximum pillar heights owing to the physical proximity of protective pillars. Analysis of the nanometric spacing between the nanoparticles revealed an average distance of 30 nm (Figure 5.6). However, spacings below 20 nm could barely be resolved, and likely exists. The larger spacing dominates our interpretation of the average interstitial sizing. The composite micropillar array was then plasma cleaned and infused with 1 μL cm^{-2} of lubricant per substrate area.

Tuning Micro-SLIPS to Nano-SLIPS. To provide additional size variation of the packing particles, we functionalized silica-based microparticles (diameter 5-10 μm) and nanoparticles (diameter 500 nm) under the same conditions as described before (identical w/w ratio) to maintain identical surface chemistry. Thereafter, we deposited them using the same technique (re-suspension in acetone (25 mg mL^{-1}), spray-coating, polishing, and oil infusion). The resulting variations are listed with their interstitial spacing, as Micro-SLIPS (5 μm) and Nano-SLIPS (165 nm). In the former, owing to the fragmentation during deposition, irregular microparticles were formed. Samples were then mounted in the custom-built confocal-frosting chamber, and exposed to the same test conditions for the measurement of the lubricant layer's equilibrium stability.

Lubricant and Dye. For the lubricant, a silicone oil (polyphenyl-methylsiloxane, Sigma Aldrich AR 200; surface tension, γ = 20 mN m^{-1}, 200 cSt) was used. A fluorescence marker (Lumogen Red F300, BASF, excitation at 532 nm, emission at 610 nm) was added to the silicone oil. To enhance the solubility of the

fluorescence dye in silicone oil, the dye was initially dissolved in chloroform (Chloroform, 99.8+ %, Fisher Chemical). The dye-chloroform concentration was diluted down to 0.1 mg mL^{-1} and ultra-sonicated for 1 min. The dye-chloroform solution was then mixed with silicone oil such that an eventual Lumogen Red-silicone oil concentration of 0.1 mg mL^{-1} was achieved (1:1 solvent exchange). The mixture was stirred for an additional 5 minutes. To remove remaining chloroform, the mixture was exposed to 40 °C and 50 mbar for 24 h under vacuum-assisted evaporation. We did not observe changes in interfacial tension nor an accumulation of the dye at the interfaces. The close refractive index matching of the chemically modified nanoparticles (approximately 1.45) and silicone oil (1.41) enables the 3D visualization of the lubricant.

Humidity and Temperature Control. To control the temperature of the targeted SLIPS samples, a custom-built setup was designed, Figure 5.7. Samples are mounted on a cooling element (Linkam) within a frosting chamber (volume: 240 ml). The cooling element is closed loop controlled within a temperature range of -196 °C to 600 °C, capable of a cooling rate of up to 100 K min^{-1}. To control the chamber's humidity, two nitrogen gas lines are used: One is water vapor enriched (humidified) while the other comprises of dry nitrogen gas. We utilized a water-bubbler system to enrich the first gas line with water. The sample is then cooled down alongside the continuous purging of the chamber using the dry stream at 2 L min^{-1}. The temperature was kept at the desired set-point for 2 min to achieve equilibration (typically within 1 minute). Thereafter, the flow rate of the humidified gas line was set to 2 L min^{-1}. Both lines are then directed into a mixing stream. The mixed stream is introduced into the frosting chamber for 30 s before the frosting chamber is sealed. This stream results in an influx of a bulk vapor phase peaking at ca. 40 % relative humidity, at 20 °C ambient (thus inducing frost formation on the cold stage). Condensation-frosting on the cooled surface decreases chamber humidity after sealing the chamber. In this work, a range of datasets (10 °C increments) was collected from -20 °C to -100 °C set points. The actual substrate surface temperature was also measured independently using a flat PT-100 (2 mm x 2 mm) sensor (Figure 5.14). Minor reorganization occurs during cooling for the Micro- SLIPS series, in contrast to the relative invariance for Nano-SLIPS series (Movie M5). Additional datasets were also obtained from ambient (20 °C) and a condensing (but not frosting) environment (set point at 0 °C). 3 experiments were performed for all measurements that follow to ensure repeatability of the phenomena, unless otherwise stated.

Laser Scanning Confocal Microscopy. The experiments were monitored with a custom-built, inverted Laser Scanning Confocal Microscope (LSCM), with an inverted frosting chamber. The microscope has two

illuminating lasers (*Cobolt DLC™ 25*; wavelength: blue 473 nm; green 532 nm. Power: 25 mW). The laser beam is directed into a magnifying objective lens onto the sample surfaces. The objective lens (dry; *OLYMPUS UPIanSApo* 10x/0.40; *OLYMPUS LMPIanFLN* 100x/0.80) of the microscope is mounted on a piezo-controlled stage that translates the sample within a domain of up to 200 μm in the vertical direction. The horizontal plane is sampled with a counter rotation scanner (*Cambridge Technology, 215H Optical Scanner*) which sweeps with a sampling rate of 7910 ± 15 Hz in one direction. The microscope is controlled with a custom LabVIEW program. Three distinctive modes of capturing were utilized: three dimensional horizontal plane (XYt), four-dimensional (XYZt) and three-dimensional (XYZ) scans, where t stands for time. XYt (line accumulation: 32) was performed at a plane of view of within an effective 730 μm x 180 μm depth of view of 8.5 μm (*OLYMPUS UPIanSApo* 10x/0.40). Objective-to-surface distance is typically 2-3 mm. This prevents the influence of thermal mass on the surface and condensation/frosting on the objective. The large spacing ensured unhindered flow of humid air between the lubricant-infused surfaces and the objectives. This spatial configuration allowed a recording frequency of 2 fps. XYZt and XYZ were performed at a plane of view of 146 μm x 73 μm within an effective depth of view of ca. 0.5 μm (*OLYMPUS LMPIanFLN* 100x/0.80). The scanning height was 20 μm and XYZt measurements were performed at a line accumulation of 4 and a height resolution of 1 μm. For high resolution images, the scanning height was 50 μm and the XYZ measurements were taken using a line accumulation of 32 and a height resolution of 0.25 μm. These configurations allowed a recording frequency of 0.39 fps or one frame per 2.59 s in the former scheme and 0.005 fps for the high-resolution settings. The latter was only used for quasi-equilibrium states. The lasers are used at the maximum capacity of 25 mW each. The incident photons on the sample reflect off the upper layer of the samples' surfaces. The combined reflection-fluorescence modes enable the identification and distinction between the reorganized lubricant bulk and the corresponding frost geometries that are formed. Notably, readers should be advised that overlapping reflection-fluorescence signals may not depict actual frost features. However, reflection signals in the absence of fluorescence can be interpreted as frost. Although, absence of reflection does not imply the absence of frost because the light might be scattered in all directions and not back into the objective.

Fluorescence Intensity Analysis. To provide a macroscopic mapping of lubricant drainage, we perform an intensity analysis on the XYt plane, having a field of view of 730 μm x 180 μm and a depth of view of 8.5 μm (NA 10x/0.40). Although this depth of view is slightly below the pillar height, it allows for the qualitative mapping of the depletion of lubricant from the wells and channels between pillars during frosting. Raw data files were used without further processing, first by splitting channels using ImageJ.

Thereafter, the fluorescence channel was loaded into a custom-script in MATLAB which analyzes an area intensity defined by the user (i.e. the wells between pillars). A total of at least 100 sampling data points were analyzed and averaged. The intensity is typically mapped between values of 1 to 255. This intensity is mapped up to 5 minutes, at 2 fps. The intensity is then normalized within a scale of 0-100 %, where the minimum was determined from a quasi-dry location within wells by the end of the experiment under the most lubricant-depleted conditions (-50 °C to -70 °C). Both Micro-SLIPS (18 μm) and Nano-SLIPS (30 nm) experiments are analyzed together to provide adequate normalization and appropriate comparison of the latter (minimal intensity variations).

Static Height Extraction. At frosting equilibrium (5 minutes after the onset of exposure), high-resolution XYZ images were extracted using a line accumulation: 32, height resolution of 0.25 μm over a range of 50 μm. This particular mode enabled the combined usage of both reflection-and-fluorescence mode of the confocal microscope (Figure 5.11). The reflection mode is able to qualitatively map the geometries of ice that were not flooded with lubricant while the fluorescence mode is able to map the locations of fluorescent lubricant. The raw data is processed via ImageJ by optimizing brightness/contrast (B/C), performing a mean 3D of 6 pixels to fill in empty data cells and a final threshold that converts the entire surface bulk into thin interfaces (oil-air, oil-substrate). The variable settings are fixed for each experimental set (i.e. temperature variation: B/C at 3-20, threshold at 169-202). This processed data is then analyzed using the 3D viewer in ImageJ to ensure realistic accuracy. The final images are then processed using a custom- script in MATLAB that maps the top interface (oil-air) and bottom interface (oil-substrate) interfaces using images that are converted into binary (surface plots). This layer of oil that is sandwiched between the two interfaces is then analyzed at 2 representative wells centrically between 8 different pillars (Figure 5.11). These wells are analyzed both circumferentially (radial data point selection) and a grid square (cartesian data point selection). Both domains are outlined by around 60 sampling data points each, totaling 120 locations. Care was taken to avoid 1) uneven nanoparticle surfaces, 2) densified frost, and 3) pillars. These selected domains are then averaged and normalized across the realistic height of the actual well (10 μm) from the pristine state (at ambient 20 °C) and computed across different condensation and frosting conditions. Images that are analyzed with MATLAB using this algorithm are also processed using an ImageJ algorithm (Gaussian Blur at 0.2 μm) before they are exported as representative reflection and fluorescence surface plots (.obj files using ImageJ) into Blender (Figure 5.11), where predefined pillar arrays are then superimposed into the surface signals. The fluorescence channel is artificially represented as yellow (oil) while the reflection channel is artificially represented as a textured translucent white (ice).

Dynamic Height Extraction. The XYZt dynamic height images are captured with a lower signal intensity (line accumulation: 4) due to requirements in temporal resolution, and thus required slightly different post-processing in ImageJ. Maximum thresholds and signal capture were performed by a B/C of 0-1 and 1-255 respectively. Thereafter, a mean 3D of 6 pixels was performed before a secondary threshold of 100-160 was used to capture the top and bottom interfaces. A custom MATLAB script was then used to process the heights of the lubricant interfaces. This reconstructs the spatial distribution of the lubricant film. As before, the lubricant height h is also measured in the space centrically in between the micropillars. The field of observation allows a collection of 128 sampling points which are then averaged.

Frost Analysis. The length scale of frost was analyzed by ImageJ, where the reflection channel of ultra-cold formed frost (without lubricant) at -100 °C was used. At -100 °C the frost is most dendritic, i.e. the length scales are smallest and represents the upper limit. Thus, capillary suction pressure is maximal and can be used as a limit. The reflection channel was processed through an initial auto brightness/contrast, followed by an auto thresholding at several 1 μm slices, over an area of 10,658 μm^2. Thereafter, noise was removed using the ImageJ's despeckle algorithm. Images were then analyzed using ImageJ's BoneJ > Surface Area analysis algorithm[218] in order to map the surface area and volumetric fraction of the frost. Results are summarized in surface area to volume ratios: $\mu m^2\ \mu m^{-3}$. Confocal resolution is known to have a spatial limit of around 200 nm, which was also confirmed by the analysis of the smallest length scales detectable.

Traverse Ice-Shear Adhesion Analysis. The in-air (-10 °C) water drop adhesion analysis is performed using a cooled chamber (Mobicool FR60), at -10 °C. Samples were fixed onto a height-adjustable stage and cooled for at least 30 minutes before commencing experiments. Every cycle consists of placing a water drop (10 μL) on the surface followed by further cooling for ca. 1 minute before freezing was triggered. At -10 °C, time-delay of freezing can take hours. To induce freezing under the most identical conditions, freezing was triggered by using contact with fine frost crystals (i.e. contact nucleation[219]). Contact nucleation does not alter the overall shape of the drop. More importantly: the footprint of the drop is kept constant, increasing the accuracy of the measurement of the area-specific force ($N\ m^{-2}$). Each iced drop is then imaged to verify the contact area (Board camera, Sony IMX 179), assuming spherical contact. Thereafter, a force sensor (PCE-DFG N 20, PCE Instruments GmbH), attached to a probe is engaged. The probe moves at ca. 30 $\mu m\ s^{-1}$ toward the drop via a motorized stage (custom-modified Thorlabs linear stage). The probe contacts the ice drop at approximately 0.5 mm above the surface. The ice drops have a contact area of ca. $28 \pm 2\ mm^2$. 3 drop locations were used throughout the cycling process, while

reporting the average ± standard error. Up to 50 cycles were performed until the ice adhesion strength leveled off. During probing, contact results in an increased force.

5.5 Supporting Information

5.5.1 Supplementary Discussions

Lubricant-Cloaked Frost Ice. We observe an increase in lubricant heights for Nano-SLIPS (30 nm) from -40 °C to -100 °C Dominantly, this results from excess lubricant during the infiltration step. This lubricant can be easily sucked up because it is poorly retained by the capillary pressure of the nanointerstices. At lower temperatures, the frost becomes highly dendritic, resulting in stronger capillary suction. Consequentially, this excess lubricant is sucked up into the frost-to-lubricant interface (3 µm). However, this process can be barely discriminated from the formation of lubricant-wetted frost. Close observation of the fluorescence channel show that lubricant wicks onto the frost without breaking away from the base layer. The lubricant does not travel deep into the dendritic frost structure, partially due to the lack of excess lubricants.

To gauge the influence of lubricant-wetted frost from cloaking, we estimate the volume of required lubricant. Therefore, we compute the surface area to volume ratio of the 3D confocal reconstructions from the frost at a set-point temperature of -100°C, utilizing ImageJ's plugin BoneJ and its associated algorithms. We analyzed -100 °C, because the frost at this temperature is most dendritic, i.e. the total surface area is at a maximum. A spherical approximation was used for frost geometries. This provides a surface area to volume ratio $r = \frac{4\pi R^2}{\left(\frac{4}{3}\right)\pi R^3}$ of ca. r = 7.5 µm^2 µm^{-3} to r = 30 µm^2 µm^{-3}. R is the effective radius of neighboring dendrites. The effective radius of neighboring ice dendrites was computed within the limits of 100 to 400 nm, which coincides with high-quality 3D confocal microscopy images of the frost (Movie M1). These results are also similar to previous studies on surface areas and volume fractions exhibited by ultra-fine snow/frost geometries.[220]

$$R = \frac{3}{r} \tag{19}$$

Next, we estimate the thickness of the lubricant layer to find the volume of lubricant contributing to this wetting process. The frost-air interface is likely cloaked with lubricant. For a stable layer of lubricant that does not soak into the frost, the disjoining pressure of the thin wetting film (on frost) must balance

the Laplace pressure exerted by the curved lubricant film cloaking the ice geometries (R). This balance stabilizes the cloaked layer at equilibrium,

$$\frac{A_H}{6\pi\delta^3} = \frac{2\gamma}{R} \tag{20}$$

$$\delta^3 = \frac{A_H R}{12\pi\gamma} \tag{21}$$

where A_H is the Hamaker constant, and δ is the thickness of the thin film coating the frost. The Hamaker constants, A_H, is at a maximum of 10-18 J, likely lower.[214] The size of frost R should be thus between 100 to 1000 nm. Inserting these limits into Eq. 21, leads to a lubricant film on frost, thickness δ of maximum 10 nm (A_H = 10-18 J, R = 1000 nm). Assuming a maximum frost height of 2 μm (maximum in situ observable drainage), a net volumetric loss of just r * 10nm * 3 μm ≈ 0.1 μm^3 in lubricants occurs per geometric area of 1 μm^2. Considering an originally stabilized lubricant layer of 10 μm in height, this represents a height loss of just 0.1 μm (1 % loss). Therefore, this explains why such losses (stemming from excess lubricants) often goes unnoticed, and capillary-balanced bulk lubricant layers always appear to remain invariant despite interface wetting of frost dendrites. Moreover, if lubricant-wetted frost is allowed to remelt and dry on the nanostructured slippery surfaces, the lubricant from the cloak will be reabsorbed back into the nanostructured surface.

Mobility of Lubricant in Micro-SLIPS at Ultra-Low Temperatures. At the set-points of -80°C to -100°C we observe minute lubrication reorganization in Micro-SLIPS (18 μm) although the lubricant (silicone oil) should be frozen (Figure 5.3) (See Movie M5). This minute reorganization of lubricant could be induced by phase-change (freezing of lubricants) as solid crystals are formed. Severe lubricant reorganization (drop of 20 % in intensity) occurs predominantly during exposure to the warm humid air (20°C, 40 % RH) during the first 30 s. Condensation and freezing releases heat, which might melt the solidified lubricant. For reference, the latent heat of condensation and fusion is at 2264 kJ kg^{-1} and 334 kJ kg^{-1} respectively. The heat capacity of frost ice and silicone oil is at 2.1 kJ kg^{-1} K^{-1} and 1.5 kJ kg^{-1} K^{-1} respectively. While the latent heat of fusion of silicone oil varies, it scales exponentially with melting temperatures. At an assumed maximum melting point of 60 °C, via Trouton's rule (negligible hydrogen bonding), latent heat of fusion scales between 1 to 10 kJ mol^{-1} at M_w of ca. 11000 g or 0.1 to 1 kJ kg^{-1}. As a result, the condensation-frosting should, qualitatively be expected to result in releasing sufficient heat to heat/melt frozen silicone oil. Excess heat is eventually absorbed by the cooling element.

5.5.2 Supplementary Figures

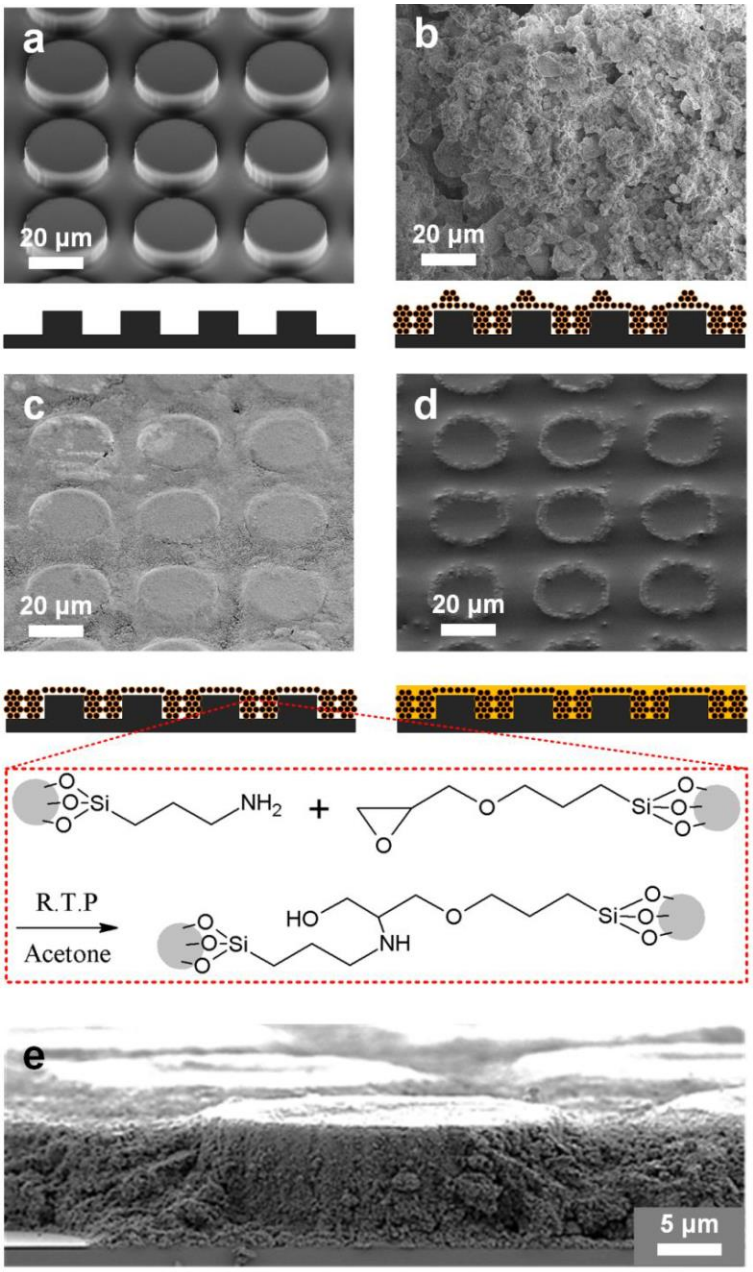

Figure 5.5. Synthesis of Nano-SLIPS (30 nm). a) UV-photolithography for regular microstructures, b) coating of nanoparticle layers, c) polished nanoparticle-infused microstructures, d) lubricant-infused nanoparticle-microstructures (ionic liquid was used for visualization). e) A nanoparticle bed of covalently bonded epoxy-amine nano-silica is proposed as the source for capillary balancing.

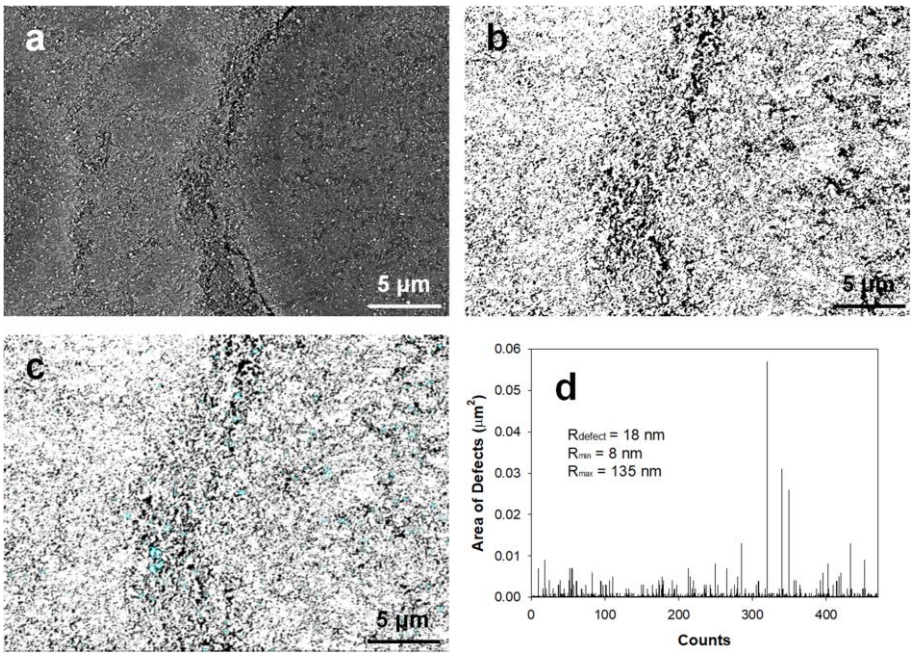

Figure 5.6. ImageJ mapping analysis of the size of interstices in the nanoparticle bed (Nano-SLIPS, 30 nm). a) Scanning electron microscope image of a nanoparticle layer wrapped-pillar. b) Re-contrasting and binary image that shows dominate holes (represented by dark regions). c) ImageJ's particle analyzer without spherical limitations (0 to 1), which provides a d) size distribution of interstices (assumed radial dimensions R), at an average of 15 nm (non-normal distribution) with a minimum of 8 nm (detection limit) and a sporadic maximum of up to 135 nm. However, the distribution of larger pore sizes drops off sharply from 60 nm (Figure 5.14). These results were correlated and confirmed using high resolution (high magnification) side-profile SEMs (See Figure 5.1).

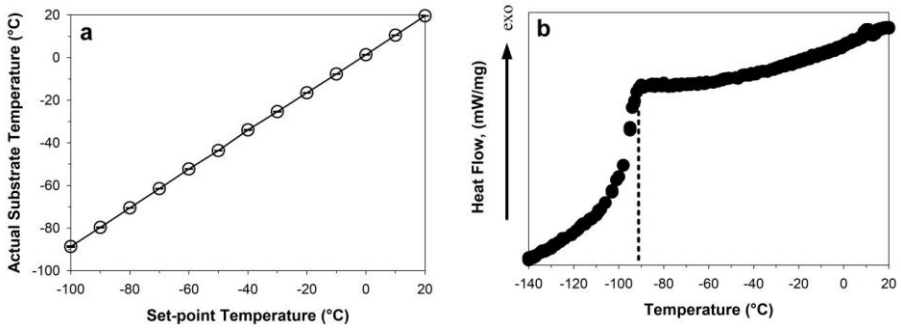

Figure 5.7. Temperature scale within the system. a) "Actual substrate temperature" vs. "Setpoint temperature" on the Linkam stage (Peltier element). Chamber: 0 % relative humidity, 20 °C ambient. Temperatures measured after 1-2 minutes of equilibration (per experimental conditions). b) Differential scanning calorimetry (DSC) measurements on pristine silicone oil (AR 200), showing a gradual change in heat flow from room temperature down to ca. -90 °C, i.e. when approaching the glass transition temperature. The gradients observed before and after the glass transition are caused by temperature-dependent heat capacities.

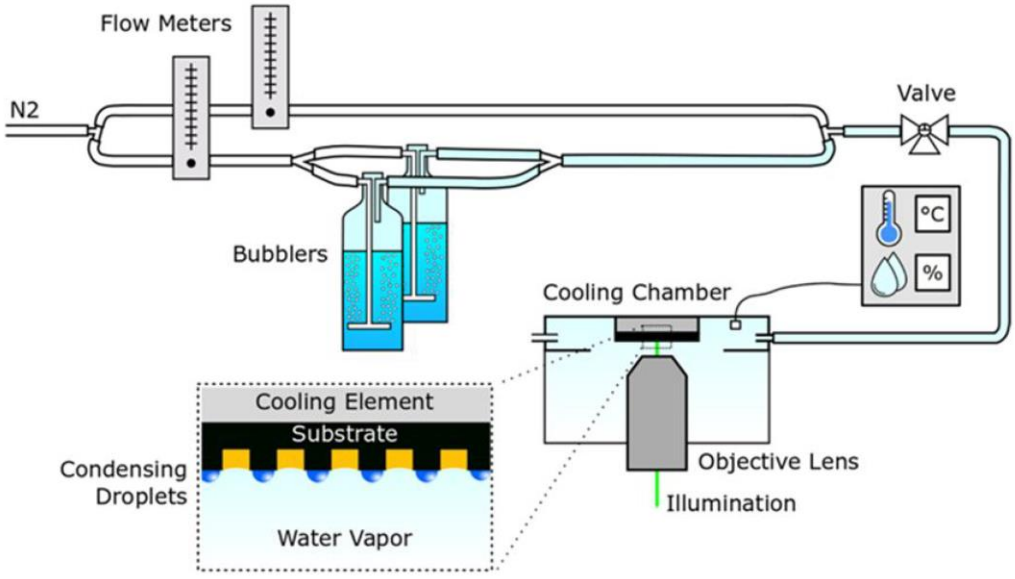

Figure 5.8. Custom-built confocal-frosting set-up. Frosting is induced by using a stream of warmer, wet humid nitrogen stream (40 % RH, 20 C).

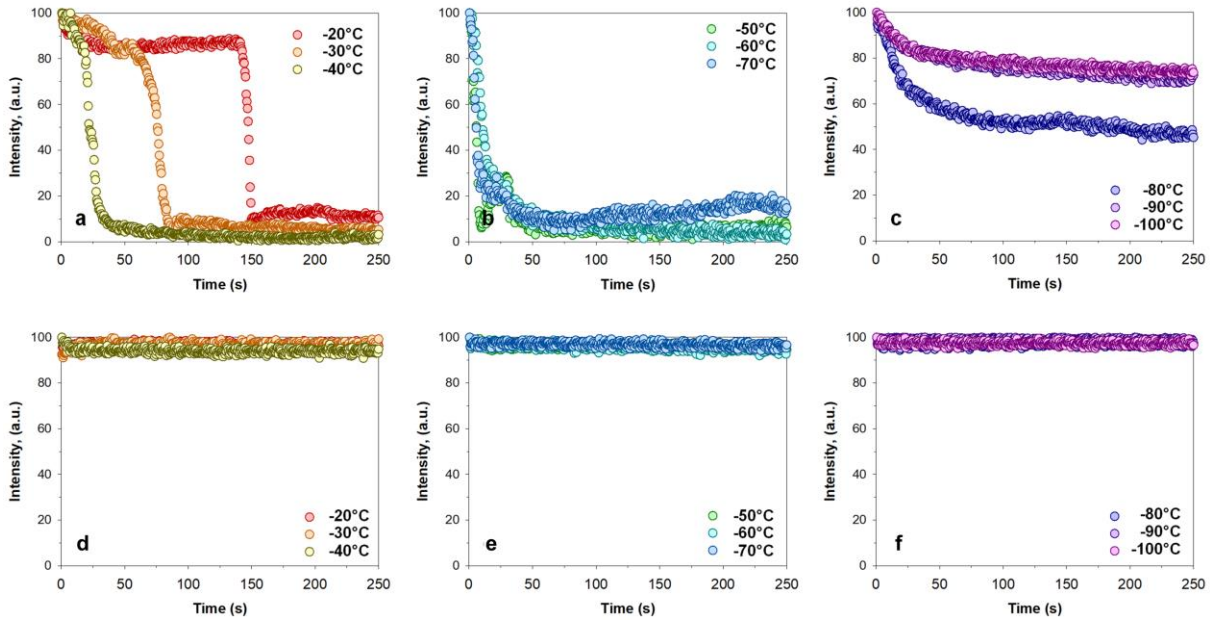

Figure 5.9. Macroscopic qualitative analysis of drainage using fluorescence-intensity. At the start of the experiment the intensity was defined to be maximum, i.e. 100 %. The focal plane was zeroed to the top surface of the pillars. Intensity measurements experience a depth of view of only around 8.5 µm. Therefore the loss of lubricant from the domain of observation results in the complete loss of intensity (-100 %). Analysis of drainage in a-c) Micro-SLIPS (18 µm) and d-f) Nano-SLIPs (30 nm) under the a,c) frost front propagation domain (-20 °C to -40 °C), b,e) contacting frosting domain (-50 °C to -70 °C), c,f) frozen lubricant domains (-80 °C to -100 °C). a) Macroscopically, it appears that the time-delay required for nucleation-induced frosting decreases with temperature. During this time-delay, minor drops (10-15 %) in fluorescence intensities were noted. Frosting-induced drainage dynamics appear to be identical once frosting begins, taking place between 10-20 s to decrease the fluorescence intensity in the larger targeted interstices: from an original 100 % to lower than 10 %. b) At -50 °C to -70 °C, lubricant depletion occurs immediately, regardless of the actual substrate temperature. c) The lubricant used (silicone oil) begins to freeze. d-f) For the capillary-balanced Nano-SLIPS (30 nm), the intensity remains constant. Intensity measurements should be regarded as a qualitative representation of the depletion phenomena as they are inherently non-linear due to the influence of the point-spread function on confocal imaging.

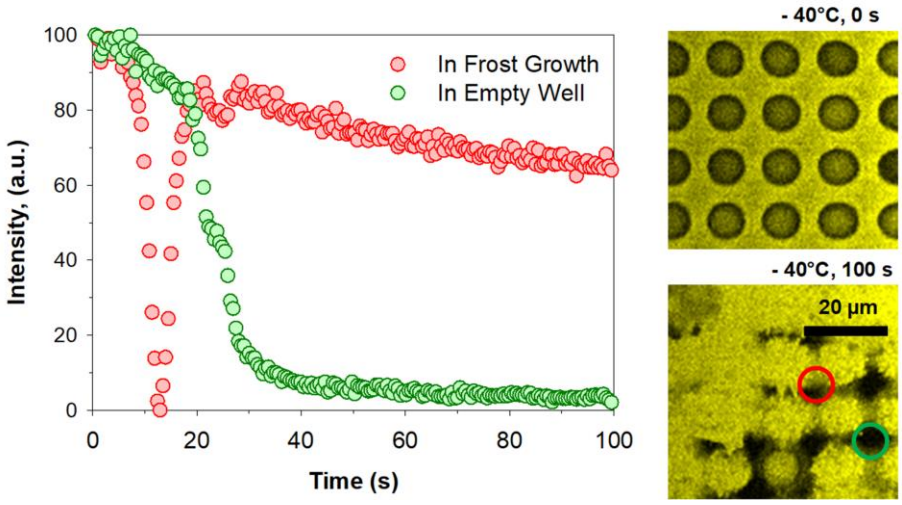

Figure 5.10. Macroscopic intensity imaging in the frost front domain of Micro-SLIPS (18 µm). Frost front drainage depends on the location. Some regions drain regularly (green location and data points) while other regions first rapidly drain due to the incoming frost front. Thereafter, the lubricant thickness can "increase" again as the lubricant-soaked frost grows above the dry zone (red location and red data points). The green locations are usually analyzed (final empty location at equilibrium) because these reveal the dynamic (albeit qualitative) thickness of the lubricant layer between pillars during depletion.

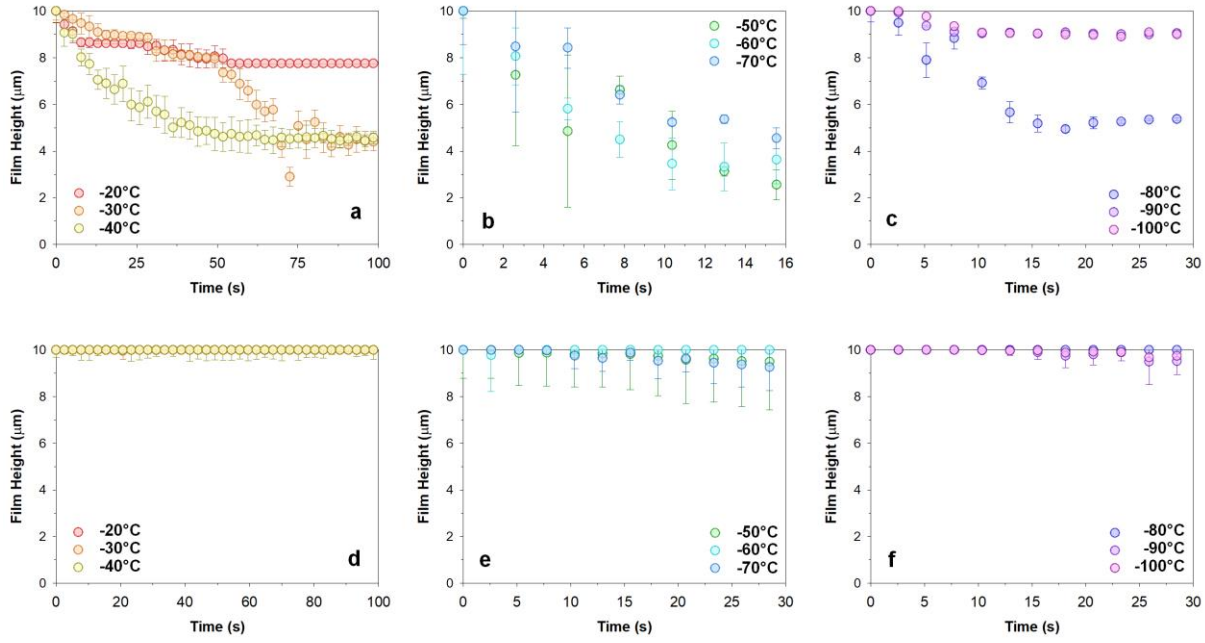

Figure 5.11. Height evaluation of frosting on Micro-SLIPS (18 µm) and Nano-SLIPS (30 nm). Quantitative dynamic drainage of a-c) Micro-SLIPS (18 µm) and d-f) Nano-SLIPS (30 nm) in pillar interstices at a,b) -20 °C to -40 °C, b,e) -50 °C to -70 °C and c,f) -80 °C to -100 °C. The minimum height of lubricants cannot be observed due to frost-growth densification. Densified frost scatters light. Optical resolution cannot be improved due to the as-required fast scanning speeds involved: Therefore, equilibrium states are supplemented using high resolution scans (Figure 5.3).

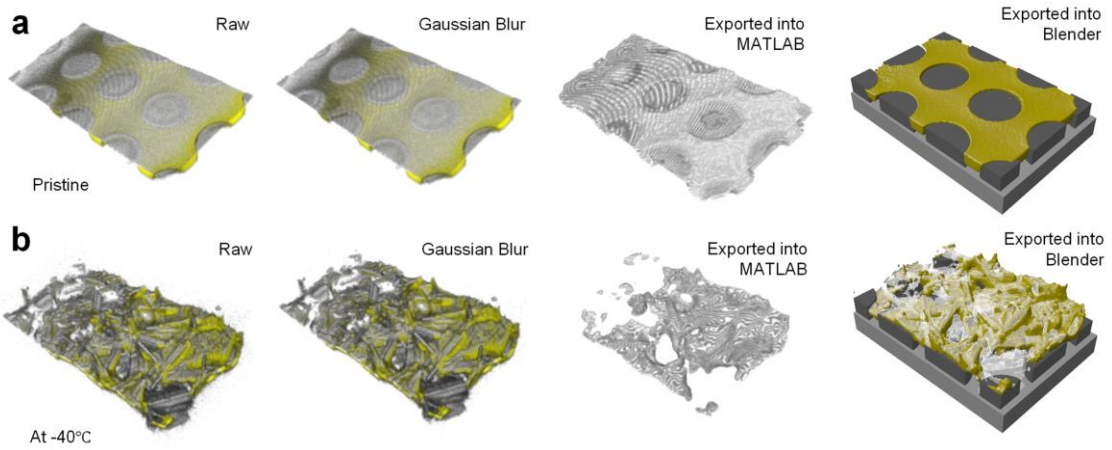

Figure 5.12. Image processing of raw data. a) Pristine state and b) Frosted state: Raw data obtained from confocal microscopy shows 2 layers, the reflection channel (grey) and the fluorescence channel (yellow). These are then processed using thresholding and a Gaussian blur algorithm which removes excessive noise in the images. Thereafter, the channels are split, and the florescence channel is exported into MATLAB for height analysis (dynamic / static drainage etc.). These split channels can also then be exported from ImageJ as 3D surface plots (.obj) into Blender, cropped and superimposed with known pillar dimensions (grey-black) to provide realistic experimental reconstructions. The reflection channel can be either a) removed, if ice is non-existent or b) given a translucent texture which provides hints of iced domains without lubricant (see foreground, first lubricant well).

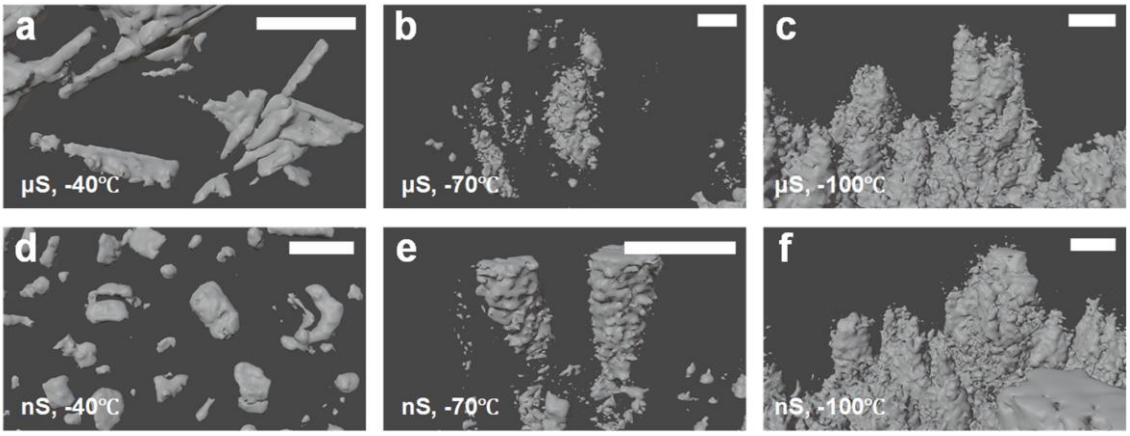

Figure 5.13. Isolated images of confocal-captured frost features. Frost geometries range from a) needle/rod-like (diameter = 1.3 ± 0.4 μm) at -40 °C on Micro-SLIPS (μS, 18 μm), or d) globular-like (diameter = 4 ± 1 μm) on Nano-SLIPS (nS, 30 nm), to b,c,e,f) fractal regular agglomerate-like at -100 °C on both Micro-SLIPS (μS, 18 μm) and Nano-SLIPS (nS, 30 nm). Fractal agglomerates are typically 5-10 μm in width, tree-like and comprises of sub-micrometer roughness. Scale bars are set at 10 μm in all images.

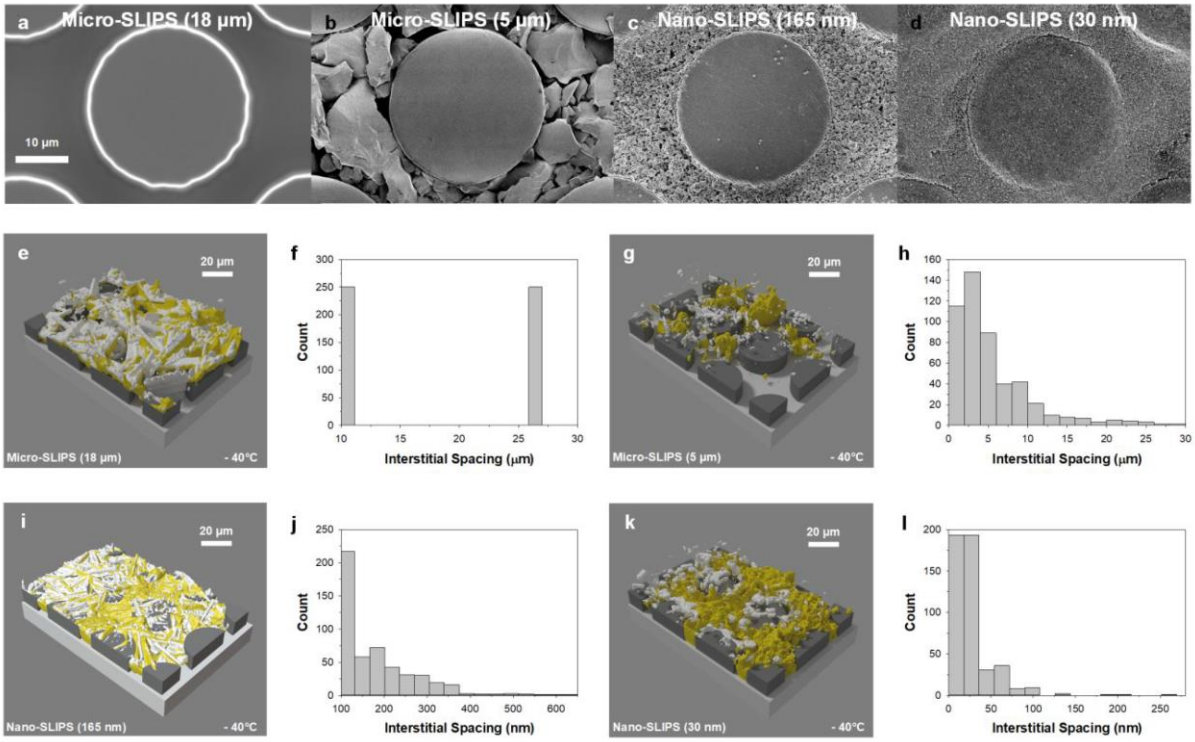

Figure 5.14. 3D confocal microscopy imaging for frosting-induced drainage under equilibrium conditions at -40 °C (exposure time, t = 5 min, 100x objective). e-f) Micro-SLIPS (18 μm), g-h) Micro-SLIPS (5 μm), i-j) Nano-SLIPS (165 nm), k-l) Nano-SLIPS (30 nm). Ice is colored plain white and the lubricant is colored yellow. The histograms were obtained using ImageJ, with thresholding and 500 sampling circle fits.

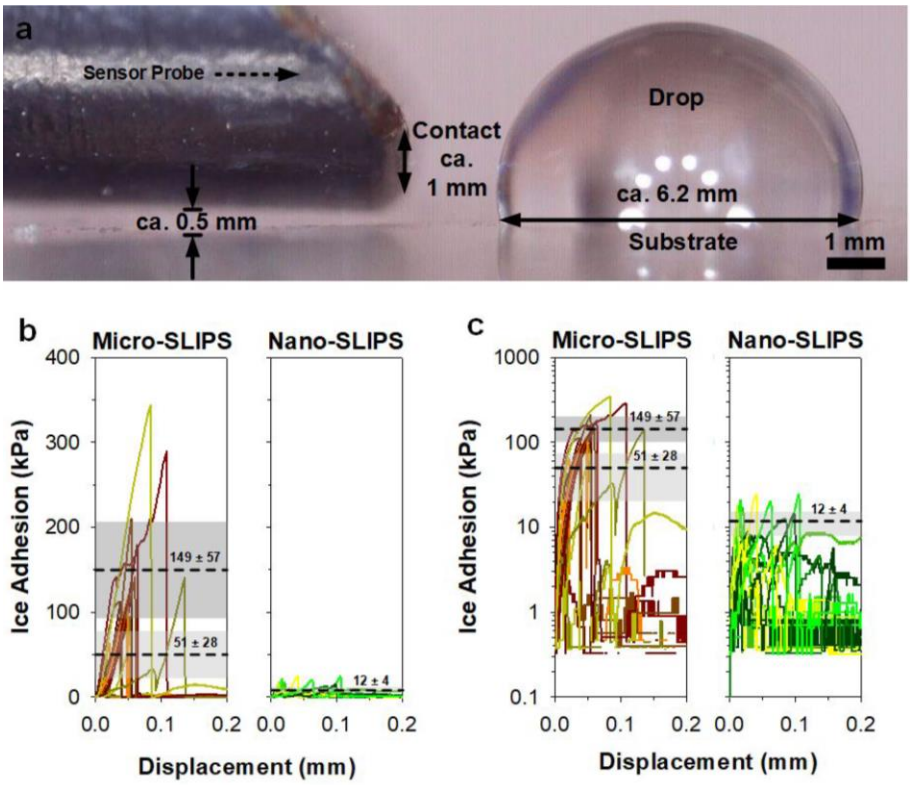

Figure 5.15. Compilation of geometry of probe-to-ice contact and ice adhesion force curves. a) Side-on imaging of probe-to-ice contact and the relevant scales of geometries. Probe is slightly out of focus as the width of the sensor is wider than the entire drop (an unfrozen drop was used for visualization). Ice drop (glaze) contact area is ca. 28 mm^2 collated from the first 10 representative cycles are presented in a) linear and b) semi-log. Left panel as Micro-SLIPS (18 µm) and right panel as Nano-SLIPS (30 nm). Grey zones: Average ± 1 standard deviation. Micro-SLIPS (18 µm): Light grey box represents the first 3 cycles, while darker grey box represents the next 7 cycles of peak force measurements. Nano-SLIPS (30 nm): Average of the first 10 cycles are comparatively stable within a log-scale and can be represented in a single domain, due to much greater performance stability.

Table 6. Equilibrium relative humidity in frosting chamber at designated set-points.

Set-point Temperature (°C)	*Equilibrium Relative Humidity (in Chamber) after frosting at ca. 20 °C (%)*
-20	9.7 ± 0.6
-30	9.0 ± 0.3
-40	8.2 ± 0.5
-50	6.6 ± 0.6
-60	6.3 ± 0.2
-70	5.3 ± 0.7
-80	5.3 ± 0.4
-90	5.1 ± 0.3
-100	4.9 ± 0.5

5.6 Author Contributions

W.S.Y.W. and K.I.H. fabricated the surfaces. W.S.Y.W. carried out the experiments and characterization unless otherwise stated below and wrote the manuscript. W.S.Y.W and K.I.H. performed scanning electron microscopy and discussed (with L.H.), confocal microscopy results. V.D. aided in supplementary confirmation experiments. W.S.Y.W. performed the image processing with L.H.'s consultation. All authors (particularly W.S.Y.W, L.H., A.N., and D.V.) discussed the mechanisms for understanding capillary balancing. W.S.Y.W. and D.V. contributed to experimental planning, data analysis, and manuscript preparation. All authors reviewed and approved the manuscript.

5.7 Acknowledgments

This work was supported by the European Union's Horizon 2020 research and innovation program LubISS No. 722497 (W.S.YW., A.N., V.D., D.V.), the German Research Foundation (DFG) with the Priority Program 2171 (L.H., D.V.), the Collaborative Research Center 1194 (L.H.), the Max Planck − Univ. Twente Center for Complex Fluid Dynamics (D.V.), and the Max Planck Graduate Center (K.I.H.). We thank M. D'Acunzi, H.-J. Butt, and P. Baumli for stimulating discussions and A. Sharifi for technical support.

6 Surface Topography as a Promising Tool to Tune Bacterial Adhesion

6.1 Introduction

The formation of biofilms affects a broad variety of industrial sectors, including transport infrastructure, the food industry, and medical devices. In the US, healthcare-associated infections linked with high morbidity affect about 10 % of patients.[221]

Due to the cooperative behavior of mature biofilms, they show a higher resilience toward removal by antibiotics or biocides.[111,222] Furthermore, the increasing resistance of bacteria toward antibiotics and environmental concerns regarding the large-scale use of biocides limit their application.[223,224]

Therefore, extensive research aims at developing surface modifications that reduce or eliminate bacterial attachment in the first place. The attachment of bacteria is governed by a wide range of factors, including physiochemical properties of the bacteria and surface properties such as surface chemistry, topography, and charge. Typical approaches to anti-bacterial surfaces rely on the inhibition of cell adhesion due to chemical modifications such as poly(ethylene glycol)[225,226] and functional polymer brushes[223]. However, chemical modifications may eventually be masked due to nonspecific protein adsorption or by surfactants secreted by bacteria.

Generally, bacteria are on the micrometer scale with surface appendages on the nanometer scale. Control of the nano- and micrometer surface topography could potentially play a pivotal role in inhibiting interactions between bacteria and surfaces over a long timescale.[227] So far, super-liquid-repellent[115], liquid-infused[118,228], and bactericidal[122,123,229–231] surfaces have been investigated.

Super-liquid-repellent surfaces have received particular attention. On the solid-air composite interface, the contact area available for bacterial attachment is greatly reduced (Figure 6.1a). However, with changes in pressure, temperature, or humidity, the liquid may transition to the Wenzel state.[232] As soon as the bacterial suspension wets the surface, an increased surface area is available for colonization and the anti-bacterial functionality is lost (Figure 6.1b). Therefore, super-liquid-repellent surfaces have not been successfully implemented as a long-term solution to biofouling.

Recently, Encinas et al. showed that a suitable three-dimensional surface topography can reduce bacterial adhesion even in the superhydrophilic state.[124] Experiments with *E. coli* and *M. luteus* on superhydrophobic and superhydrophilic silicone nanofilaments (SNF) showed similar anti-bacterial behavior. Presumably, the spacing of the fibrous three-dimensional structure falls just below the characteristic size of bacteria, effectively reducing the number of anchoring points and suppressing

bacterial adhesion in the wetted state (Figure 6.1c). The coating is applicable to a wide variety of materials and geometries, making them a promising candidate for application in medical devices.[125] A well-chosen three-dimensional topography presents a promising method for designing anti-bacterial surfaces: surfaces do not rely on the use of antibiotics, biocides, or low surface energy functionalization with fluoroalkyl substances, which expands possible applications in the medical field. Additionally, systems should be less susceptible to changes in the environment and therefore, show an increased lifetime.

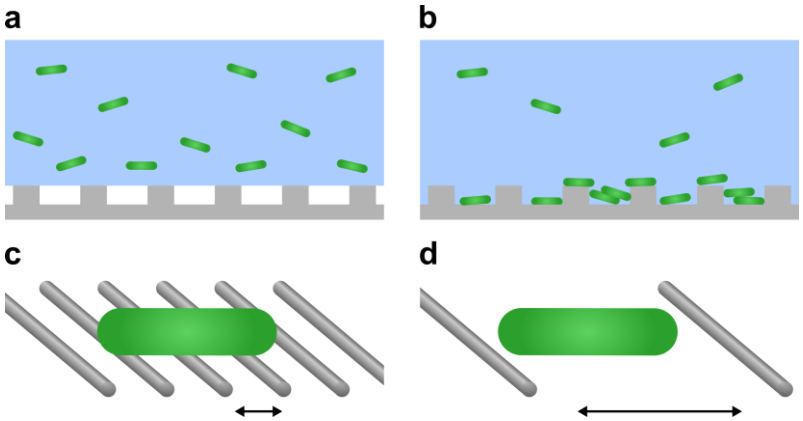

Figure 6.1. Scheme of a bacterial suspension (blue) on a low surface energy substrate in a) the Cassie and b) the Wenzel state. c) Bacteria contacting a surface with an appropriate submicrometer-sized topography. d) Bacteria contacting a surface where the surface features are spaced out too far.

The SNF synthesis requires prior activation of the underlying substrate to introduce surface hydroxyl-groups and solvent-immersion growth under controlled reaction conditions. Furthermore, tuning of the resulting surface features and reproducibility of the coatings can be challenging. LFS presents a promising alternative to produce easily scalable surfaces with an appropriate topography. As previously shown, the method allows precise control over the size and density of fractal-like aggregates of nanoparticles.

Tuning and optimization of the surface topography allow a deeper understanding of the relation between surface morphology and bacterial adhesion. Apart from a mere physical approach employing surface topography, chemical modifications can further enhance their anti-biofouling properties. Past research has shown that mechano-bactericidal high aspect ratio surfaces such as black silicon can deform and stretch microbial membranes and induce cell rupture.[122,231] Additionally, cell death can be induced via the introduction of photocatalytically active titanium[233] or antibacterial chemical functionalizations.[234]

Still, there are numerous unanswered questions concerning bacterial adhesion and the synthesis of anti-bacterial surfaces. In the light of rising multi-resistant bacteria strains, the design of surfaces that minimize bacterial attachment is an important issue.

6.2 Introducing Sub-Micrometer Roughness via Liquid Flame Spray

Here, a well-chosen surface topography as a generic approach to anti-bacterial surfaces will be explored. The feasibility of using LFS as a coating technique is investigated as it allows the structural optimization on the nano- and micrometer scale toward reduced bacterial adhesion. Thus, a variety of process parameters are varied: the precursor feed rate (tetraethoxysilane in isopropanol), the particle collection distance, and the number of passes of the substrate through the flame and the velocity thereof.

During experiments on bacterial adhesion, immense forces are acting on the surface structures. A quick test, where samples are wetted with water and thereafter left to dry shows, that as-received silicone dioxide particle films collapse during drying, resulting in the formation of densely packed, closed films. When particles produced via LFS are collected on a substrate outside of the hot zone of the flame, they form aggregates that are loosely connected, e.g. by van der Waals forces (Chapter 1.4.1). Highly porous structures on the nano- to micrometer scale are inherently mechanically weak, challenging their application. To improve the mechanical stability of the nanoparticle aggregates, a silica shell is added via chemical vapor deposition. By exposure of the surfaces to tetraethoxysilane and aqueous ammonia solution for 24 h, a silica layer with a thickness ranging from 20 to 35 nm is formed.[65] Afterward, the coatings are sintered at 500 °C for 3 h in air. The overall diameter of the resulting silicone dioxide particles is typically around 55 nm and therefore on the same scale as the diameters found for silicone nanofilaments. Apart from the size of the nano features, their aggregation into micrometer-scale aggregates is crucial. During the coating process, particles tend to aggregate into hierarchical micrometer-sized surface protrusions. However, a low micrometer scale roughness is required for anti-bacterial properties. To achieve comparatively closed films, the coatings need to be produced at small distances to the burner and with high precursor feed rates. Rough surface morphologies increase the surface area and the number of adhesion points for bacteria. Figure 6.2a presents a case where the surface area available for bacterial attachment is drastically increased. The LFS coating was produced using a precursor feed rate of 3 mL min^{-1}, at a distance to the burner of 90 mm. The sample passed the flame 4 times at a speed of 30 mm s^{-1}. Despite the addition of a silica shell and sintering at 500 °C for 3 h, the

coating partially destabilized over the course of the bacterial assay. Individual particles and particle aggregates can be observed on top of attached bacteria.

Figure 6.2b shows a coating with a more uniform surface morphology produced at a higher precursor feed rate of 5 mL min^{-1}. However, even on this coating, relatively large indentations with diameters of more than 1 µm can be discerned. These indentations present preferential attachment sites for bacteria that are of a similar size. Furthermore, mechanical instabilities can be observed: Figure 6.2c depicts a LFS coating produced at the same coating parameters. Here the coating collapsed during the experiment and formed a denser particle layer. Furthermore, the coatings are challenging to produce; increasing the precursor feed rate increases the size of the flame which oftentimes induced bursting of the substrate. For the same reason, the distance to the burner cannot be further reduced.

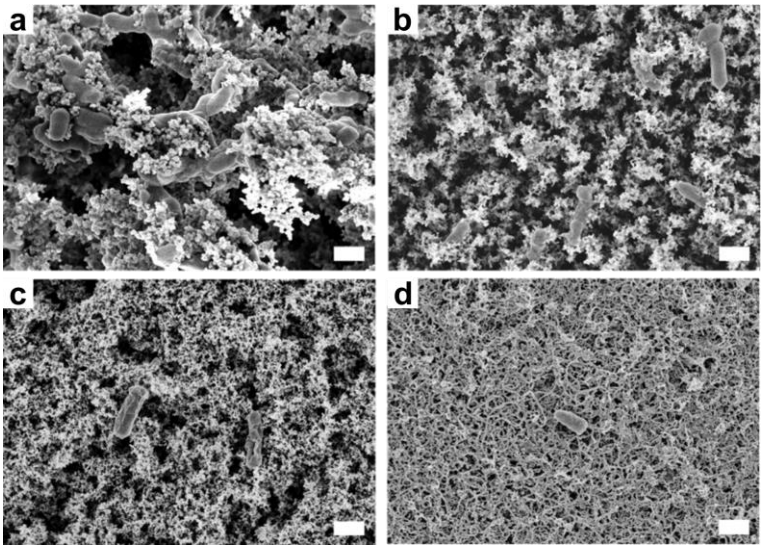

Figure 6.2. SEM images of bacterial attachment on a, b) LFS coatings prepared at different process conditions, c) a collapsed LFS coating, and d) SNF (scale bars are 1 µm). The more homogeneous the surface, the less bacteria attachment can be observed.

Generally, it was found that all LFS surfaces prepared at different process parameters exhibit a higher degree of bacterial attachment compared to SNF control surfaces. The SNF coating presents less distinctive surface protrusions and appears more homogeneous overall (Figure 6.2d). Even though LFS is a versatile coating method, so far, the process parameters could not be successfully tuned toward the fabrication of surfaces suitable for anti-biofouling in the wetted state.

7 Summary and Outlook

This thesis contributes to the understanding and fabrication of liquid-repellent and super-liquid-repellent surfaces, focusing on the vital role of surface topography. Optimization of the structures on the nano- and micrometer scale is crucial for the successful application of these surfaces.

LFS has proven a valuable technique for the production of various particle-based structures: depending on the chosen process conditions, the coatings may vary from a closely packed particle film to the formation of pronounced microscale features. Furthermore, the coatings can be applied to a range of substrate geometries, are highly reproducible, and allow upscaling.

For the application in bubble bursting and bulk defoaming, small nanoparticles aggregated into spaced-out, cone-shaped structures have shown superior results. The concept was applied to greatly enhance the separation efficiency in a froth flotation setup by defoaming in-situ generated foam. This additive-free, passive method is a promising alternative to the addition of oils or hydrophobic particles, conventionally used to prevent uncontrolled foaming.

Usually, super-liquid-repellency toward low surface tension liquids relies on the use of fluorinated hydrocarbons. Due to growing concerns toward fluorinated materials, novel fluorine-free super-liquid-repellent coatings are of high interest, specifically for applications in the food or medical sector. Here, two fundamentally different approaches toward low lateral drop adhesion are combined to circumvent the need for a fluoroalkyl-functionalization. A range of particle-based surfaces is functionalized with surface-tethered PDMS which is non-toxic, biocompatible, cheap, and has low surface tension. Indeed, water-ethanol solutions with a surface tension of only 31 mN m^{-1} can easily roll and bounce off surfaces with an optimized underlying structure. Experiments with different types of probe liquids reveal the effect of wetting-induced surface adaptation: increasing interactions with solvents and swelling of the PDMS chains cause drops to penetrate deeper into the structures. Despite having comparatively high surface tensions, liquids may remain pinned or even fully wet the surface. The limits of super-liquid-repellent surfaces are typically discussed in terms of the probe liquid's surface tension. Here, the results show that interactions between substrate and probe liquid and the associated changes in interfacial energy need to be considered in the design of super-liquid-repellent surfaces as well.

Another approach toward fluorine-free surfaces with low lateral drop adhesion are slippery lubricant-infused surfaces. The application of these surfaces is challenged by the depletion of lubricant. A simple but general concept is proposed to counteract lubricant depletion: capillary balancing. By balancing the capillary forces exerted by the solid scaffold with those from growing frost dendrites, the depletion of

lubricant can be minimized. This can be achieved by tuning the interstitial spacing of the solid scaffold. This design concept can be applied to SLIPS in general, thereby facilitating their successful implementation in anti-icing, drag reduction, and other fields.

Surface topography is an essential tool to introduce functionality, even if the wetting properties are insignificant. Silicone nanofilaments have exhibited greatly reduced bacterial adhesion; the sub-micrometer roughness offers only a vanishingly small number of anchoring points even in the wetted state. While this concept of passive anti-biofouling is highly promising, it requires an optimized surface topography and sufficient mechanical robustness. Since multi-resistant bacteria strains will become an increasing problem in modern society, more research in this area is urgently needed.

8 References

[1] L. Gao, T. J. McCarthy, *Langmuir* **2009**, *25*, 14105–14115.

[2] P. G. de Gennes, *Rev. Mod. Phys.* **1985**, *57*, 827–863.

[3] S. Herminghaus, *Europhys. Lett.* **2000**, *52*, 165–170.

[4] D. Quéré, *Annu. Rev. Mater. Res.* **2008**, *38*, 71–99.

[5] D. W. Pilat, P. Papadopoulos, D. Schäffel, D. Vollmer, R. Berger, H. J. Butt, *Langmuir* **2012**, *28*, 16812–16820.

[6] N. Gao, F. Geyer, D. W. Pilat, S. Wooh, D. Vollmer, H. J. Butt, R. Berger, *Nat. Phys.* **2018**, *14*, 191–196.

[7] A. Laroche, D. Bottone, S. Seeger, E. Bonaccurso, *Surf. Coat. Technol.* **2021**, *410*, 126971.

[8] K. Golovin, S. P. R. Kobaku, D. H. Lee, E. T. DiLoreto, J. M. Mabry, A. Tuteja, *Sci Adv.* **2016**, *2*, e1501496.

[9] S. B. Subramanyam, K. Rykaczewski, K. K. Varanasi, *Langmuir* **2013**, *29*, 13414–13418.

[10] H.-J. Butt, K. Graf, M. Kappl, *Physics and Chemistry of Interfaces*, Wiley-VCH, Weinheim, **2003**.

[11] T. Young, *Philos. Trans. Royal Soc.* **1805**, *95*, 65–87.

[12] A. Marmur, *Soft Matter* **2012**, *8*, 6867–6870.

[13] R. N. Wenzel, *Ind. Eng. Chem. Res.* **1936**, *28*, 988–994.

[14] T. Onda, S. Shibuichi, N. Satoh, K. Tsujii, *Langmuir* **1996**, *12*, 2125–2127.

[15] S. Shibuichi, T. Onda, N. Satoh, K. Tsujii, *J. Phys. Chem.* **1996**, *100*, 19512–19517.

[16] A. B. D. Cassie, S. Baxter, *Trans. Faraday Soc.* **1944**, *40*, 546–551.

[17] L. Gao, T. J. Mccarthy, *Langmuir* **2006**, *22*, 2966–2967.

[18] A. Tuteja, W. Choi, M. Ma, J. M. Mabry, S. A. Mazzella, G. C. Rutledge, G. H. Mckinley, R. E. Cohen, *Science* **2007**, *318*, 1618–1622.

[19] H. J. Butt, C. Semprebon, P. Papadopoulos, D. Vollmer, M. Brinkmann, M. Ciccotti, *Soft Matter* **2013**, *9*, 418–428.

[20] A. Grinthal, J. Aizenberg, *Chem. Mater.* **2014**, *26*, 698–708.

[21] A. Lafuma, D. Quéré, *Europhys. Lett.* **2011**, *96*, 56001.

[22] T. S. Wong, S. H. Kang, S. K. Y. Tang, E. J. Smythe, B. D. Hatton, A. Grinthal, J. Aizenberg, *Nature* **2011**, *477*, 443–447.

[23] P. Baumli, H. Teisala, H. Bauer, D. Garcia-Gonzalez, V. Damle, F. Geyer, M. D'Acunzi, A. Kaltbeitzel, H. J. Butt, D. Vollmer, *Adv. Sci.* **2019**, *6*, 1–8.

[24] C. W. Extrand, *Langmuir* **2003**, *19*, 3793–3796.

[25] L. Gao, T. J. McCarthy, *Langmuir* **2007**, *23*, 3762–3765.

[26] H. J. Butt, J. Liu, K. Koynov, B. Straub, C. Hinduja, I. Roismann, R. Berger, X. Li, D. Vollmer, W. Steffen, M. Kappl, *Curr. Opin. Colloid Interface Sci.* **2022**, *59*, 101574.

[27] A. Pockels, *Phys. Z.* **1914**, *15*, 39–46.

[28] H. J. Butt, N. Gao, P. Papadopoulos, W. Steffen, M. Kappl, R. Berger, *Langmuir* **2017**, *33*, 107–116.

[29] B. Becher-Nienhaus, G. Liu, R. J. Archer, A. Hozumi, *Langmuir* **2020**, *36*, 7835–7843.

[30] Z. Cai, A. Skabeev, S. Morozova, J. T. Pham, *Commun. Mater.* **2021**, *2*, DOI 10.1038/s43246-021-00125-2.

[31] H. Mishra, A. M. Schrader, D. W. Lee, A. Gallo, S. Y. Chen, Y. Kaufman, S. Das, J. N. Israelachvili, *ACS Appl. Mater. Interfaces* **2016**, *8*, 8168–8174.

[32] H. J. Butt, R. Berger, W. Steffen, D. Vollmer, S. A. L. Weber, *Langmuir* **2018**, *34*, 11292–11304.

[33] W. S. Y. Wong, L. Hauer, A. Naga, A. Kaltbeitzel, P. Baumli, R. Berger, M. D'Acunzi, D. Vollmer, H. J. Butt, *Langmuir* **2020**, *36*, 7236–7245.

[34] X. Li, S. Silge, A. Saal, G. Kircher, K. Koynov, R. Berger, H. J. Butt, *Langmuir* **2021**, *37*, 1571–1577.

[35] D. F. Cheng, C. Urata, M. Yagihashi, A. Hozumi, *Angew. Chem. Int. Ed.* **2012**, *51*, 2956–2959.

[36] X. Li, P. Bista, A. Z. Stetten, H. Bonart, M. T. Schür, S. Hardt, F. Bodziony, H. Marschall, A. Saal, X. Deng, R. Berger, S. A. L. Weber, H. J. Butt, *Nat. Phys.* **2022**, *18*, 713–719.

[37] F. Schellenberger, N. Encinas, D. Vollmer, H. J. Butt, *Phys. Rev. Lett.* **2016**, *116*, 096101.

[38] H.-J. Butt, I. v. Roisman, M. Brinkmann, P. Papadopoulos, D. Vollmer, C. Semprebon, *Curr. Opin. Colloid Interface Sci.* **2014**, *19*, 343–354.

[39] X. Zhang, F. Shi, J. Niu, Y. Jiang, Z. Wang, *J. Mater. Chem.* **2008**, *18*, 621–633.

[40] L. Gao, T. J. McCarthy, *Langmuir* **2006**, *22*, 6234–6237.

[41] E. Schäffer, P. Wong, *Phys. Rev. E* **2000**, *61*, 5257–5277.

[42] W. D. Harkins, F. E. Brown, *J. Am. Chem. Soc.* **1919**, *41*, 499–524.

[43] J.-H. Kim, H. P. Kavehpour, J. P. Rothstein, *Phys. Fluids* **2015**, *27*, 032107.

[44] J.-H. Wang, P. M. Claesson, S. J. L. Parker, H. Yasuda, *Langmuir* **1994**, *10*, 3887–3897.

[45] C. G. L. Furmidge, *J. Colloid Sci.* **1962**, *17*, 309–324.

[46] K. Kawasaki, *J. Colloid Sci.* **1960**, *15*, 402–407.

[47] C. W. Extrand, Y. Kumagai, *J. Colloid Interface Sci.* **1995**, *170*, 515–521.

[48] D. Daniel, J. V. I. Timonen, R. Li, S. J. Velling, M. J. Kreder, A. Tetreault, J. Aizenberg, *Phys. Rev. Lett.* **2018**, *120*, 244503.

[49] C. W. Extrand, A. N. Gent, *J. Colloid Interface Sci.* **1990**, *138*, 431–442.

[50] L. Wang, T. J. McCarthy, *Angew. Chem. Int. Ed.* **2016**, *55*, 244–248.

[51] W. Barthlott, C. Neinhuis, *Planta* **1997**, *202*, 1–8.

[52] T. Wagner, C. Neinhuis, W. Barthlott, *Acta Zool.* **1996**, *77*, 213–225.

[53] F. J. Norton, *Waterproofing Treatment of Materials*, **1942**, 2,386,259.

[54] H. J. Ensikat, P. Ditsche-Kuru, C. Neinhuis, W. Barthlott, *Beilstein J. Nanotechnol.* **2011**, *2*, 152–161.

[55] D. Öner, T. J. McCarthy, *Langmuir* **2000**, *16*, 7777–7782.

[56] M. D'Acunzi, L. Mammen, M. Singh, X. Deng, M. Roth, G. K. Auernhammer, H.-J. Butt, D. Vollmer, *Faraday Discuss.* **2010**, *146*, 35–48.

[57] W. S. Y. Wong, *Nano Lett.* **2019**, *19*, 1892–1901.

[58] M. Ma, R. M. Hill, J. L. Lowery, S. v. Fridrikh, G. C. Rutledge, *Langmuir* **2005**, *21*, 5549–5554.

[59] M. Callies, D. Quéré, *Soft Matter* **2005**, *1*, 55.

[60] H. Teisala, F. Geyer, J. Haapanen, P. Juuti, J. M. Mäkelä, D. Vollmer, H. J. Butt, *Adv. Mater.* **2018**, *30*, DOI 10.1002/adma.201706529.

[61] X. Deng, L. Mammen, H.-J. Butt, D. Vollmer, *Science* **2012**, *335*, 67–70.

[62] A. Tuteja, W. Choi, G. H. McKinley, R. E. Cohen, M. F. Rubner, *MRS Bull.* **2008**, *33*, 752–758.

[63] A. Tuteja, W. Choi, J. M. Mabry, G. H. McKinley, R. E. Cohen, *Proc. Natl. Acad. Sci. U.S.A.* **2008**, *105*, 18200–18205.

[64] M. Paven, P. Papadopoulos, L. Mammen, X. Deng, H. Sachdev, D. Vollmer, H. J. Butt, in *Pure and Applied Chemistry*, Walter De Gruyter GmbH, **2014**, pp. 87–96.

[65] M. Paven, R. Fuchs, T. Yakabe, D. Vollmer, M. Kappl, A. N. Itakura, H. J. Butt, *Adv. Funct. Mater.* **2016**, *26*, 4914–4922.

[66] N. Nasiri, T. D. Elmøe, Y. Liu, Q. H. Qin, A. Tricoli, *Nanoscale* **2015**, *7*, 9859–9867.

[67] H. K. Park, K. Y. Park, *KONA Powder Part. J.* **2015**, *32*, 85–101.

[68] L. Mädler, H. K. Kammler, R. Mueller, S. E. Pratsinis, *J. Aerosol Sci.* **2002**, *33*, 369–389.

[69] H. K. Kammler, L. Mädler, S. E. Pratsinis, *Chem. Eng. Technol.* **2001**, *24*, 583–596.

[70] R. Mueller, R. Jossen, H. K. Kammler, S. E. Pratsinis, M. K. Akhtar, *AIChE J.* **2004**, *50*, 3085–3094.

[71] F. Meierhofer, L. Mädler, U. Fritsching, *AIChE J.* **2020**, *66*, e16885.

[72] S. E. Pratsinis, *Prog. Energy Combust. Sci.* **1998**, *24*, 197–219.

[73] L. Mädler, A. A. Lall, S. K. Friedlander, *Nanotechnology* **2006**, *17*, 4783–4795.

[74] W. S. Y. Wong, G. Liu, N. Nasiri, C. Hao, Z. Wang, A. Tricoli, *ACS Nano* **2017**, *11*, 587–596.

[75] J. M. Mäkelä, M. Aromaa, H. Teisala, M. Tuominen, M. Stepien, J. J. Saarinen, M. Toivakka, J. Kuusipalo, *Aerosol Sci. Technol.***2011**, *45*, 827–837.

[76] H. Teisala, M. Tuominen, M. Aromaa, J. M. Mäkelä, M. Stepien, J. J. Saarinen, M. Toivakka, J. Kuusipalo, *Surf. Coat. Technol.* **2010**, *205*, 436–445.

[77] K. J. Brobbey, J. Haapanen, J. M. Mäkelä, M. Gunell, E. Eerola, E. Rosqvist, J. Peltonen, J. J. Saarinen, M. Toivakka, *SN Appl. Sci.* **2019**, *1*, 1–14.

[78] K. J. Brobbey, J. Haapanen, M. Tuominen, J. Mäkelä, M. Gunell, E. Eerola, J. J. Saarinen, M. Toivakka, *Text. Res. J.* **2020**, *90*, 503–511.

[79] R. Campos, A. J. Guenthner, A. J. Meuler, A. Tuteja, R. E. Cohen, G. H. McKinley, T. S. Haddad, J. M. Mabry, *Langmuir* **2012**, *28*, 9834–9841.

[80] European Commission, "Poly- and perfluoroalkyl substances (PFAS): Chemicals Strategy for Sustainability Towards a Toxic-Free Environment," **2020**.

[81] M. Scheringer, X. Trier, I. T. Cousins, P. de Voogt, T. Fletcher, Z. Wang, T. F. Webster, *Chemosphere* **2014**, *114*, 337–339.

[82] J. M. Conder, R. A. Hoke, W. de Wolf, M. H. Russell, R. C. Buck, *Environ. Sci. Technol.* **2008**, *42*, 995–1003.

[83] T. Liu, C. J. Kim, *Science* **2014**, *346*, 1096–1100.

[84] M. J. Kreder, D. Daniel, A. Tetreault, Z. Cao, B. Lemaire, J. V. I. Timonen, J. Aizenberg, *Phys. Rev. X* **2018**, *8*, 031053.

[85] J. D. Smith, R. Dhiman, S. Anand, E. Reza-Garduno, R. E. Cohen, G. H. McKinley, K. K. Varanasi, *Soft Matter* **2013**, *9*, 1772–1780.

[86] P. Baumli, M. D'Acunzi, K. I. Hegner, A. Naga, W. S. Y. Wong, H.-J. Butt, D. Vollmer, *Adv. Colloid Interface Sci.* **2021**, *287*, 102329.

[87] X. M. Li, D. Reinhoudt, M. Crego-Calama, *Chem. Soc. Rev.* **2007**, *36*, 1350–1368.

[88] D. C. Leslie, A. Waterhouse, J. B. Berthet, T. M. Valentin, A. L. Watters, A. Jain, P. Kim, B. D. Hatton, A. Nedder, K. Donovan, E. H. Super, C. Howell, C. P. Johnson, T. L. Vu, D. E. Bolgen,

S. Rifai, A. R. Hansen, M. Aizenberg, M. Super, J. Aizenberg, D. E. Ingber, *Nat. Biotechnol.* **2014**, *32*, 1134–1140.

[89] Andre Colas, *Dow Corning: Life Sciences* **2005**.

[90] L. Gao, T. J. McCarthy, *J. Am. Chem. Soc.* **2006**, *128*, 9052–9053.

[91] H. Teisala, P. Baumli, S. A. L. Weber, D. Vollmer, H. J. Butt, *Langmuir* **2020**, *36*, 4416–4431.

[92] X. Zhao, M. A. R. Khandoker, K. Golovin, *ACS Appl. Mater. Interfaces* **2020**, *12*, 15748–15756.

[93] J. W. Krumpfer, T. J. Mccarthy, *Faraday Discuss.* **2010**, *146*, 103–111.

[94] W. Chen, A. Y. Fadeev, M. C. Hsieh, D. Öner, J. Youngblood, T. J. McCarthy, *Langmuir* **1999**, *15*, 3395–3399.

[95] J. Liu, Y. Sun, X. Zhou, X. Li, M. Kappl, W. Steffen, H. J. Butt, *Adv. Mater.* **2021**, *33*, 2100237.

[96] X. Zhao, B. Khatir, K. Mirshahidi, K. Yu, J. N. Kizhakkedathu, K. Golovin, *ACS Nano* **2021**, *15*, 13559–13567.

[97] S. Wooh, N. Encinas, D. Vollmer, H. J. Butt, *Adv. Mater.* **2017**, *29*, 1–7.

[98] S. Wu, Y. Du, Y. Alsaid, D. Wu, M. Hua, Y. Yan, B. Yao, Y. Ma, X. Zhu, X. He, *Proc. Natl. Acad. Sci. U.S.A.* **2020**, *117*, 11240–11246.

[99] G. Graffius, F. Bernardoni, A. Y. Fadeev, *Langmuir* **2014**, *30*, 14797–14807.

[100] F. Weinhold, R. West, *Organometallics* **2011**, *30*, 5815–5824.

[101] J. W. Krumpfer, T. J. McCarthy, *Faraday Discuss.* **2010**, *146*, 103–111.

[102] S. Wooh, D. Vollmer, *Angew. Chem. Int. Ed.* **2016**, *55*, 6822–6824.

[103] H. Monder, L. Bielenki, H. Dodiuk, A. Dotan, S. Kenig, *Polymers* **2020**, *12*, 1–15.

[104] X. Zhao, L. Bi, B. Khatir, P. Serles, T. Filleter, J. E. Wulff, K. Golovin, *Chem. Eng.* **2022**, *442*, 136017.

[105] F. Geyer, M. D'Acunzi, A. Sharifi-Aghili, A. Saal, N. Gao, A. Kaltbeitzel, T.-F. Sloot, R. Berger, H.-J. Butt, D. Vollmer, *Sci. Adv.* **2020**, *6*, eaaw9727.

[106] W. S. Y. Wong, T. P. Corrales, A. Naga, P. Baumli, A. Kaltbeitzel, M. Kappl, P. Papadopoulos, D. Vollmer, H. J. Butt, *ACS Nano* **2020**, *14*, 3836–3846.

[107] M. K. Fu, I. Arenas, S. Leonardi, M. Hultmark, *J. Fluid. Mech.* **2017**, *824*, 688–700.

[108] B. Bhushan, Y. C. Jung, *Prog. Mater. Sci.* **2011**, *56*, 1–108.

[109] M. Paven, P. Papadopoulos, S. Schöttler, X. Deng, V. Mailänder, D. Vollmer, H. J. Butt, *Nat Commun* **2013**, *4*, 2512.

[110] K. Liu, L. Jiang, *Annu. Rev. Mater. Res.* **2012**, *42*, 231–263.

[111] A. J. W. Costerton, P. S. Stewart, E. P. Greenberg, *Science* **1999**, *284*, 1318–1322.

[112] R. M. Vejborg, P. Klemm, *Appl. Environ. Microbiol.* **2008**, *74*, 3551–3558.

[113] J. A. Callow, M. E. Callow, *Nat. Commun.* **2011**, *2*, 210–244.

[114] J. Liu, L. Ye, Y. Sun, M. Hu, F. Chen, S. Wegner, V. Mailänder, W. Steffen, M. Kappl, H. J. Butt, *Adv. Mater.* **2020**, *32*, 1908008.

[115] M. Meier, V. Dubois, S. Seeger, *Appl. Surf. Sci.* **2018**, *459*, 505–511.

[116] X. Zhang, L. Wang, E. Levänen, *RSC Adv.* **2013**, *3*, 12003–12020.

[117] G. B. Hwang, K. Page, A. Patir, S. P. Nair, E. Allan, I. P. Parkin, *ACS Nano* **2018**, *12*, 6050–6058.

[118] A. K. Epstein, T.-S. Wong, R. A. Belisle, E. M. Boggs, J. Aizenberg, *Proc. Natl. Acad. Sci. U.S.A.* **2012**, *109*, 13182–13187.

[119] N. Maccallum, C. Howell, P. Kim, D. Sun, R. Friedlander, J. Ranisau, O. Ahanotu, J. J. Lin, A. Vena, B. Hatton, T. S. Wong, J. Aizenberg, *ACS Biomater. Sci. Eng.* **2015**, *1*, 43–51.

[120] Y. Cheng, G. Feng, C. I. Moraru, *Front. Microbiol.* **2019**, *10*, 1–17.

[121] D. P. Linklater, V. A. Baulin, S. Juodkazis, R. J. Crawford, P. Stoodley, E. P. Ivanova, *Nat. Rev. Microbiol.* **2021**, *19*, 8–22.

[122] A. Elbourne, R. J. Crawford, E. P. Ivanova, *J. Colloid Interface Sci.* **2017**, *508*, 603–616.

[123] E. P. Ivanova, J. Hasan, H. K. Webb, G. Gervinskas, S. Juodkazis, V. K. Truong, A. H. F. Wu, R. N. Lamb, V. A. Baulin, G. S. Watson, J. A. Watson, D. E. Mainwaring, R. J. Crawford, *Nat. Commun.* **2013**, *4*, 1–7.

[124] N. Encinas, C. Y. Yang, F. Geyer, A. Kaltbeitzel, P. Baumli, J. Reinholz, V. Mailänder, H. J. Butt, D. Vollmer, *ACS Appl. Mater. Interfaces* **2020**, *12*, 21192–21200.

[125] F. Geyer, M. D'Acunzi, C. Y. Yang, M. Müller, P. Baumli, A. Kaltbeitzel, V. Mailänder, N. Encinas, D. Vollmer, H. J. Butt, *Adv. Mater.* **2019**, *31*, 1801324.

[126] S. Nath, S. F. Ahmadi, J. B. Boreyko, *Nanoscale Microscale Thermophys. Eng.* **2017**, *21*, 81–101.

[127] J. Petit, E. Bonaccurso, *Langmuir* **2014**, *30*, 1160–1168.

[128] A. J. Meuler, J. D. Smith, K. K. Varanasi, J. M. Mabry, G. H. McKinley, R. E. Cohen, *ACS Appl. Mater. Interfaces* **2010**, *2*, 3100–3110.

[129] M. Schwarzer, T. Otto, M. Schremb, C. Marschelke, H. T. Tee, F. R. Wurm, I. v. Roisman, C. Tropea, A. Synytska, *Chem. Mater.* **2019**, *31*, 112–123.

[130] L. Hauer, W. S. Y. Wong, V. Donadei, K. I. Hegner, L. Kondic, D. Vollmer, *ACS Nano* **2021**, *15*, 4658–4668.

[131] K. Rykaczewski, S. Anand, S. B. Subramanyam, K. K. Varanasi, *Langmuir* **2013**, *29*, 5230–5238.

[132] A. Angulo, P. van der Linde, H. Gardeniers, M. Modestino, D. Fernández Rivas, *Joule* **2020**, *4*, 555–579.

[133] J.-H. Kim, J. P. Rothstein, *Exp. Fluids* **2016**, *57*, 81.

[134] Z. Long, Y. Zhao, C. Zhang, Y. Zhang, C. Yu, Y. Wu, J. Ma, M. Cao, L. Jiang, *Adv. Mater.* **2020**, *32*, 1–8.

[135] Y. Luo, L. Tang, U. Khan, Q. Yu, H. M. Cheng, X. Zou, B. Liu, *Nat. Commun.* **2019**, *10*, 1–9.

[136] S. I. Karakashev, M. V. Grozdanova, *Adv. Colloid Interface Sci.* **2012**, *176–177*, 1–17.

[137] H. Leuner, C. Gerstenberg, K. Lechner, C. McHardy, C. Rauh, J. U. Repke, *Chem. Eng. Res. Des.* **2020**, *163*, 281–294.

[138] Y. Xing, X. Gui, L. Pan, B. El Pinchasik, Y. Cao, J. Liu, M. Kappl, H. J. Butt, *Adv. Colloid Interface Sci.* **2017**, *246*, 105–132.

[139] J. Rubio, M. L. Souza, R. W. Smith, *Miner. Eng.* **2002**, *15*, 139–155.

[140] C. Y. Teh, P. M. Budiman, K. P. Y. Shak, T. Y. Wu, *Ind. Eng. Chem. Res.* **2016**, *55*, 4363–4389.

[141] Z. Wu, X. Wang, H. Liu, H. Zhang, J. D. Miller, *Adv. Colloid Interface Sci.* **2016**, *235*, 190–200.

[142] A. P. Chandra, A. R. Gerson, *Adv. Colloid Interface Sci.* **2009**, *145*, 97–110.

[143] L. Rapoport, T. Emmerich, K. K. Varanasi, *Adv. Mater. Interfaces* **2020**, *7*, 1–8.

[144] J. Wang, Q. Yang, M. Wang, C. Wang, L. Jiang, *Soft Matter* **2012**, *8*, 2261–2266.

[145] A. Kannan, P. Hristov, J. Li, J. Zawala, P. Gao, G. G. Fuller, *J. Colloid Interface Sci.* **2020**, *575*, 298–305.

[146] H. De Maleprade, C. Clanet, D. Quéré, *Phys. Rev. Lett.* **2016**, *117*, 1–5.

[147] C. Shi, X. Cui, X. Zhang, P. Tchoukov, Q. Liu, N. Encinas, M. Paven, F. Geyer, D. Vollmer, Z. Xu, H. J. Butt, H. Zeng, *Langmuir* **2015**, *31*, 7317–7327.

[148] J. Huo, Q. Yang, J. Yong, P. Fan, Y. feng Lu, X. Hou, F. Chen, *Adv. Mater. Interfaces* **2020**, *7*, 1–8.

[149] J. Wang, Y. Zheng, F. Q. Nie, J. Zhai, L. Jiang, *Langmuir* **2009**, *25*, 14129–14134.

[150] D. Y. C. Chan, E. Klaseboer, R. Manica, *Soft Matter* **2011**, *7*, 2235–2264.

[151] Z. Chu, S. Seeger, *Chem. Soc. Rev.* **2014**, *43*, 2784–2798.

[152] J. Zhang, S. Seeger, *Angew. Chem. Int. Ed.* **2011**, *50*, 6652–6656.

[153] G. R. J. Artus, S. Jung, J. Zimmermann, H. P. Gautschi, K. Marquardt, S. Seeger, *Adv. Mater.* **2006**, *18*, 2758–2762.

[154] G. C. Frye, J. C. Berg, *J. Colloid Interface Sci.* **1989**, *127*, 222–238.

[155] A. Dippenaar, *Int. J. Miner. Process* **1982**, *9*, 1–14.

[156] D. Schäffel, K. Koynov, D. Vollmer, H. J. Butt, C. Schönecker, *Phys. Rev. Lett.* **2016**, *116*, 1–5.

[157] B. Liu, R. Manica, Q. Liu, E. Klaseboer, Z. Xu, G. Xie, *Phys. Rev. Lett.* **2019**, *122*, 1–5.

[158] D. Georgieva, A. Cagna, D. Langevin, *Soft Matter* **2009**, *5*, 2063–2071.

[159] F. Henrich, D. Fell, D. Truszkowska, M. Weirich, M. Anyfantakis, T. H. Nguyen, M. Wagner, G. K. Auernhammer, H. J. Butt, *Soft Matter* **2016**, *12*, 7782–7791.

[160] A. Bahrami, Y. Ghorbani, M. R. Hosseini, F. Kazemi, M. Abdollahi, A. Danesh, *Min. Eng.* **2019**, *71*, 43–45.

[161] F. Geyer, Y. Asaumi, D. Vollmer, H. J. Butt, Y. Nakamura, S. Fujii, *Adv. Funct. Mater* **2019**, *29*, 1–8.

[162] W. Y. Teoh, R. Amal, L. Mädler, *Nanoscale* **2010**, *2*, 1324–1347.

[163] L. Mädler, A. Roessler, S. E. Pratsinis, T. Sahm, A. Gurlo, N. Barsan, U. Weimar, *Sens. Actuators B Chem.* **2006**, *114*, 283–295.

[164] A. Pratsinis, G. A. Kelesidis, S. Zuercher, F. Krumeich, S. Bolisetty, R. Mezzenga, J. C. Leroux, G. A. Sotiriou, *ACS Nano* **2017**, *11*, 12210–12218.

[165] A. Tricoli, R. Bo, *Front. Nanosci.* **2020**, *15*, 247–269.

[166] M. Gockeln, S. Pokhrel, F. Meierhofer, J. Glenneberg, M. Schowalter, A. Rosenauer, U. Fritsching, M. Busse, L. Mädler, R. Kun, *J. Power Sources* **2018**, *374*, 97–106.

[167] P. Kulkarni, P. Biswas, *Aerosol Sci. Technol.* **2004**, *38*, 541–554.

[168] O. Reynolds, *Philos. Trans. R. Soc.* **1886**, *177*, 157.

[169] G. K. Batchelor, *An Introduction to Fluid Dynamics*, Cambridge University Press, **1967**.

[170] L. G. Leal, *Advanced Transport Phenomena: Fluid Mechanics and Convective Transport*, Cambridge University Press, **2007**.

[171] E. Chatzigiannakis, J. Vermant, *Phys. Rev. Lett.* **2020**, *125*, 158001.

[172] A. Vrij, J. T. H. G. Overbeek, *J. Am Chem Soc.* **1968**, *90*, 3074–3078.

[173] X. Gao, L. Jiang, *Nature* **2004**, *432*, 36.

[174] R. Fürstner, W. Barthlott, C. Neinhuis, P. Walzel, *Langmuir* **2005**, *21*, 956–961.

[175] N. Miljkovic, E. N. Wang, *MRS Bull.* **2013**, *38*, 397.

[176] M. J. Kreder, J. Alvarenga, P. Kim, J. Aizenberg, *Nat. Rev. Mater.* **2016**, *1*, 15003.

[177] S. Pan, R. Guo, M. Björnmalm, J. J. Richardson, L. Li, C. Peng, N. Bertleff-Zieschang, W. Xu, J. Jiang, F. Caruso, *Nat. Mater.* **2018**, *17*, 1040–1047.

[178] A. T. Paxson, K. K. Varanasi, *Nat. Commun.* **2013**, *4*, 1–8.

[179] C. Peng, Z. Chen, M. K. Tiwari, *Nat. Mater.* **2018**, *17*, 355–360.

[180] Q. Wang, G. Sun, Q. Tong, W. Yang, W. Hao, *Chem. Eng. J.* **2021**, *426*, 130829.

[181] M. Long, S. Peng, X. Yang, W. Deng, N. Wen, K. Miao, G. Chen, X. Miao, W. Deng, *ACS Appl. Mater. Interfaces* **2017**, *9*, 15857–15867.

[182] K. I. Hegner, W. S. Y. Wong, D. Vollmer, *Adv. Mater.* **2021**, *33*, 2101855.

[183] S. Shabanian, B. Khatir, A. Nisar, K. Golovin, *Nat. Sustain.* **2020**, *3*, 1059–1066.

[184] A. B. D. Cassie, *Discuss. Faraday Soc.* **1948**, *3*, 11–16.

[185] M. J. Hokkanen, M. Backholm, M. Vuckovac, Q. Zhou, R. H. A. Ras, *Adv. Mater.* **2021**, *33*, 1–7.

[186] G. Vazquez, E. Alvarez, J. M. Navaza, *J. Chem. Eng. Data* **1995**, *40*, 611–614.

[187] A. I. ElSherbini, A. M. Jacobi, *J. Colloid Interface Sci.* **2006**, *299*, 841–849.

[188] E. Pierce, F. J. Carmona, A. Amirfazli, *Colloids Surf. A: Physicochem. Eng. Asp.* **2008**, *323*, 73–82.

[189] W. S. Y. Wong, K. I. Hegner, V. Donadei, L. Hauer, A. Naga, D. Vollmer, *Nano Lett.* **2020**, *20*, 8508–8515.

[190] M. Mohseni, H. S. Far, M. Hasanzadeh, K. Golovin, *Prog. Org. Coat.* **2021**, *157*, 106319.

[191] I. Luzinov, S. Minko, V. v Tsukruk, *Prog. Polym. Sci.* **2004**, *29*, 635–698.

[192] C. Urata, B. Masheder, D. F. Cheng, D. F. Miranda, G. J. Dunderdale, T. Miyamae, A. Hozumi, *Langmuir* **2014**, *30*, 4049–4055.

[193] J. N. Lee, C. Park, G. M. Whitesides, *Anal. Chem.* **2003**, *75*, 6544–6554.

[194] P. J. Carvalho, M. G. Freire, I. M. Marrucho, J. Queimada, *J. Chem. Eng. Data* **2008**, 1346–1350.

[195] C. M. Hansen, *Hansen Solubility Parameter - A User's Handbook*, CRC Press, Boca Raton, Florida, **2007**.

[196] T. Uragami, I. Sumida, T. Miyata, T. Shiraiwa, H. Tamura, T. Yajima, *Mater. Sci. Appl.* **2011**, *02*, 169–179.

[197] W. Zeng, Y. Du, Y. Xue, H. L. Frisch, in *Physical Properties of Polymers Handbook*, **2007**, pp. 289–303.

[198] K. S. Lee, N. Ivanova, V. M. Starov, N. Hilal, V. Dutschk, *Adv. Colloid Interface Sci.* **2008**, *144*, 54–65.

[199] J. E. Oliver, *Encyclopedia of World Climatology*, Springer Netherlands, Dordrecht, **2008**.

[200] B. Na, R. L. Webb, *Int. J. Heat Mass Transf.* **2003**, *46*, 3797–3808.

[201] S. Sastry, *Nature* **2005**, *438*, 746–747.

[202] J. Guadarrama-Cetina, A. Mongruel, W. González-Viñas, D. Beysens, *Europhys. Lett.* **2013**, *101*, 16009.

[203] H. Niemelä-Anttonen, H. Koivuluoto, M. Tuominen, H. Teisala, P. Juuti, J. Haapanen, J. Harra, C. Stenroos, J. Lahti, J. Kuusipalo, J. M. Mäkelä, P. Vuoristo, *Adv. Mater. Interfaces* **2018**, *5*, 1800828.

[204] P. Kim, T. S. Wong, J. Alvarenga, M. J. Kreder, W. E. Adorno-Martinez, J. Aizenberg, *ACS Nano* **2012**, *6*, 6569–6577.

[205] J. Lv, Y. Song, L. Jiang, J. Wang, *ACS Nano* **2014**, *8*, 3152–3169.

[206] P. Irajizad, S. Nazifi, H. Ghasemi, *Adv. Colloid Interface Sci.* **2019**, *269*, 203–218.

[207] S. Peppou-Chapman, C. Neto, *ACS Appl. Mater. Interfaces* **2018**, *10*, 33669–33677.

[208] P. Kim, M. J. Kreder, J. Alvarenga, J. Aizenberg, *Nano Lett.* **2013**, *13*, 1793–1799.

[209] J. L. Laforte, M. A. Allaire, J. Laflamme, *Atmos. Res.* **1998**, *46*, 143–158.

[210] T. Kameda, H. Yoshimi, N. Azuma, H. Motoyama, *J. Glaciol.* **1999**, *45*, 394–396.

[211] A. Perșoiu, S. Lauritzen, in *Ice Caves*, Elsevier, **2018**, pp. 21–32.

[212] C. A. Knight, A. L. Devries, *J. Glaciol.* **1985**, *31*, 127–135.

[213] R. le Gall, J. M. Grillot, C. Jallut, *Int. J. Heat Mass Transf.* **1997**, *40*, 3177–3187.

[214] H.-J. Butt, M. Kappl, *Surface and Interfacial Forces 2e*, Wiley-VCH Verlag GmbH & Co. KGaA, Weinheim, Germany, **2018**.

[215] T. Koop, B. Luo, A. Tsias, T. Peter, *Nature* **2000**, *406*, 611–614.

[216] T. Kajiya, F. Schellenberger, P. Papadopoulos, D. Vollmer, H.-J. Butt, *Sci. Rep.* **2016**, *6*, 23687.

[217] S. Jung, M. K. Tiwari, D. Poulikakos, *Proc. Natl. Acad. Sci. U.S.A.* **2012**, *109*, 16073–16078.

[218] W. E. Lorensen, H. E. Cline, in *Proceedings of the 14th Annual Conference on Computer Graphics and Interactive Techniques - SIGGRAPH '87*, ACM Press, New York, New York, USA, **1987**, pp. 163–169.

[219] W. A. Murray, R. List, *J. Glaciol.* **1972**, *11*, 415–429.

[220] A. M. Rankin, E. W. Wolff, S. Martin, *J. Geophys. Res. Atmos.* **2002**, *107*, 4683.

[221] R. M. Klevens, J. R. Edwards, C. L. Richards, T. C. Horan, R. P. Gaynes, D. A. Pollock, D. M. Cardo, *Public Health Rep.* **2007**, *122*, 160–166.

[222] M. E. Davey, G. A. O'toole, *Microbiol. Mol. Biol. Rev.* **2000**, *64*, 847–867.

[223] W. J. Yang, K. G. Neoh, E. T. Kang, S. L. M. Teo, D. Rittschof, *Prog. Polym. Sci.* **2014**, *39*, 1017–1042.

[224] J. T. Trevors, *Enzyme Microb. Technol.* **1987**, *9*, 331–333.

[225] W. Yandi, S. Mieszkin, P. Martin-Tanchereau, M. E. Callow, J. A. Callow, L. Tyson, B. Liedberg, T. Ederth, *ACS Appl. Mater. Interfaces* **2014**, *6*, 11448–11458.

[226] K. W. Kolewe, J. Zhu, N. R. Mako, S. S. Nonnenmann, J. D. Schiffman, *ACS Appl. Mater. Interfaces* **2018**, *10*, 2275–2281.

[227] R. J. Crawford, H. K. Webb, V. K. Truong, J. Hasan, E. P. Ivanova, *Adv. Colloid Interface Sci.* **2012**, *179–182*, 142–149.

[228] C. S. Ware, T. Smith-Palmer, S. Peppou-Chapman, L. R. J. Scarratt, E. M. Humphries, D. Balzer, C. Neto, *ACS Appl. Mater. Interfaces* **2018**, *10*, 4173–4182.

[229] D. P. Linklater, S. Juodkazis, E. P. Ivanova, *Nanoscale* **2017**, *9*, 16564–16585.

[230] S. D. Puckett, E. Taylor, T. Raimondo, T. J. Webster, *Biomaterials* **2010**, *31*, 706–713.

[231] D. E. Mainwaring, S. H. Nguyen, H. Webb, T. Jakubov, M. Tobin, R. N. Lamb, A. H. F. Wu, R. Marchant, R. J. Crawford, E. P. Ivanova, *Nanoscale* **2016**, *8*, 6527–6534.

[232] P. Papadopoulos, L. Mammen, X. Deng, D. Vollmer, H.-J. Butt, *Proc. Natl. Acad. Sci. U.S.A.* **2013**, *110*, 3254–3258.

[233] G. R. Meseck, R. Kontic, G. R. Patzke, S. Seeger, *Adv. Funct. Mater.* **2012**, *22*, 4433–4438.

[234] T. Zhang, J. Gu, X. Liu, D. Wei, H. Zhou, H. Xiao, Z. Zhang, H. Yu, S. Chen, *Mater. Sci. Eng. C* **2020**, *111*, 110855.

9 Acknowledgments

[redacted]

10 Publications and Contributions

10.1 List of Publications

- Herber, U., **Hegner, K. I.**, Wolters, D., Siris, R., Wrobel, K., Hoffmann, A., Lochenie, C., Weber, B., Kuckling, D., Herres-Pawlis, S. Iron(II) and Zinc(II) Complexes with Tetradentate Bis(pyrazolyl)methane Ligands as Catalysts for the Ring-Opening Polymerisation of rac-Lactide. *European Journal of Inorganic Chemistry* **2017**, 1341-1354 (2017).
- Wong, W. S. Y., **Hegner K. I.**, Donadei, V., Hauer, L., Naga, A., Vollmer, D. Capillary Balancing: Designing Frost-Resistant Lubricant-Infused Surfaces. *Nano Letters* **20**, 8508-8515 (2020).
- Baumli, P., D'Acunzi, M., **Hegner, K. I.**, Naga, A., Wong, W. S. Y., Butt, H.-J., Vollmer, D. The challenge of lubricant-replenishment on lubricant-impregnated surfaces. *Advances in Colloid and Interface Science* **287**, 102329 (2020).
- Hauer, L., Wong, W. S. Y., Donadei, V., **Hegner, K. I.**, Kondic, L., Vollmer, D. How Frost Forms and Grows on Lubricated Micro- and Nano Structured Surfaces. *ACS Nano* **15**, 4658-4668 (2021).
- D'Acunzi, M., Sharifi-Aghili, A., **Hegner, K. I.**, Vollmer, D. Super liquid repellent coatings against the everyday life wear: heating, freezing, scratching. *IScience* **24**, 102460 (2021).
- **Hegner, K. I.**, Wong, W. S. Y., Vollmer, D. Ultrafast Bubble Bursting by Superamphiphobic Coatings. *Advanced Materials* **33**, 2101855 (2021).
- Wong, W. S. Y., Naga, A., Hauer, L., Baumli, P., Bauer, H., D'Acunzi, M., Kaltbeitzel, A., **Hegner, K. I.**, Butt, H.-J., Vollmer, D. Super liquid repellent surfaces for anti-foaming and froth management. *Nature Communications* **12**, 5358 (2021).
- Baumli, P., Hauer, L., Lorusso, E., Sharifi-Aghili, A., **Hegner, K. I.**, D´Acunzi, M., Gutmann, J., Dünweg, B., Vollmer, D. Linear shrinkage of hydrogel coatings exposed to flow: Interplay between dissolution of water and advective transport. *Soft Matter* **18**, 365–371 (2022).
- **Hegner, K. I.**, [redacted] Fluorine-Free Super-Liquid-Repellent Surfaces: Pushing the Limits of PDMS, submitted (2022).
- **Hegner, K. I.**, [redacted] Effect of Solid-Liquid Interactions on the Wettability of Super-Liquid-Repellent PDMS Surfaces, in preparation (2022).

10.2 List of Contributions

- Wetting Dynamics, September 28th to 30th 2020, Bonn, Germany, Poster presentation: “Air Bubble Bursting on Superamphiphobic Hierarchical Structures”
- Droplets, August 14th to 18th 2021, Darmstadt, Germany, Poster presentation: “Ultrafast Bubble Bursting and Passive Anti-Foaming by Superamphiphobic Surfaces”
- 33rd Australian Colloid and Surface Science Student Conference, January 31st to February 2nd 2022, Australia, Oral presentation: “Ultrafast Bubble Bursting by Superamphiphobic Surfaces”
- 3rd International Conference on Materials Science & Engineering, April 18th to 22nd 2022, Boston, USA, Oral presentation: “Ultrafast Bubble Bursting by Superamphiphobic Surfaces”
- 36th European Colloid and Interface Society Conference, September 4th to 9th 2022, Crete, Greece, Oral presentation: “Superamphiphobic Surfaces for Ultrafast Single Bubble Bursting and Bulk Defoaming”